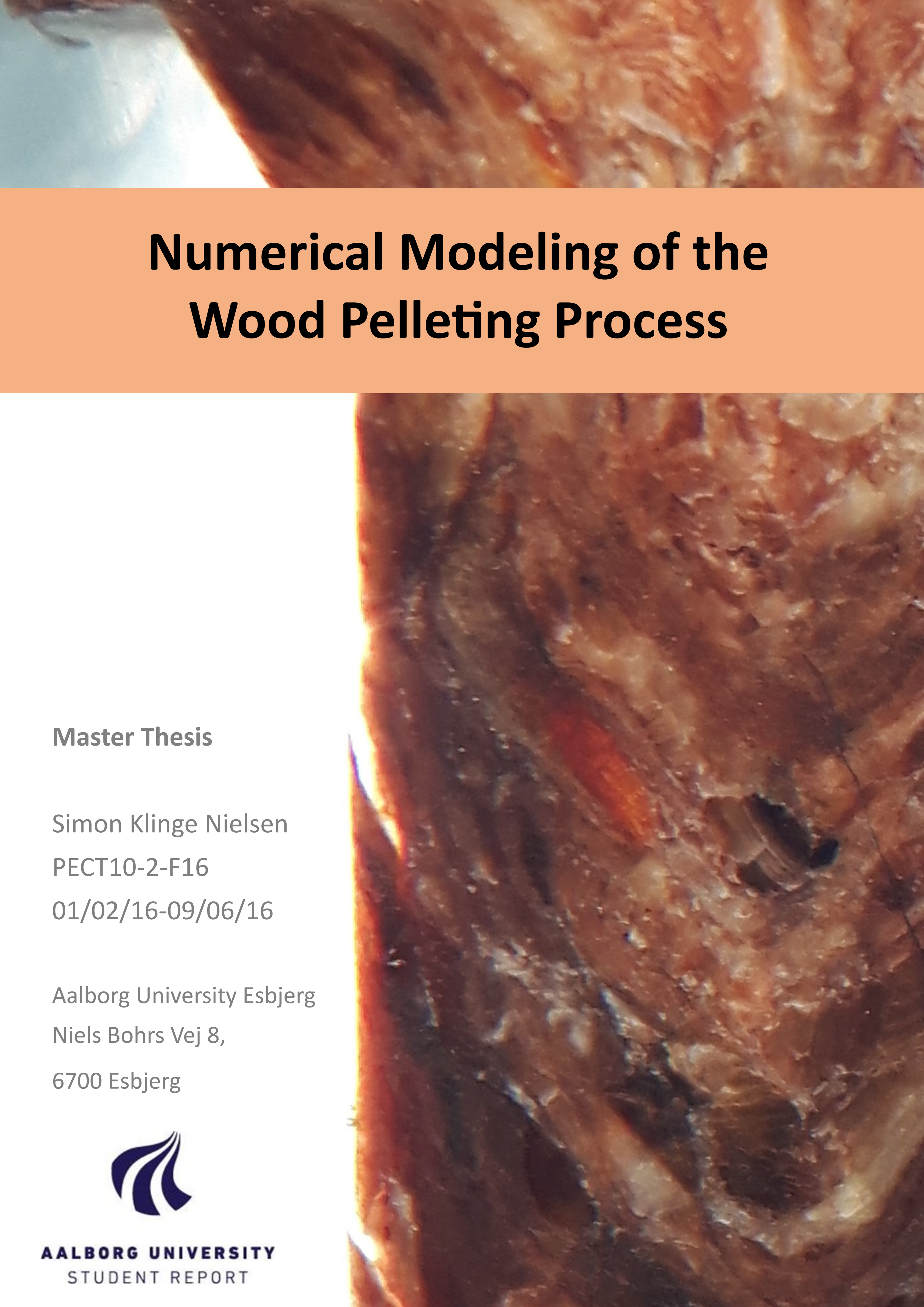

Numerical Modeling of the Wood Pelleting Process

Master Thesis

Simon Klinge Nielsen
PECT10-2-F16
01/02/16-09/06/16

Aalborg University Esbjerg
Niels Bohrs Vej 8,
6700 Esbjerg

AALBORG UNIVERSITY
STUDENT REPORT

Title Sheet

Theme:	Master Thesis
Project title:	Numerical Modeling of the Wood Pelleting Process
Group:	PECT10-2-F16
Semester:	10th semester
Supervisor:	Matthias Mandø
University:	Aalborg University Esbjerg
Initial problem:	*How does the inlet design of a pellet channel affect the pelleting process?*

Signature:

Simon Klinge Nielsen

Abstract

The topic of this project is pelleting of wood, where the main focus is how the die design affects the pelleting process. The project provides a thorough review of the pelleting process, and presents results of published studies. The project is carried out with experimental work and includes two numerical models. The experiments provides an insight of how the pelleting material behaves when pressed into a die. The project is the first step in order to be able to simulate the pelleting process. A 1D and a 2D model have been set up, in order to simulate the pelleting load for dies with different inlet designs. With the 1D model it is possible to simulate pelleting loads for dies without an inlet. With the 2D model it is possible to perform simulations, that shows the correct tendencies of the pelleting load, when an inlet is added to the die.

Preface

This project is written by Simon Klinge Nielsen in the project period 1/2-2016 to 9/6-2016. The project is prepared in cooperation with Andritz Feed & Biofuel located in Esbjerg. The project is a natural extend of a project written in the 9th semester. The main focus for this report is dedicated for process engineering purposes regarding pelleting processes. One of the main goals for this project, is to set up numerical models which can simulate, how the pelleting process is affected by the inlet design of the pelleting dies.

A thank is dedicated to Andritz Feed & Biofuel for the opportunity of this project, and a special thank to the department of Research and Development, for providing useful knowledge during the project period.

Contents

Nomenclature

Symbol	**Description**	**Unit**
x, y	Coordinate	$-$
N	Number of axial elements	$-$
M	Number of radial elements	$-$
A	Area	m^2
l	Length	m
d	Diameter	m
r	Radius	m
z	Chamfer depth	mm
β	Active press area	$-$
α	Inlet angle	^{o}
T	Temperature	^oC
T_g	Transition temperature for lignin	^oC
P	Pressure	Pa
F	Force	N
σ	Normal stress	Pa
τ	Shear stress	Pa
ρ	Density	$\frac{kg}{m^3}$
V	Volume	m^3
m	Mass	kg
$\dot{m}$	Massflow	$\frac{kg}{s}$
V_s	Specific volume	$\frac{m^3}{kg}$
h	Height	m
k	Empirical constant	$-$
μ	Friction factor	$-$
ν	Poisson's ratio	$-$

ϕ	Fiber orientation	$-$
E	Modulus of elasticity	MPa
v	Velocity	$\frac{m}{s}$
$\dot{W}$	Power	W
w_s	Specific energy	$\frac{J}{kg}$

Introduction

We live in a world, where we constantly are reminded of the rising challenges with carbon-dioxide emissions to the atmosphere. There has been suggested many solutions, but common for all are, that we have to rethink how we today recover our energy and develop new technologies. A transition towards a purely green energy can take several years, and therefore we have to utilize the technologies that already are available. One of the immediate technologies, is to switch from the combustion of fossil fuels, and instead use biomass.

In the year 2013, the danish energy company Dong announced, that in year 2020, 50% of their energy will come from combustion of biomass [2]. The annual consumption of coal has to be reduced by 65% (3.1 $Mton$ to 1.1 $Mton$) in this period. The amount of biomass used as fuel shall be increased with 121% (1.4 $Mton$ to 3.1 $Mton$). According to the plan, 58% of the biomass will be wood pellets (1.8 $Mton$). This means, that the use of wood pellets increases with 100% in the before mentioned period, from 0.9 $Mton$ to 1.8 $Mton$. In the 2020, 43% of the total energy from Dong will come from combustion of wood pellets.

This danish example is a part of a general tendency seen in the global marked for wood pellets, where the annual production increases year after year [3].

The pelleting process is an energy consuming process, and with the increasing demand of wood pellets, it is time to evaluate the production methods, and search for ways to optimize the design of the pellet mills.

The primary way of producing wood pellets originate from production of livestock feed, where a mixture of compounds is pelleted in pellet mills with ring dies. The development of the pelleting process has until now mostly been focusing on the material that is pelleted, rather than evaluate the physical design of the pellet mill.

In present time two PhD-studies concerning the pelleting process has been conducted [4] [5], where each of them has been focusing on the pelleting material, and its dependency in the pelleting process. This project is set up in order to research how the die design affects the pelleting process, such that more efficient die designs, with respect to energy consumption, can be implemented in the future production of wood pellets. Therefor this project can be stated as being a pioneer work.

The project is divided into four chapters.
Chapter one is intended to provide the reader with information about the pelleting process. The pelleting process is a complex process, where multiple processes occur, and several parameters has an effect on these. Therefore is chapter one a thorough description of the entire pelleting process, combined with a state of the art analysis of the pelleting process, where existing knowledge is presented.

With an overview of the pelleting process and the existing knowledge, the topic is narrowed down to a problem definition, which lists the goals for this project. The goals of the project involves experiments and setting up numerical models, which can simulate the pelleting process in the pellet channel.

In chapter two, the laboratory work and the result of this is presented, while chapter three is a description of the numerical models. Chapter four is the conclusion of the project.

CHAPTER 1

Pelleting Process

1.1 Pelleting

The primary purpose of pelleting a material is to ease the handling and lower the cost for transportation. Volume is an often limiting factor when it comes transportation. By increasing the density of a material, the required volume for transporting a certain amount of material is lowered. Pelleting processes are divided into two main sections; livestock feed and biomass. Today's concept of pelleting was developed for livestock feed, but in the past decade, the market for biomass pelleting is rapidly rising. Pelleted biomass is primary used in power and heat production, where wood represents the main part of the annual pellet production [6]. Figure 1.1 shows the development of the wood pellet production during the last decade. In the last couple of years the production of pelleted straw and grasses also has increased.

This project is focused on the pelleting of biomass, especially wood, but the concept of the pelleting process is the same for all materials.

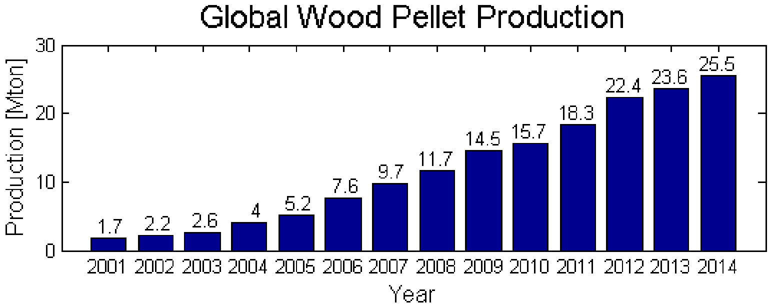

Figure 1.1: Annual production of wood pellets world wide [3].

1.2 The Pelleting Process

Wood pellets are often produced from waste material from other productions, though a few large production sites prepare wood only for pelleting. An example of a site that only produces wood pellets from its raw material is Vyborgskaja Cellulosa in the town of Vyborg located in Russia. At this site 36 Andritz Feed & Biofuel pellet mills are installed, with a total capacity of 125 $\frac{ton}{h}$ which equals an annual production of 0.9 $Mton$.

The raw material used for the pelleting process can be prepared in different manners, examples of these are shown in figure 1.2. In table 1.1 properties of the four wood manners are listed. Both for transportation and power and heat production, an energy-rich fuel is desirable. The values of specific energy content in table 1.1 shows, that wood pellets have a volumetric specific energy content, that is five times higher than for waste wood and wood chips. The high specific energy content of wood pellets lowers the transportation costs and the required storage capacity.

Figure 1.2: Wood processed in different manners. A: Sawmill wood waste. B: Wood chips. C: Sawdust/grinded wood chips. D: Wood pellets [6].

Property	**Wood chips and sawmill wood waste**	**Dry sawdust**	**Wood pellets**
Bulk density	300 $\left[\frac{kg}{m^3}\right]$	160 $\left[\frac{kg}{m^3}\right]$	650 $\left[\frac{kg}{m^3}\right]$
Moisture	55 %	12 %	8 %
Specific energy content	2.00 $\left[\frac{MWh}{ton}\right]$	4.40 $\left[\frac{MWh}{ton}\right]$	4.80 $\left[\frac{MWh}{ton}\right]$
	0.60 $\left[\frac{MWh}{m^3}\right]$	0.70 $\left[\frac{MWh}{m^3}\right]$	3.12 $\left[\frac{MWh}{m^3}\right]$

Table 1.1: Properties of wood processed in different manners [6].

1.2.1 Grinding of the Material

Before the waste material or the prepared wood chips enters the pellet mill, it is grinded in order to reduce the particle size. The grinding process is carried out in hammer mills, where beater rolls grinds the wood to a desired particle size. A screen with a hole pattern encloses the beater roll. The particle size can be controlled by changing the hole size in the screen. The usual hole size is in the range of 3-8 mm. The capacity of the hammer mill is highly dependent of the hole size in the screen, where larger holes increases the capacity. Another important parameter of the grinding process is the moisture content (denoted MC) of the material entering the hammer mill. The elasticity of the wood fibers is affected by the moisture content of the wood. Wood with a high moisture content is more elastic compared to dry wood, which is more brittle [7]. Therefore the wood is dried before entering the hammer mill, since a brittle material will ease the grinding process and further more increase the efficiency. The moisture content of wood entering the hammer mill is typical in the range 4-8 % on wet basis ($w.b.$) [6]. The energy required for the grinding process is $\approx 65\,\frac{kWh}{ton}$ [6].

1.2.2 Pelleting of the Material

The grinded material enters the pellet mill, where it is pressed into high density pellets. When the material is pelleted, a low moisture content is undesirable. Andritz's own experiences have shown that pelleting of dry material ($MC < 7\%(w.b)$) increases the energy demand of the pelleting process, and produces low quality pellets. This has also been confirmed in studies made by Nielsen et. al. [8] and Stelte et. al. [7].

To increase the MC of the material before entering the pellet mill, it is led through a conditioner. The conditioner is a long tube, where a conveyor provides a propulsion, while moisture is added to the material using steam. Adjusting the propulsion velocity and the amount of steam, it is possible to control the MC added to the material at the exit of the conditioner. The hot steam added in the conditioner, increases the temperature of the material, which is beneficial for the pelleting process. At the exit of the conditioner, the material has a MC of ≈ 15 % and a temperature of $\approx 70^oC$. At some production sites, the grinded material is conditioned with cold water instead of steam, which causes the material to enter the pellet mill with a lower temperature.

Andritz Feed & Biofuel produces a wide range of pellet mills for different purposes and capacities, but the concept of the process is identical for all of them. Generally the pellet mills developed for biomass pelleting has a lower capacity compared to the livestock feed pellet mills. Pelleting of biomass demands high stresses to be applied to the pelleting material, which causes a high wear on the pellet mill compared to pelleting of livestock feed. Wear parts of the biomass pellet mills are produced of high strength alloys to maintain the durability of the pellet mill. A picture of a Andritz PM30 pellet mill, developed for biomass pelleting, is shown in figure 1.3. A PM30 pellet mill is equipped with a 355 kW electrical powered motor, and has a capacity of pelleting $\approx\ 5\frac{ton}{h}$ dependent of the pelleting material. The total weight of the pellet mill is $11.8\,ton$. The biomass pellet mill with the highest capacity produced by Andritz Feed & Biofuel is the Biomax pellet mill, which has a capacity of pelleting $\approx\ 10\frac{ton}{h}$.

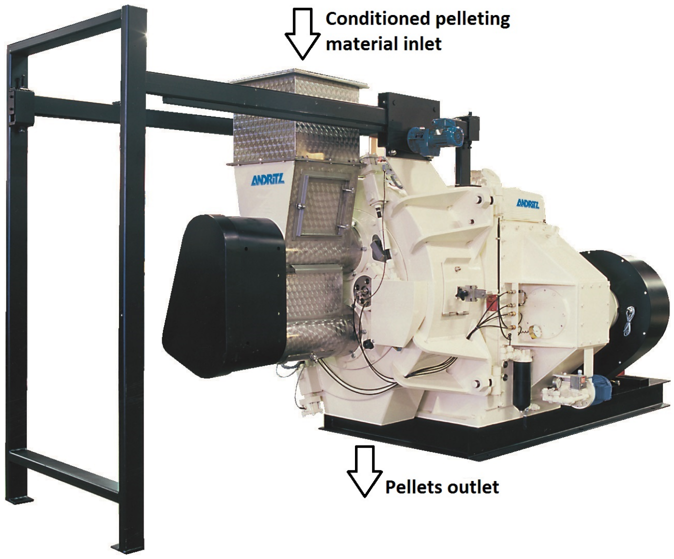

Figure 1.3: Andritz PM30 pellet mill, developed for biomass pelleting [6].

Figure 1.4: Ring die for PM30 [6].

When the conditioned pelleting material enters the pellet mill, the mass flow are split into two or three equal sized mass flows, which is separately led into the pelleting chamber. In the pelleting chamber a ring die is mounted, which is connected by a shaft to the electrical motor. A ring die for a PM30 is shown in figure 1.4.

The ring die is equipped with a number of pellet channels, wherein the pellets are formed. The size and design of the ring die varies dependent of the pellet mill and the material that has to be pelleted. The most common diameters of biomass pellets are 6 and 8 *mm*. A ring die for a PM30 pellet mill with 8 *mm* pelleting channels has the following specifications:

- Die diameter: $850\,mm$.
- Die width: $132\,mm$.
- Number of pellet channels: 2964.
- Total inner surface area: $352.5 \cdot 10^3\,mm^2$.
- Total area of pellet channel inlets: $148.9 \cdot 10^3\,mm^2$.

The distribution pattern of the pelleting channels in the ring die varies dependent of the pellet mill, and has to be fitted to the pelleting material. The pattern is specified by a parameter called the active press area. The active area is the fraction of the total hole area in the ring die, compared to the inner surface area. The active press area is specified in equation 1.1 where:

- β is the active press area of the ring die $[-]$
- n is the number of pelleting channels in the ring die $[-]$
- d_p is the diameter of the pelleting channels $[m]$
- d_{die} is the inner diameter of the ring die $[m]$
- w_{die} is the width of the ring die $[m]$

$$\beta = \frac{n \cdot A_{hole}}{A_{ring.die}} = \frac{n \cdot \frac{1}{4} \cdot d_p}{d_{die} \cdot \pi \cdot w_{die}} \tag{1.1}$$

Ring dies used for pelleting of biomass is produced with an active press area of $\beta \approx 40\%$, while ring dies for livestock feed has a higher active area. The reason for lowering the active press area for biomass dies (less or smaller holes) is to increase the strength of the ring die, due to the higher stress that is applied when pelleting biomass.

Inside the ring die are two or three rolls mounted, dependent of the type of pellet mill. The mass flow is split into the number of rolls in the pellet mill. Each mass flow of pelleting material is distributed on the inner surface of the ring die in front of each roll. When the die rotates, the pelleting material is pressed between the roll and the die, which forces the material into the pellet channels in the ring die. The clearance between the rolls and the ring die is $\approx 0.5\,mm$. A sketch of a sliced ring die and a roll is shown in figure 1.5, illustrating the position of the roll and the ring die. The red arrow symbolizes the direction of rotation for the ring die.

The uncompressed pelleting material, distributed on the inner surface of the ring die, is compressed and forced into a pellet channel when it passes a roll. The concept is illustrated in figure 1.6.

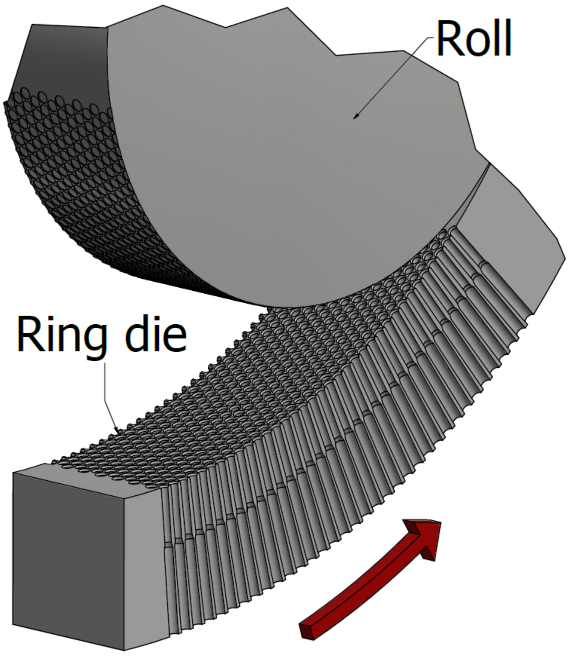

Figure 1.5: Sectional drawing of the ring die and the roll.

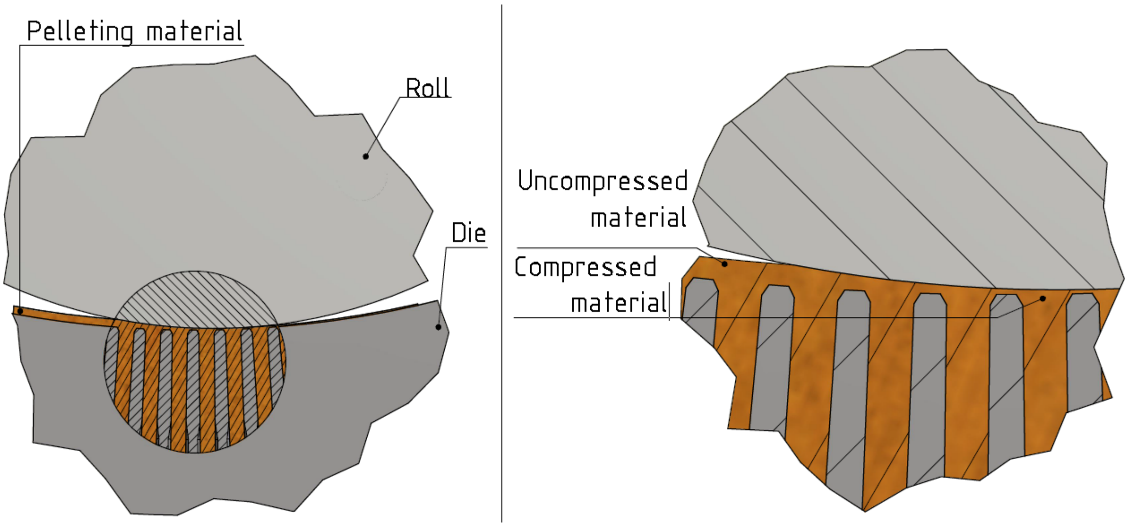

Figure 1.6: Cross sectional view of a roll compressing the pelleting material into the pellet channels.

The extrusion causes compressed material to leave the pellet channel shaped as a pellet. In a PM30 pellet mill with two rolls, the speed of the ring die is 128 RPM, which causes each pelleting channel in the ring die to pass a roll 4.27 times each second.

At the outer surface of the ring die a blade is mounted. The blade cuts the pellets into a desired length, which is three to four times the diameter of the pellet. The reason for cutting the pellets into this length, is that this length has shown to produce the smallest amount of dust and loose particles from the pellet during transportation [6].

To obtain an evenly distributed wear on the ring die, the pelleting material has to be distributed evenly across the ring die surface. If not, it would cause the production rate across the ring die to be unevenly distributed, causing high wear on the pellet channels with the highest production rates.

Pelleting Channel

A pelleting channel is divided into three sections:

- **1. section:** Inlet (chamfer)
- **2. section:** Press channel (cylindrical channel)
- **3. section:** Inactive channel (cylindrical channel with a larger diameter than section 2)

Figure 1.7 illustrates a cross sectional view of a pelleting channel. Section 1 and 2 are the active parts of the pelleting channel, while section 3 is an inactive part. The active sections affects the progress of the pelleting process. The total axial length of section 1 and 2 is named the active press length of the pelleting channel (l).

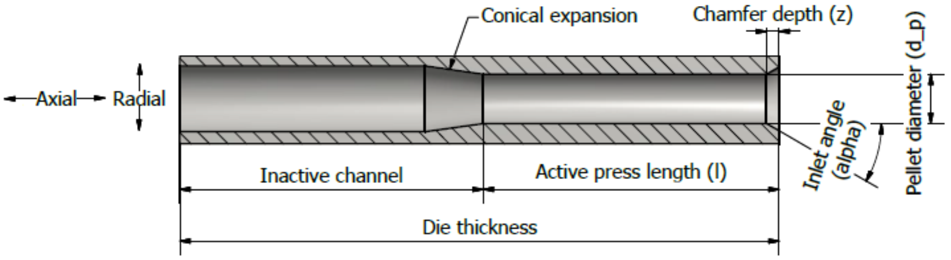

Figure 1.7: Cross sectional view of a pelleting channel.

Section 1 is the inlet of the pellet channel. The shape of the inlet is conical, and is specified by two parameters; the chamfer depth (z) and the inlet angle (α). All ring dies produced by Andritz Feed & Biofuel has an inlet angle of $\alpha = 30^o$. The chamfer depth varies dependent of the pellet channel diameter (d_p). Though there is no certain guideline for setting the chamfer depth. Normally the chamfer depth is in the range of $\frac{1}{4}$-$\frac{1}{5}$ of the pellet channel diameter. The chamfer reduces the flat area between the pellet channels. Without the chamfer, the increased flat area between pellet channels will cause high stresses between the roll and the ring die.

Typical values of the stress that the pelleting material is exposed to between the roll and the ring die is in the range of 150-300 MPa [6]. This value is referred as the load in the pellet mill, which is dependent of a number of parameters, which will be described in section 1.3.

Section 2 of the pellet channel is cylindrical. The diameter of this section determines the diameter of the produced pellets. By adjusting the length of section 2, the total friction between the wall of the pellet channel and the pelleting material can be regulated, which influences the load in the pellet mill. When pelleting biomass, the active part of the pellet channel is shorter than the ones used when pelleting livestock feed.

Section 3 is the inactive part of the pelleting channel. This part of the pelleting channel has a diameter, which is slightly larger (1-2 mm) than the diameter of section 2. There is no contact between the pellet surface and the wall of the pelleting channel in this section, causing no further compression of the pellet. The reason for having this part of the pelleting channel, is to add strength to the ring die, such that it can resist the stresses, that appears between the rolls and the inner surface of the ring die. The ring die is made of highly hardened alloys, which has a high yield strength. If the thickness of the die is to small compared to the stresses appearing between the ring die and the rolls, the ring die will be damaged and will eventually crack. The length of the inactive part is used for adjusting the strength of the ring die.

1.2.3 Densification of the Material

Through the pelleting process, the density of the pelleting material is raised by a factor of $\approx$ 10 when pelleting wood material [7]. The densification through the pelleting channel can be divided into three zones, which are illustrated in figure 1.8.

Compression zone: The grinded pelleting material, distributed on the inner surface of the ring die, is compressed between the rolls and the ring die. Before compression, the bulk density of the grinded wood material ranges between 120-170 $\frac{kg}{m^3}$, dependent of the species, particle size and MC [6]. The pelleting material resides in the compression zone as long as the resistance in the pelleting channel is higher than the stress applied by the roll. The resistance in the pelleting channel, is the force required to start pressing compressed material into the pelleting channel.

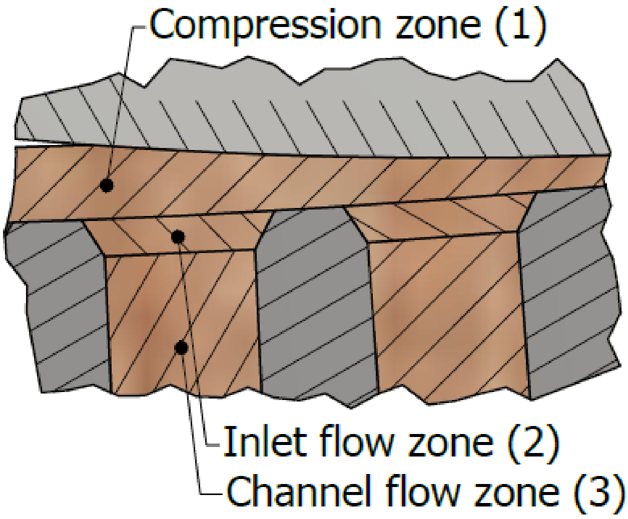

Figure 1.8: The three stages from grinded material to a densified pellet.

Published studies has shown, that the magnitude of the compression for biomass is limited by the density of the plant cell wall, which is in the range of 1420-1500 $\frac{kg}{m^3}$ [9] [10].

Inlet flow zone: Each time a pelleting channel passes a roll, a layer of compressed pelleting material is pressed into the pellet channel. Knowledge of how the inlet design affects the pelleting process is very limited. Though it has been shown, that small geometrical changes in the inlet zone rapidly changes the load conditions in the pellet mill.

Channel flow zone: The load in the pellet mill is determined by the resistance in the pelleting channel. The resistance is the frictional force between the wall of the pelleting channel and the pelleting material. If the resistance exceeds the value of the load that can be applied by the rolls, pelleting material can not be pressed into the pellet channel. This scenario causes the pellet mill to be blocked, and no pellets produced. The resisting force in the pellet channel is affected by multiple parameters, which will be described in section 1.3.

Besides providing a resistance due to the friction, the cylindrical channel causes the pelleting material to maintain the pellet shape, when the material exits the active part of the pelleting channel. The behavior of the pelleting material causes a small geometrical expansion of the pellet, when the stresses in the pellet are released. The expansion has by experience and studie shown to be dependent of the pelleting material, the load that is applied to it and its retention time in the pelleting channel [6] [11]. To minimize the expansion of the pellet, the retention time of the material in this zone has to be kept high enough for the material to maintain the pellet shape. Commonly, the retention time for the pelleting material in the active part of the pelleting channel is in the range of 4-7 seconds.

A laboratory study of a 8 mm pellet channel with an inlet angle of $\alpha = 30^o$ and a chamfer depth of $z = 2.5\,mm$, showed that the energy consumed in each of the three zones, represented by the following fractions [4]:

- Compression zone: $\frac{1}{6}$
- Inlet flow zone: $\frac{1}{2}$
- Channel flow zone: $\frac{1}{3}$

The energy consumption in pellet mills when producing wood pellets, is in the range of 45-70 $\frac{kWh}{ton}$ [6] dependent of the pellet mill, the degree of wear in the ring die, the pelleting material and its properties when entering the pellet mill.

1.2.4 Wear in the Pellet Mill

The ring die and the rolls in the pellet mill are exposed to a high wear. The durability of the parts in the pellet mill is dependent of the load in the pellet mill and the type of pelleting material. As mentioned in section 1.2.2, the load is in the range of 150-300 MPa, which for some types of steel and other alloys, is above the yield strength for compression. Therefore alloys with high yield strengths are used for the dies and rolls. The high load causes wear on the die and roll in a matter of a few hours of production. The wear on the die is concentrated in the inlet section of the pellet channel. To see how the wear appears in a pellet channel, a 3D scanning of a worn die with 8 mm pellet channels has previously been conducted by Andritz. Figure 1.9 shows the result of the 3D scanning.

Figure 1.9a is a cross sectional view of the scanned pellet channel, where the color contours illustrates the magnitude of the wear. The contours shows significant wear in the inlet of the pellet channel. The contours should only be evaluated in the pellet channel, and not the surrounding die material.

Figure 1.9b illustrates the upper 15 mm of the pellet channel wall, where the shape of the worn pellet channel (gray line) is compared to the original shape (colored line). The numbers in this figure represents the radial wear in mm.

The wear that is seen in figure 1.9 can appear after only a couple of hundred hours of production, dependent of the pelleting material and load in the pellet mill. The wear causes an increased load in the pellet mill, and will eventually cause a blockage of the pellet mill, if the ring die is not renovated or exchanged with a new ring die.

A die can be renovated 3-5 times before it is discarded. Renovating a ring die is done by machining the inner surface of the die, which removes the upper part of the pellet channels, that has been exposed to wear. After removing this layer of die material, new chamfers are drilled in all of the pellet channels. The renovation

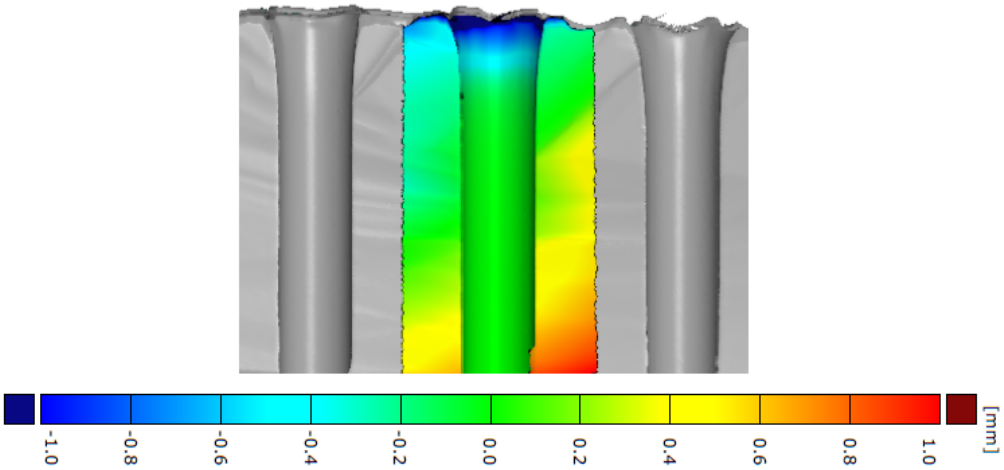

(a) Cross sectional view of the contours illustrating the wear in the pellet channel.

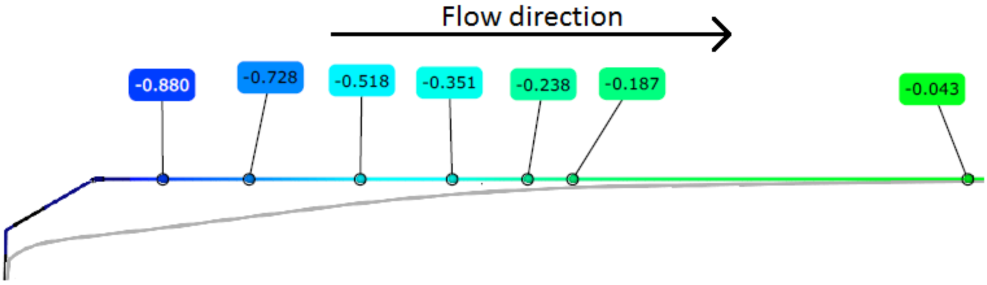

(b) Comparison of the original pellet channel shape (colored line) and the worn shape (gray line).

Figure 1.9: 3D scanning results of the wear in a pellet channel [6].

causes a shorter active part of the pellet channel, which influences the load in the pellet mill.

1.3 Pelleting Affecting Properties

The process in the pellet mill is affected by a number of properties for the pelleting material and the die design. Results of previous studies have shown, how some of these properties affects the process. These studies has primarily been focusing on the properties of the pelleting material. The following properties are known to affect the pelleting process:

- Wood type (species)
- Temperature
- MC
- Particle size and fiber orientation

The following sections will outline, how some of these properties affects the pelleting process.

1.3.1 Species

Wood used for pelleting is divided into two categories; hard- and softwood, where broad-leaved tree is defined as hardwood and coniferous tree is softwood. In table 1.2 examples of different wood species are listed. The type of biomass used as pelleting material highly affects the process parameters in the pellet mill.

Hardwood	**Softwood**	**Other**
Birch	Pine	Straw
Beech	Spruce	Grasses
Oak		

Table 1.2: Categories of biomass[1].

Pelleting of hardwood causes a higher load in the mill compared to softwood. Pelleting of straw causes a low load compared to pelleting of wood [7]. Studies of the friction between the pelleting material and the wall of the pellet channel has confirmed these experiences. Figure 1.10 shows the required pressure to push a compressed pellet in a pellet channel at temperatures in the range of 20-180 ^{o}C. This study was done with three types of biomass, each representing one of the categories in table 1.2. At temperatures below 130 ^{o}C, the beech pellet (hardwood) required the highest pressure in the test, while spruce (softwood) required $\approx \frac{1}{3}$ less pressure than the beech pellet at temperatures below 100 ^{o}C. The straw pellet required the

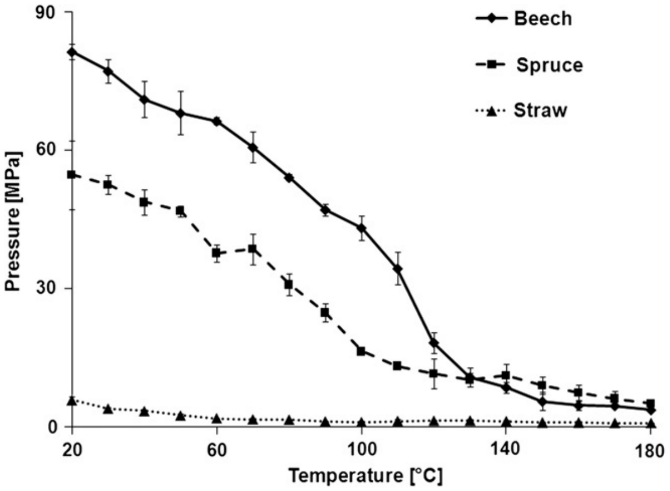

Figure 1.10: Required load to push a compressed pellet in the pellet channel at different temperatures [7].

least amount of pressure, which was significantly smaller compared to the two wood pellets.

The differences in the required load is mainly to be found in the composition of the species. Table 1.3 shows the composition of the species used in the test from figure 1.10.

Biomass type	**Cellulose (%)**	**Lignin (%)**	**Hemicellulose (%)**	**Extractives (%)**	**Ash (%)**
Beech	38.7	19.3	27.6	0.6	0.6
Spurch	41.3	21.6	22.2	1.8	0.6
Straw	37.8	29.6	19.1	4.4	4.6

Table 1.3: Composition of raw materials [12].

The compositional analysis shows the content of cellulose, hemicellulose, lignin, extractives and ash in the species. Lignocellulose is a designation of the total composition of cellulose, hemicellulose and lignin in a biomass. Lignocellulose is polymers that creates a structure surrounding the plant cell, which adds rigidity to the plant. Cellulose and hemicellulose are relatively short chained polymers compared to lignin[13]. The polymer structure of lignin is highly complex, and varies dependent of the species. Due to the long chain and complex structure, lignin is the main contributor to the rigidity of the plant. Using material with a high content of lignin, this can lead to an increased load in the pellet mill, since the rigidity of the pelleting material works against the deformation, that is necessary to form a pellet.

Besides lignocellulose, biomass contains extractives. Extractive is a term that covers multiple compounds as different acids and waxes. Extraction of these are for an example known as tall oil. A study by Stelte et.al [7] has linked the content of extractives in the pelleting material to the chemical composition of the pellet surface. The study was an ATR-IR spectra analysis of a beech, spruce, and straw pellet. Figure 1.11 shows the ATR-IR spectra results for the three types of pellets produced at 20 ^oC and 100 ^oC. The ATR-IR spectra analysis measures the absorption of light emitted at different wave lengths. The ability to absorb the emitted infrared light at different wave lengths, is linked to certain types of chemical compositions. Extractives as waxes and oils have been linked to high absorbance at wave lengths within the range of 2800-2900 cm^{-1} [14]. Figure 1.11a shows the ATR-IR results for the pellets produced at 20 ^oC, where extractives were only detected at the pellet surface of straw pellets. At 100 ^oC extractives were detected at the pellet surface for all of the three pellets, which is shown in figure 1.11b. The increase in extractive content on the pellet surfaces produced at higher temperatures, is caused by low weight molecules, as extractives [7][15], migrating to the surface of the pellets. Linking the content of extractives at the pellet surface to the pressures in figure 1.10, indicates a connection between the friction in pellet channel and the amount of extractives on the pellet surface. It is likely that the extractives at the pellet surface acts as a lubricant, which reduces the friction. The amount of extractives on the pellet surface also seems to be related to the total content of extractives in the biomass.

1.3.2 Temperature

The temperature of the pelleting material is a main parameter in the process. Increasing the temperature decreases the load in the pellet mill. Figure 1.10 shows that the pressure required to push a pellet in the pellet channel, decreases significantly for beech and spruce pellets when the temperature increases, while it is less dependent of the temperature for the straw pellet.

For industrial pellet mills it is not possible to directly control the temperature in the die. The temperature in the die is dissipated from the friction between the pellet and the die. The temperature can only be regulated by adjusting:

- The magnitude of friction, which is dependent of multiple parameters.
- The inlet temperature of the conditioned pelleting material.

There is no external cooling system connected to the die. The rolls in the pellet mill are connected to an external cooling system, to ensure that the temperature in the rolls does not exceed a critical temperature, which can damage the roller bearings in the rolls or reduce the durability. Observations from the industry has shown that the temperature of the die, when pelleting wood, is in the range of 90-120 ^oC [6].

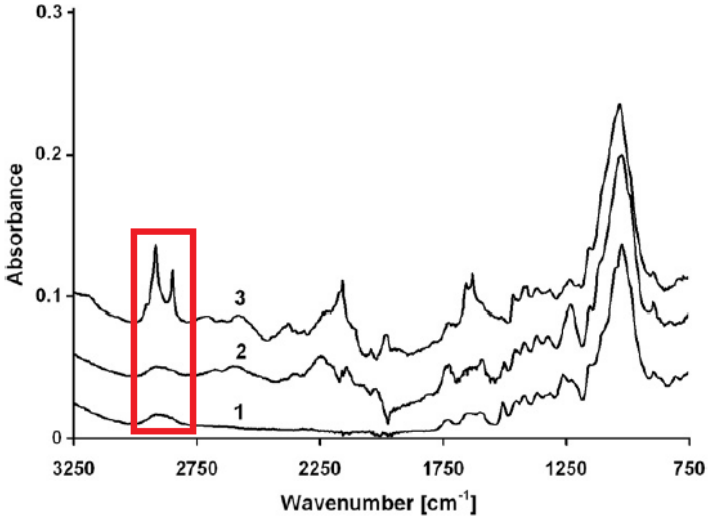

(a) Surfaces of pellets produced at 20 ^oC

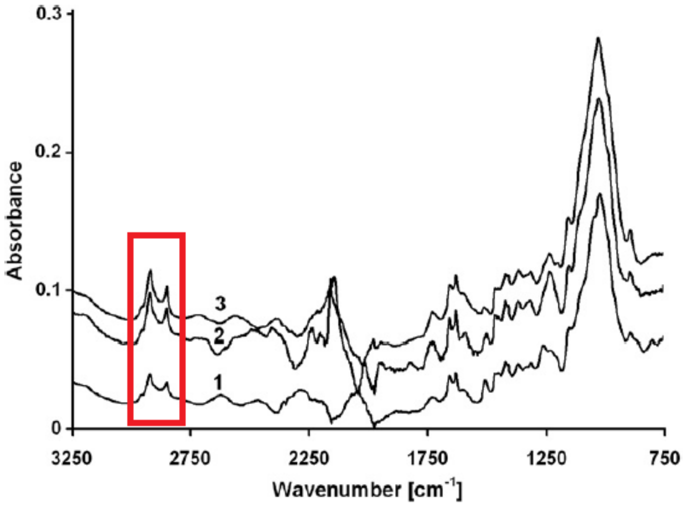

(b) Surfaces of pellets produced at 100 ^oC.

Figure 1.11: ATR-IR spectra analysis of the pellet surface of beech (1), spruce (2), and straw (3) [7].

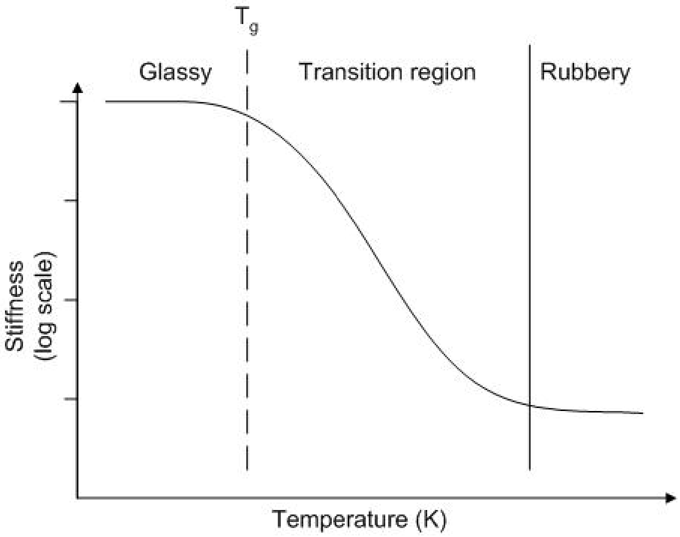

Figure 1.12: The transition between glassy and rubbery phase of a polymer [16].

When the biomass is pelleted, the plant fibers are deformed, which causes the rigidity of the pelleting material to affect the process. The rigidity of the lignin structure is affected by the temperature. Polymers as lignin undergoes a transition from a glassy phase to a rubbery phase when it is heated to a certain temperature. In case of lignin, this temperature is defined as the lignin transition temperature, T_g. Pelleting at temperatures above T_g, lignin is less rigid, and reduces the required load in the pellet mill [7]. In the rubbery phase lignin is more flexible, which causes more entanglement of the wood fibers in the pellet. More entanglement is favorable in terms of the pellet strength. Figure 1.12 illustrates the stiffness of a lignin polymer as a function of the temperature.

The transition temperature for lignin is dependent of the biomass species and the MC of the biomass. For wood T_g is in the range of 50-140 ^oC [7]. The chemical composition of lignin in hardwood causes a lower T_g compared to softwood.

The decreasing required pressure in figure 1.10 is caused by a combination of the extractives migrating to the surface at increasing temperatures and the softening of the lignin polymers.

Photos of pellets produced at 75 ^oC, 90 ^oC, 105 ^oC and 120 ^oC are shown in figure 1.13. The pellets are produced from eucalyptus tree with a $MC = 8.9\%$. The photos are taken from the 9th semester project [1], where pellets were produced with single dies in a laboratory. The photo in figure 1.13a shows a poor adhesion of the pellets produced at 75 ^oC, which causes the pellet to break into several parts. Figure 1.13b shows a better adhesion in the pellets produced at 90 ^oC, while an optimum is seen in figure 1.13c, where the pellets have a smooth surface without cracks. For the pellets produced at 120 ^oC are small cracks observed in the surface, which may be caused by a drying of the pelleting material. The color of the pellet surfaces in

(a) Pellets produced at 75 ^{o}C (b) Pellets produced at 90 ^{o}C

(c) Pellets produced at 105 ^{o}C (d) Pellets produced at 120 ^{o}C

Figure 1.13: Comparison of pellets produced at different die temperatures with two different die designs [1].

figure 1.13 tends to be darker when the temperature of the die is raised.

1.3.3 Moisture Content

The MC of the material is another key parameter in the pelleting process, which has been confirmed in a number of different studies [7] [8]. Lowering the MC causes a higher load in the pellet mill, while a high MC causes a bad pellet quality. In commercial pellet mills the pelleting material is conditioned to a $MC \approx 15\%$. Figure 1.14 shows that the required load in the pellet channel is affected by the MC. Lowering the MC of the pelleting material below 10% has shown to produce pellets with a bad adhesion, which is shown in figure 1.15. The figure shows poor adhesion of the pellets produced at $MC < 10\%$, likewise the pellets produced with $MC > 15$ also has a tendency of poor adhesion. The pellets produced at $10 \leq MC \leq 15$ can maintain the pellet shape, which indicates a good adhesion.

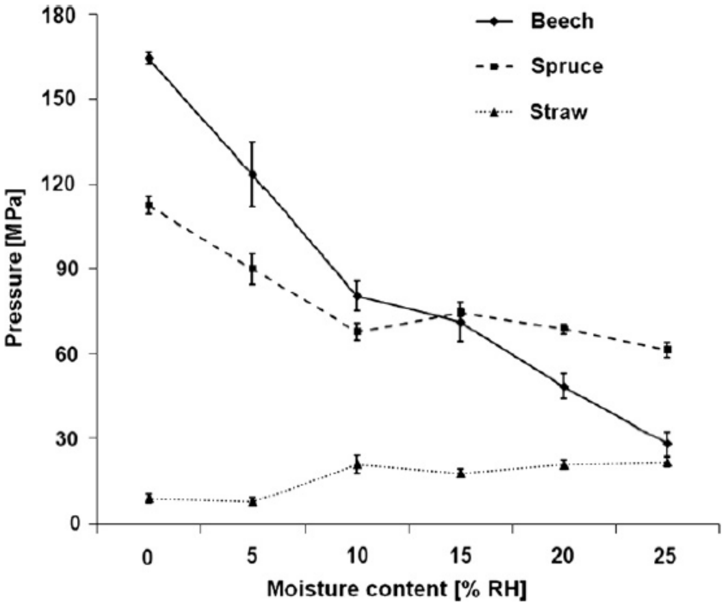

Figure 1.14: The pressure required to push a pellet in the pellet channel at 20 ^oC [7].

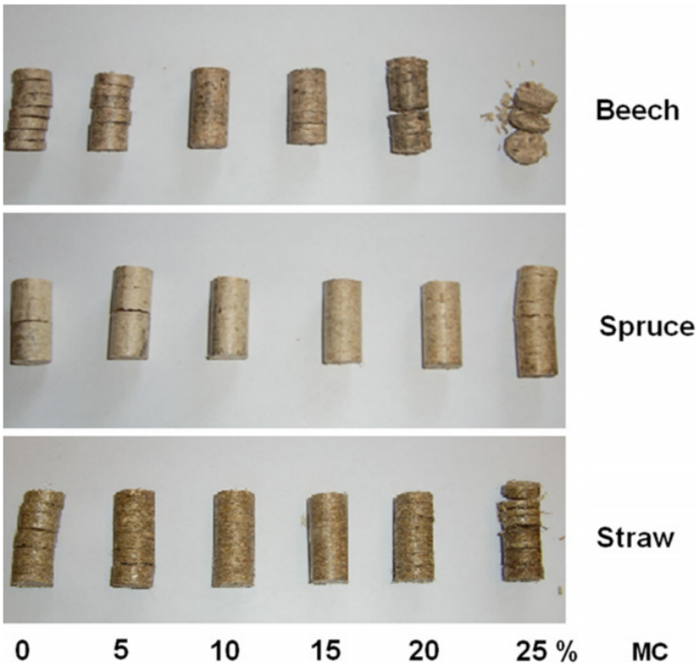

Figure 1.15: Pellets produced at various MC [7].

1.3.4 Pellet Quality

When speaking of pellet quality, the measure is defined as the adhesion of the biomass particles. A poor adhesion will cause particles to loosen from the pellet and create dust during handling and transportation. The adhesion and bonding of the particles in the pellets are caused by multiple phenomenons. A flow chart of the adhesion process is shown in figure 1.16.

Two ways of defining the pellet quality are described below.

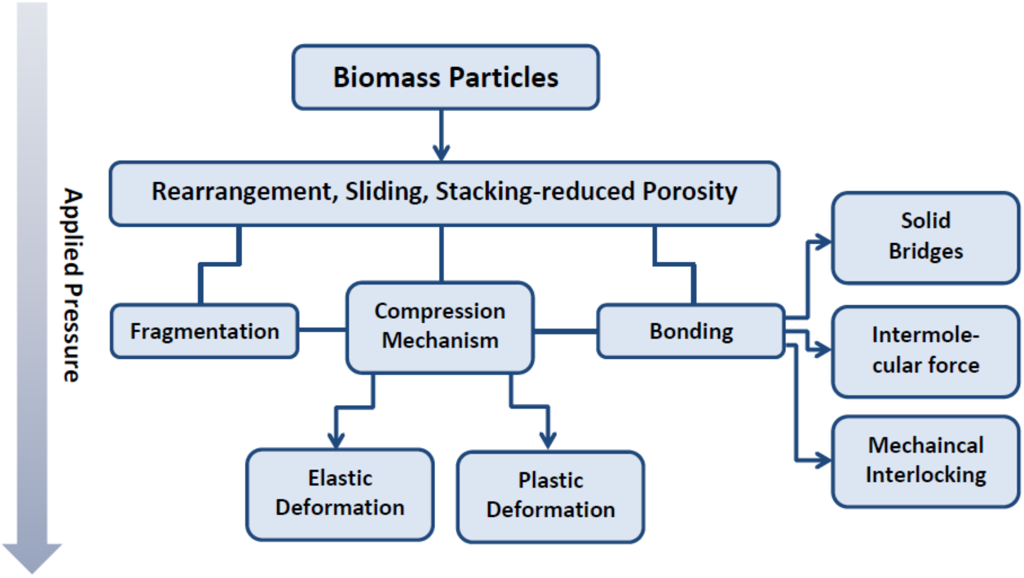

Figure 1.16: Deformation mechanisms of powder particles under compression [17] [18].

Industrial Quality Test

The standard method of measuring the pellet quality is the pellet durability index (DPI)[19], where a batch of pellets is tumbled in a tumbler. A high DPI corresponds to a good pellet quality, where the weight of the pellets is retained during the tumbling, meaning that a small amount of material is loosen from the pellets.

Single Pellet Quality Test

The DPI technique is desirable for industrial production, where a large amount of pellets are produced. For small scale testing in laboratories is the pellet quality often measured on a single pellet. This method has been used in multiple studies [7][8][20], and is performed by applying a radial force to the pellet, and measure the force that has to be applied before the pellet breaks. This force is a measure of the pellet quality, where a high force corresponds to a good quality. The method is illustrated in figure 1.17.

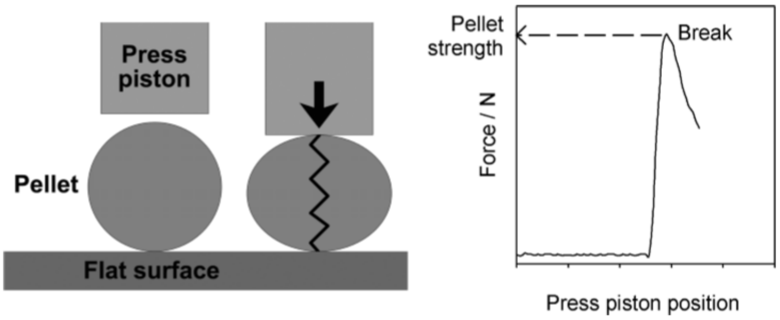

Figure 1.17: Method of testing the pellet quality on a single pellet [20].

1.4 Conclusions from Previous Semester

The main focus of the 9$^{\text{th}}$ semester project was:
How is the pelleting pressure affected by temperature and the inlet design of the die?

The project was primarily carried out with experimental work, where pellets were produced with twelve different die designs. The required force for producing pellets in each of the dies were measured, and the energy consumption for the production of the pellets were determined. The main conclusions of the die inlet design tests were:

- The load that was applied to the dies, in order to extrude pelleting material into the die, was lowest for the die without any inlet ($\alpha = 0^o$ (90^o), $z = 0\,mm$).
- Dies with deeper inlets (increasing z-values), and inlets with low values of α required a higher load.
- The specific energy consumption of the pelleting process $\left[\frac{J}{kg}\right]$, seems to be proportional to the pelleting load.

Figure 1.18 shows the measured pelleting load for the twelve dies. The black lines in figure 1.18b represents the standard deviation of the measurements.

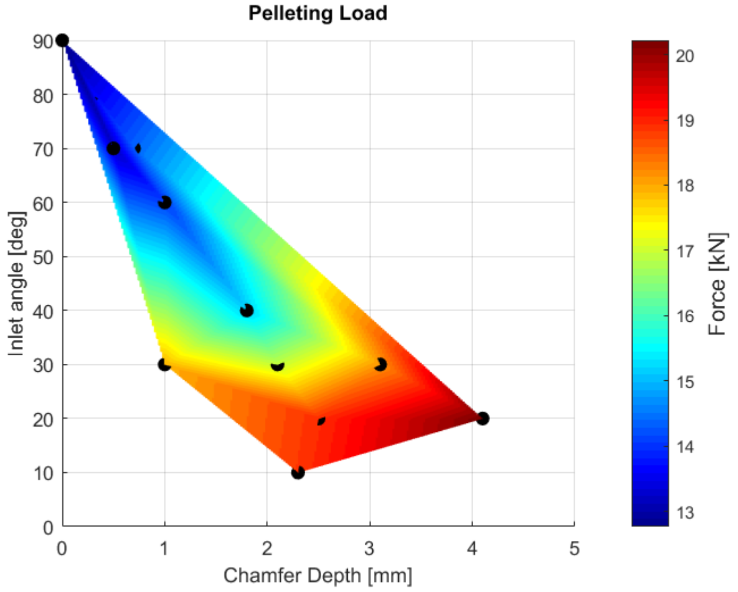

(a) View one.

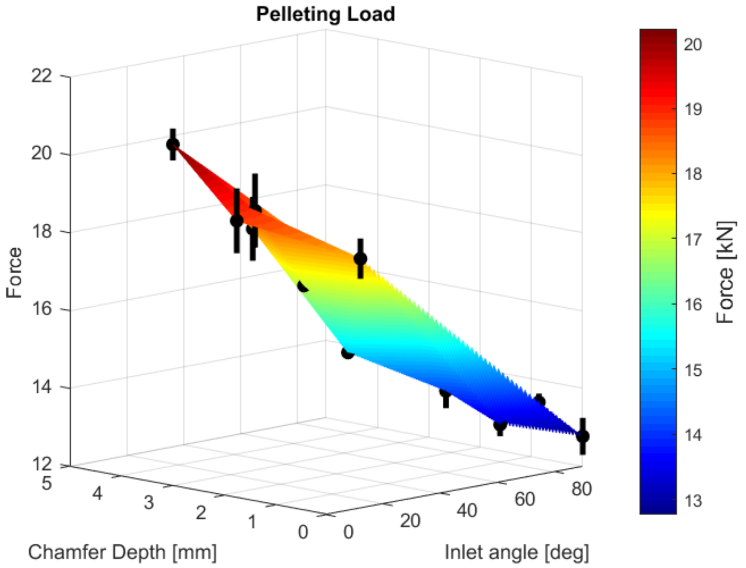

(b) View two.

Figure 1.18: The measured pelleting load.

Project Definition

The purpose of this project is to generate useful knowledge of the pelleting process, focusing on how the design of the pellet channel affects the pelleting load. This project is the first step in the process of being able to simulate the pelleting process. The main challenge for this project is, that there only is a limited amount of knowledge available, and therefore the following major limitations is set for the project:

- The numerical models will only account for the active part of the pellet channel.
- The particle size of the material is neglected.
- The model will be divided into a number of elements, where each element has the material properties of the simulated biomass.
- Effects of temperature and MC are neglected.

Up to now, previous studies has treated the pellet channel as a ”black box”, where only in- and outputs are evaluated. With this project it is wanted to clarify the processes inside the pellet channel. The available data of pelleting with different pellet channel designs, is limited to the results of the 9th semester project [1]. These data does not provide any information of the pelleting material inside the pellet channel, which is why new experiments will be set up.

The new experiments and results from the 9th semester, combined with the numerical models, will provide a useful insight in the pelleting process inside the pelleting channel.

From the present knowledge of the pelleting process, the following problem definition is set for the project:

How does the inlet design of a pellet channel affect the pelleting process?

The goals for the project is to:

- Set up an empirical model to determine the compression behavior of the pelleting material.
- Obtain knowledge of how the pelleting material is affected by the design of the pellet channel.
- Set up experiments, from which the local density of the pelleting material can be measured in the pellet channel.
- Set up numerical models which can simulate the pelleting material in pellet channels, and determine the required pelleting load.

The models will be coded in the software named *Matlab*.

CHAPTER 2

Experiments

The experiments that have been done during this project, and the results of these are presented in this chapter. The experiments are divided into two sections. The purpose of the first experiments was to obtain an empirical function, which defines the density of the pelleting material as a function of the applied pressure, and to set up an expression which can calculate the amount of work required for compressing the pelleting material. The empirical function will be used to calculate the density and the amount of compressional work. These will be implemented in the numerical models.

The purpose of the second set of experiments, is to measure how the density in the pellets is affected by the die design, and to get an understanding of, how the pelleting material flows in the pellet channel. The results of these experiments will be used for comparison and validation of the numerical models.

2.0.1 Pelleting Material

The material used for the tests in this project is eucalyptus tree. The material is taken from a 20 kg batch that was provided for the single pellet test conducted in the 9$^{\text{th}}$ semester. A new measurement of the MC was conducted in order to ensure that the material properties are comparative to the properties from the single pellet test. The test procedure of the drying test is described in appendix 4.1.1, where the results of the previous MC-measurement also is presented. The result of the new MC-measurement is shown in table 2.1. The new measurement shows that the MC of the pelleting material is reduced by 0.3% (before $MC = 8.9\%$) since the first experiments was conducted. Despite the small change in MC, the material is assumed to be comparable to the material used for the single pellet tests. Figure 2.1 shows the pelleting material used for the test.

Sample no.	$M_{(w.b.)}$ $[g]$	$M_{(d)}$ $[g]$	$MC\%(w.b.)$ $[-]$
1	20.00	18.30	8.50%
2	20.00	18.26	8.70%
Average	20.00	18.28	8.60%

Table 2.1: Results of the MC measurements.

Figure 2.1: Grinded eucalyptus tree used for the tests. The longest of the grinded wood fibers are $\approx$ 6 mm.

2.0.2 Test Unit

The tests was done in the material laboratory at Aalborg University Esbjerg. The compression tests was carried out on a LLOYD LR50K tensile and compression station. Figure 2.2 shows the test unit. The test unit is equipped with a heating chamber, which allows the temperature of the test facility to be controlled during the tests. It can apply a compressible load up to 50 kN.

2.1 Compression Tests

As mentioned in section 1.3.2, the operative temperature of the ring die is in the range of 90-120 ^oC when pelleting wood. To ensure that the compression test is conducted at conditions similar to those in a industrial pellet mill, the heating chamber is set to a temperature of 100 ^oC.

2.1.1 Test Procedure

The equipment used for the compression test consists of the following parts which are made out of stainless steel:

- **Cylinder** - The cylinder acts as a press channel, where pelleting material is added and compressed. The diameter of the cylindrical channel is 9.5 mm and

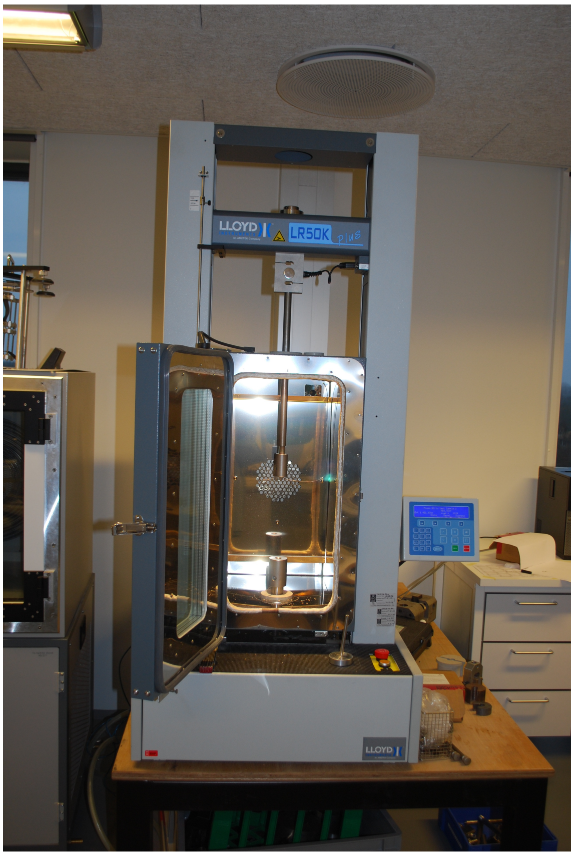

Figure 2.2: The LLOYD LR50K station equipped with the heating chamber.

has a length of 90 mm.

- **Press piston** - The press piston fits in the cylindrical press channel, and compresses the pelleting material when a load is applied to the upper end of the piston. The press piston is a 120 mm long rod. The lower end diameter of the press piston is fitted to the diameter of press channel (9.5 mm), while the diameter of the remaining part is narrowed down by 2 mm to minimize the contact area between the press piston and the wall of the press channel.

- **Stop piston** - The stop piston is a 5 mm long rod, placed in the bottom of the press channel. The diameter of the stop piston has the same diameter as the press channel. The stop piston acts as a stop block in the cylinder, which causes the pelleting material to be compressed between the press- and stop piston and the walls of the press channel.

The compression test is carried out in two steps, which are illustrated in figure 2.3. In the first step is a weighed amount of pelleting material added in the cylinder, which is illustrated in figure 2.3a. Figure 2.3b illustrates the next step, where a load is applied to the press piston and compresses the pelleting material. The maximum load added to the press piston is set to 21 kN, in order to avoid deformations of

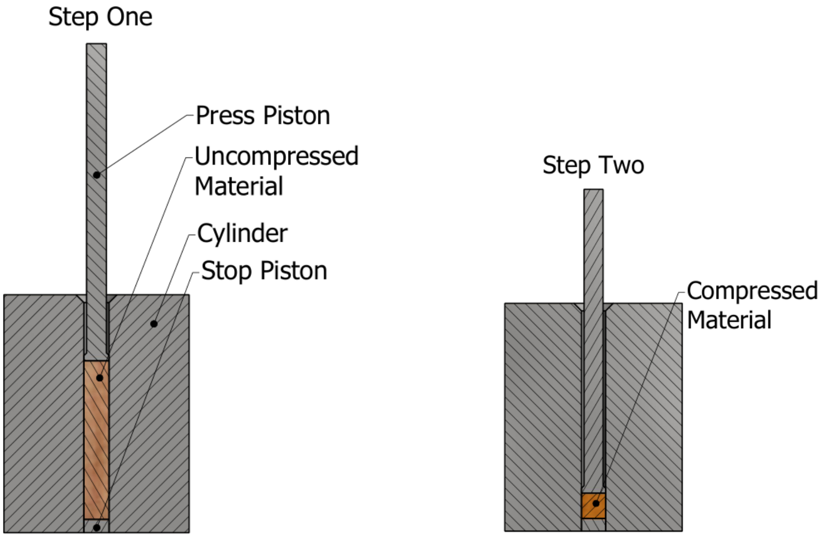

(a) Step one. (b) Step two.

Figure 2.3: Test procedure of the compression test.

the press piston. See appendix 4.1.2 for calculations of the stresses applied to the press piston and the pelleting material. The maximum load corresponds to a stress of $\approx 300\ MPa$, which is within the maximum load applied in pellet mills.

During the compression 200 data points are logged. Each data point provides information of the press piston position and the corresponding force applied. The compression speed is set to $100\frac{mm}{min}$. The reason for not increasing the compression speed, is to be able to stop the test in time, if breakage of failure of the setup occurs.

The compression test was conducted with three different amounts of pelleting material, and each amount was tested three times to ensure a more statistical valid result. The three amounts that were compressed is 0.30, 0.74 and 1.00 g. The reason for testing three different amounts is to check if the amount of pelleting material compressed affects the required amount of work.

2.1.2 Results

The result of the compression tests are shown in figure 2.4, where 2.4a shows the force applied to the press piston and the corresponding position of the piston. The reason for the curves to be displaced from each other, is that the initial position of the press piston varies dependent of the amount of pelleting material in the cylinder. Figure 2.4a shows that there is almost no variations within the three tests of each amount tested. To compare the nine compression tests, the force applied to the sample is converted to a pressure. The pressure in the sample is defined by the formulation commonly used in thermodynamics, where the pressure is equal to the average of the normal stresses acting on the volume. The pressure in the biomass sample is defined by equation 2.1, where:

- P is the pressure of the pelleting sample $[Pa]$
- σ_{axi} is the normal stress acted from the piston in the axial direction $[Pa]$
- σ_{rad} is the normal stress appearing at the walls of the cylinder in the radial direction $[Pa]$
- F_{axi} is the force applied from the press piston during the compression $[N]$
- A_{axi} is the cross sectional area of the press piston $[m^2]$
- F_{rad} is the force acting normal to the wall of the cylinder, due to an radial expansion of the pelleting material $[N]$
- A_{rad} is the area of the interface between the wall of the cylinder and the pelleting material $[m^2]$

$$P = \frac{1}{3} \cdot (\sigma_{axi} + 2 \cdot \sigma_{rad}) = \frac{1}{3} \cdot \left(\frac{F_{axi}}{A_{axi}} + 2 \cdot \frac{F_{rad}}{A_{rad}} \right) \tag{2.1}$$

The method used for calculating σ_{rad} will be presented in chapter four. The position of the press piston is related to the material density, which is calculated with equation 2.2, where

- ρ_p is the density of the pelleting sample $\left[\frac{kg}{m^3}\right]$
- h is the height of the compressed pelleting sample in the cylinder $[m]$
- m is the mass of the pelleting sample $[kg]$

$$\rho_p = \frac{m}{A_{axi} \cdot h} \tag{2.2}$$

Figure 2.4b shows the calculated densities as a function of the pressure in the pelleting material. It shows that the amount of pelleting material slightly affects how the density changes with pressure, but there is no immediate explanation of the relation between the three curves. There are a number of uncertainties which can affect the result of the compression test. One of the major uncertainties could be the orientation and packing of the wood fibers in the cylinder, which probably differs in each test. It is seen in figure 2.4b that there is a larger deviation between the plotted curves for the small sample (0.30 g) compared to the two larger samples (0.74 g and 1.00 g). This can be caused by the weighted amount of pelleting material, where small deviations will have higher significance for small samples compared to larger samples.

To set up an empirical expression for the density of the pelleting material as a function of the pressure, the nine curves plotted in figure 2.4b are averaged. Regression of the data from the compression test shows, that the density as a function of

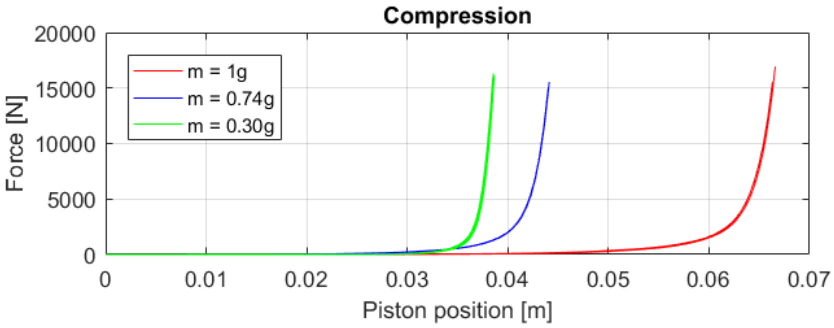

(a) Piston force plotted as a function of the press piston position.

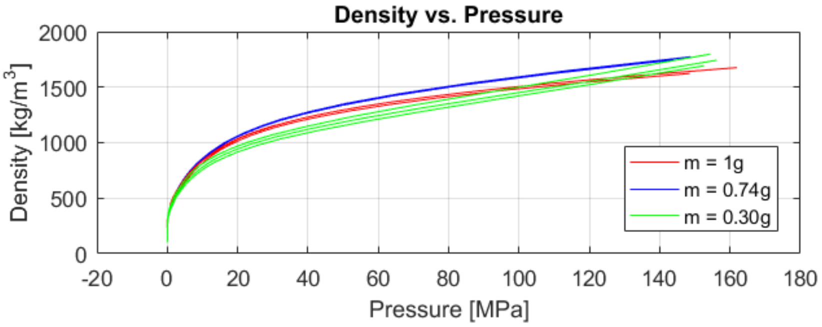

(b) Density of the pelleting material as a function of applied pressure.

Figure 2.4: Data from the compression tests.

the pressure can be described by a power function, which form is shown in equation 2.3, where:

- k_1, k_2 and k_3 are empirical constants.

$$\rho_p = k_1 \cdot P^{k_2} + k_3 \tag{2.3}$$

It was assumed that the empirical function should have a form, which has a horizontal asymptote, that defines the maximum density which the pelleting material can reach [17]. As described in section 1.2.3, the maximum density of compressed biomass is ≈ 1420-1500$\frac{kg}{m^3}$. Extrapolating the empirical function in equation 2.3 above the tested values for pressure, will not lead to any maximum value of the density. Instead the density will continue to increase, when the pressure increases. In order to avoid extrapolation above the logged data, the calculation of the density in the numerical models will be locked when the pressure exceeds this limit.

The averaged values from the test are plotted with the empirical power function in figure 2.5a, where:

- $k_1 = 318.989$
- $k_2 = 0.324$

- $k_3 = 82.694$

Since the nine data curves are averaged into one curve, the standard deviation of the density values are plotted for the data points in figure 2.5a.

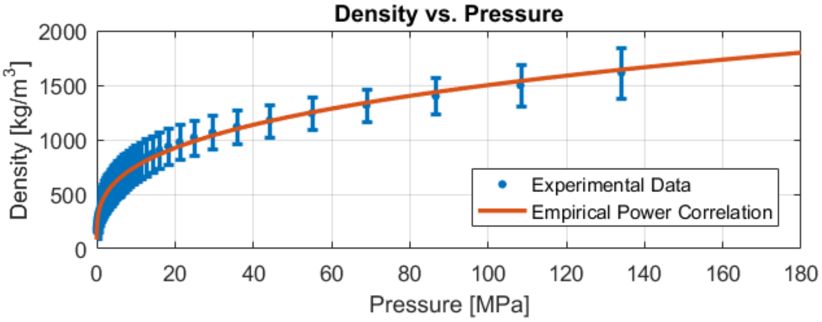

(a) Empirical density function.

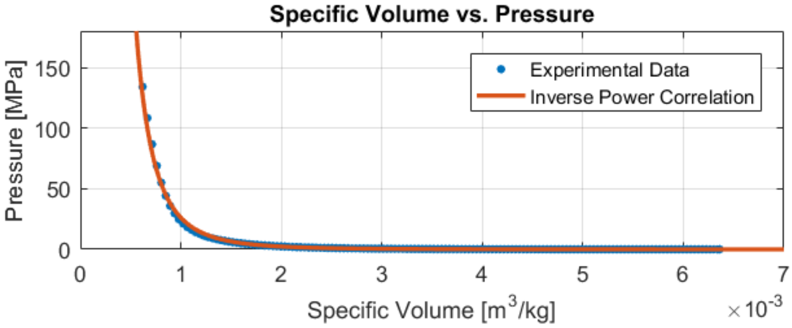

(b) Inverse empirical function for the specific volume.

Figure 2.5: Empirical functions of the density and specific volume for the pelleting material.

The empirical function plotted in figure 2.5a can be used for calculating the density of the pelleting material in the numerical models.

The second purpose of the compression test was to set up an expression that can describe the amount of work exerted to the pelleting material during compression. This will be done by setting up an expression for the pressure as a function of the specific volume of the pelleting material, where integration between two values of the specific volume defines the work. A study done by Nielsen et. al [8] has used a similar approach, for determining the compressional work from a compression test.

First is an expression for the specific volume set up, which is shown in equation 2.4, where:

- V_s is the specific volume of the pelleting material $\left[\frac{m^3}{kg}\right]$

$$V_s = \frac{1}{\rho_p} = \frac{1}{k_1 \cdot P^{k_2} + k_3} \tag{2.4}$$

Taking the inverse of the function shown in equation 2.4, the expression in equation 2.5 is obtained.

$$P = \left(\frac{1}{k_1 \cdot V_s} - \frac{k_3}{k_1} \right)^{\frac{1}{k_2}} \tag{2.5}$$

The pressure as a function of the specific volume is shown in figure 2.5b, where the work exerted for the compression can be determined by integration.

2.2 Pellet Structure Test

This experiment has been set up, in order to provide knowledge of how the pelleting material behaves inside the pellet channel.

Generally the knowledge of the processes occurring inside the pellet channel are very limited, which is why these tests are set up.

2.2.1 Test Procedure

Three dies with different inlet designs have been selected for this test. The three dies were among the dies used for the experiments conducted in the 9th semester project [1]. In table 2.2 the dimensions of the three dies are listed. The selected dies represents a span of different inlet angles and chamfer depths.

Die no.	**Inlet angle** (α) [^{o}]	**Chamfer depth** (z) [mm]	**Volume of plug** [mm^3]	**Mass of plug** [g]
3	20	2.5	207.4	0.311
6	30	2.1	246.5	0.370
11	70	0.7	199.2	0.299

Table 2.2: Dimensions of the three dies used for the Pellet Structure Test.

The experiment is proceeded in three steps, which are illustrated in figure 2.6 where:

- **Step one** is shown in figure 2.6a. Pelleting material is compressed in the inlet of the die. A stop piston is placed in the pellet channel of the die, in order to provide a blockage causing the pelleting material to be compressed to a plug by the press piston. The press piston is stopped 0.5 mm above the die inlet.
- **Step two** is shown in figure 2.6b. 0.5 g of pelleting material is added on top of the compressed material, and the stop piston in the pellet channel is removed.
- **Step three** is shown in figure 2.6c. The pelleting material added in step two, is compressed and forced into the pellet channel, forming a pellet.

The amount of pelleting material which is compressed in step one, is listed in table 2.2. The reason for using different amount of pelleting material, is to obtain an even density (1500 $\frac{kg}{m^3}$) of the plugs compressed in the inlet of the three dies.

When the pelleting material in step three is compressed, the pellet is pushed out of the pellet channel. For each die, three pellets were produced.

One pellet from each die was embedded in epoxy. After two days, the epoxy was hardened, and the pellets were planed down until a cross sectional view of the

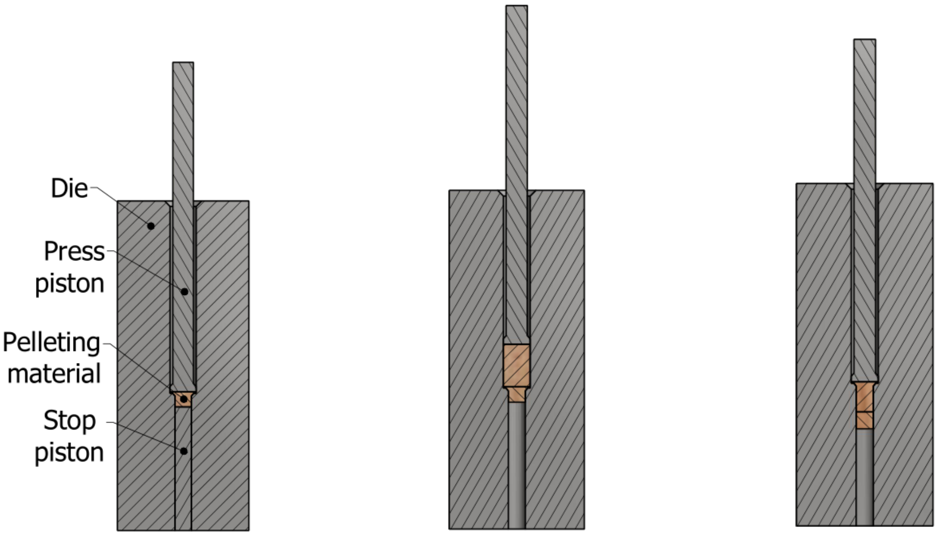

(a) Step one. (b) Step two. (c) Step three.

Figure 2.6: Test procedure for the pellet structure test.

pellets were obtained. Abrasive paper of different grit sizes were used to get a smooth surface of the pellet cross sections. Figure 2.7 shows two embedded pellets.

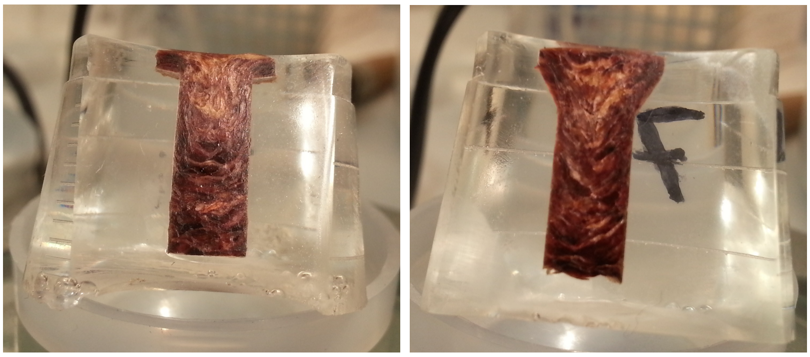

(a) Pellet from die no. 12. (b) Pellet from die no. 7.

Figure 2.7: Embedded and sanded pellets.

The embedded pellets are evaluated in two ways. First the pellets are photographed in a magnifier with 10 x zoom, and evaluated visual. Next the the hardness is tested by measuring the deformation, when applying a force to the pellet.

2.2.2 Visual Results

Photographs of the magnified pellets, produced in the three dies are shown in figure 2.8.

Looking at the cylindrical part of the pellet channel in figure 2.8 shows that there are differences in the orientation of the fibers for the three pellets. The fact that the fiber orientation varies can be an explanation of the differences in the required load

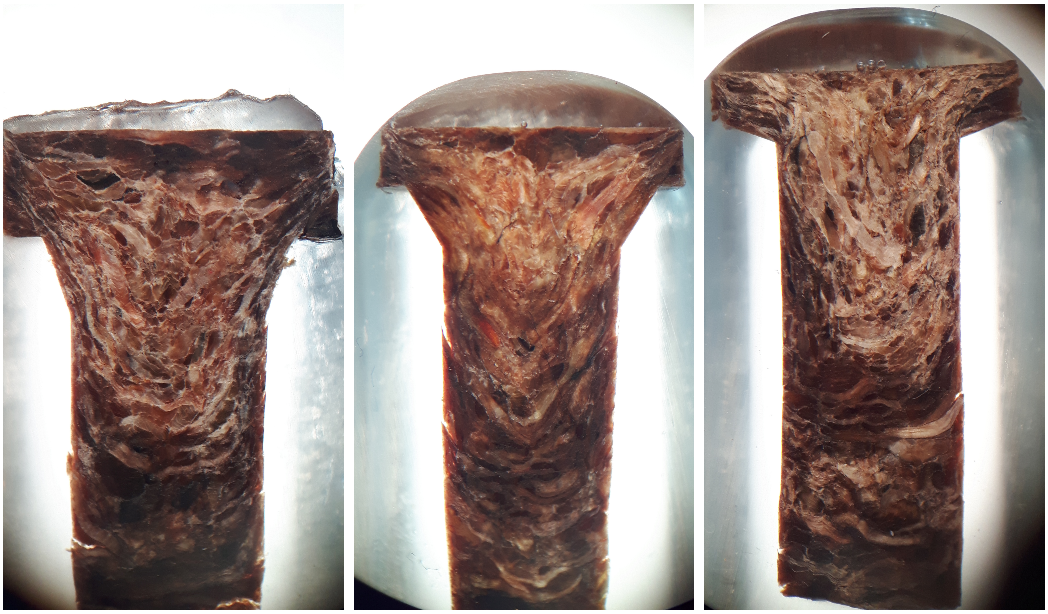

(a) Die no. 3. (b) Die no. 6. (c) Die no. 11.

Figure 2.8: Photos of magnified pellets.

when using different die designs. The fibers seems to form a more or less parabolic curve, dependent of the inlet design. To visualize the differences, trend lines are added to the fiber orientation in figure 2.9. The trend lines are based on visual inspection of the pellets.

Generally for the photos of the magnified pellets are, that the pelleting material seems to be divided into two regions just above the inlet. The first region is the area, which is outlined by the outer trend lines. This region seems to be stagnant, while the pelleting material between the two outer trend lines seems to flow into the die. This is a common phenomenon in extrusion processes, when extruding solids like metals or plastics through a die [21]. The color of the stagnant region is darker than the flow region, which can be caused by its large contact area with the heated die. The fact that pelleting material darkens at higher temperatures, can also explain why the bottom of the pellets are darker than the upper part, since the material in the bottom comes from the first compression (step one in the test procedure), and therefore has been located in the die for a longer time. The shape of the stagnant region seems to be related to the inlet design of the die.

For the pellet produced in die no. 11, only the two outer trend lines are added, since no pattern of the fibers are observed. This may be caused by the material not being affected by the inlet design of the die, and therefore the fibers are extruded directly into the die.

The trend lines for the pellets produced in die no. 3 and no. 6 have similar tendencies. The ones in die no. 6 are steeper, compared to the ones for die no. 3. It can be imagined that the fiber orientation affects how much shear, that has to be

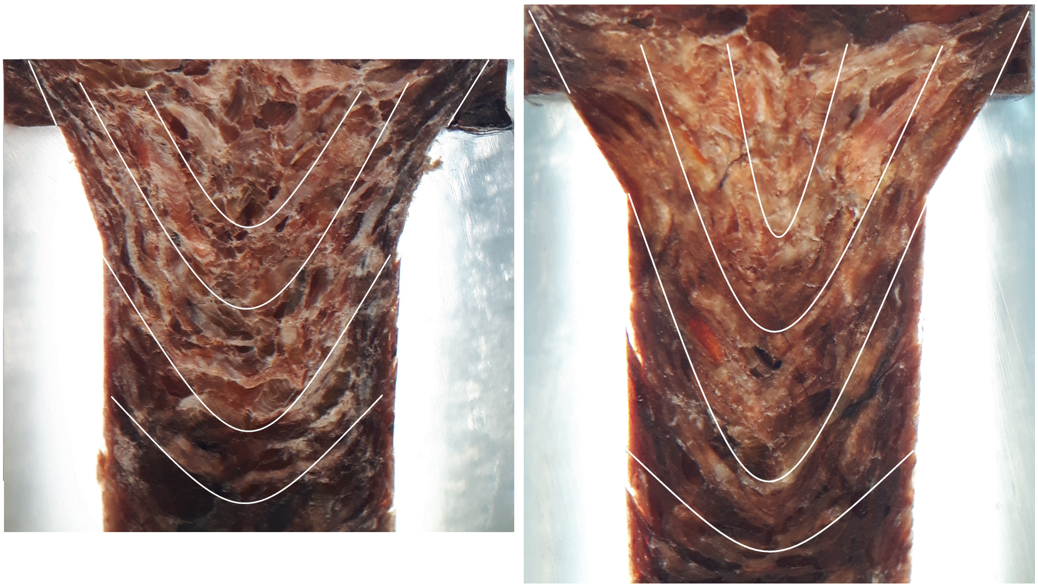

(a) Die no. 3. (b) Die no. 6.

(c) Die no. 11.

Figure 2.9: Trend lines of the fiber orientation.

applied in order to break the bonding between the fibers. The reason for the lowest trend lines not having the same profile as the upper lines, is because the embedded pellets only consist of two layers of pelleting material. The material in the bottom of the pellets has not been extruded into the pellet channel like the upper material.

2.2.3 Hardness Test

To determine if the pelleting material is compressed evenly in the pellet channel, the hardness of the embedded pellets is measured. The hardness is measured with a digital hardness meter, which measures the deformation of the material, when a geometric shape is forced into the surface of the material. The unit used for the hardness test is a Durotech M202 hardness meter.

There exists a number of different methods for measuring the hardness of a material. The most well known are rockwell and brinell. The measuring unit used for these tests, outputs a number within the range of 0.00-3.00, where 3.00 corresponds to no deformation, and thereby a hard material. Different types of geometrical shapes can be used for the deformation. It is expected that the pellet structure is very inhomogeneous, and the hardness will vary whether if the deformation is applied on top of a fiber or between two fibers. In order to minimize this uncertainty, the geometrical shape is chosen, such that it covers a larger area of the pellet.

It is expected that the density of the pelleting material is related to its hardness. In order to test this, 0.9 g samples of pelleting material were compressed to five different densities. Three samples of each density were produced. The samples are compressed similar to the procedure done in the compression tests (section 2.1).

The hardness of the samples are measured and compared to the density, in order to determine if there is a relation between the two properties.

The compression station was set for five different loads, which resulted in five different densities. After compression, the dimensions of the cylindrical samples were measured, and the final density of the samples were calculated. In table 2.3 the calculated densities of the 15 samples are listed.

	Sample Density $\frac{kg}{m^3}$			
Sample No.	**1**	**2**	**3**	**Average**
Load 1	1459	1452	1463	1458
Load 2	1408	1411	1403	1408
Load 3	1312	1309	1315	1312
Load 4	1232	1238	1230	1233
Load 5	1181	1185	1176	1181

Table 2.3: Calculated densities from the compression samples.

Like the pellets, the compression samples were embedded in epoxy and planed down. Figure 2.10 shows photographs of a sample from load no. 1, no. 3, and no. 5, which have the densities 1458, 1313 and 1181$\frac{kg}{m^3}$.

Besides of the size, it is hard to determine any visual differences between the three compression samples in figure 2.10. The hardness is measured at 18 locations

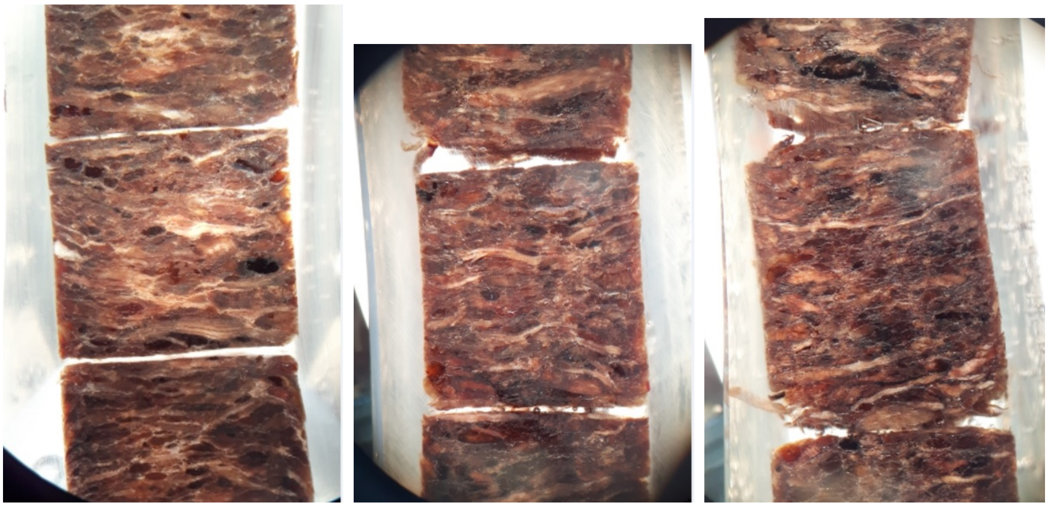

(a) $\rho = 1458\frac{kg}{m^3}$. (b) $\rho = 1313\frac{kg}{m^3}$. (c) $\rho = 1181\frac{kg}{m^3}$.

Figure 2.10: Photos of magnified compression samples.

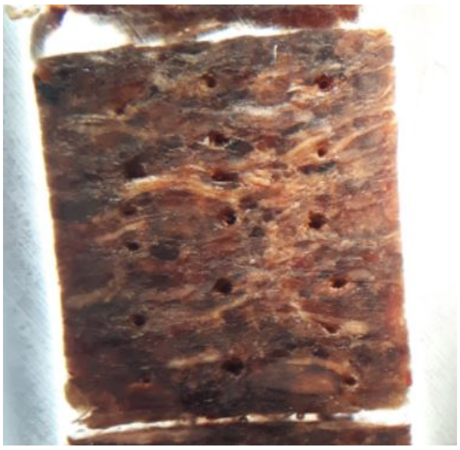

Figure 2.11: The measuring locations represented by the deformation holes in the sample.

for each of the 15 compression samples; six along the center axis, and six on each side of the center axis (named east and west axis).

The compression samples are assumed to have a uniform density, and therefore the output of the hardness measurement should be independent of the measuring location in the sample. Though, since the compression samples are cylindrical, the amount of pelleting material supporting below the measuring plane varies across the radial direction, which can lead to deviations in the measurements across the samples. Figure 2.11 shows one of the compression samples after measuring the hardness. With the hand held hardness meter it is hard to hit the exact same measuring locations in each sample.

Hardness of Compression Samples

To evaluate the result of the hardness measurements, the average value and standard deviation for each of the three measuring axises are calculated for each of the five densities. The values are shown in figure 2.12, where the error bars represents the standard deviation, and the x-marks are the average values of the 18 measuring values in each axis (center, west and east). Figure 2.12 shows that the average hardness of the center axis generally is lower compared to the east and west axis. This can be caused by the radial stresses being larger near the wall, compared to the center. Though it should also be minded, that the layer of pelleting material supporting below the measuring plane in the center compared to the east and west axis are thicker. In the east and west axis, a thinner layer of pelleting material separates the measuring plane and the hard epoxy.

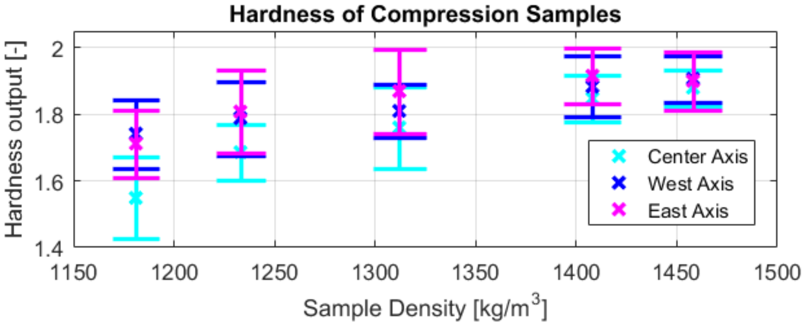

Figure 2.12: Result of hardness measurements for the compression samples.

It is seen in figure 2.12, that the standard deviation reduces at higher densities, which means that more homogeneous compression samples are produced, when they are exposed to higher compressions.

Figure 2.12 shows a tendency of the average hardness to increase, when the density of the pelleting material is raised. Therefore the hardness of the pellets, can be used as an expression for the local density in the pellets.

Hardness of Pellets

In order to determine how the inlet design affects the density in the pellet, hardness measurements are conducted for three pellets, which each were produced in one of the three dies listed in table 2.2. Since the inlet design is different in the three dies, the measuring locations in the inlet section can not be identical for the pellets produced in the three dies, and even to obtain the exact same measuring locations for the dies will be almost impossible, due to the small size of the pellets. Therefore the measuring locations are mapped for each pellet by reading the coordinates of the measuring locations from magnified pictures of the pellets.

Figure 2.13 shows a pellet produced in die no. 3, 6 and 11, and the measured hardness at the measuring locations. The measurements are represented as dots, where the color represents the hardness. Due to the small count of measuring locations at each pellet, the hardness data is not interpolated into a grid, covering the entire cross section of the pellet.

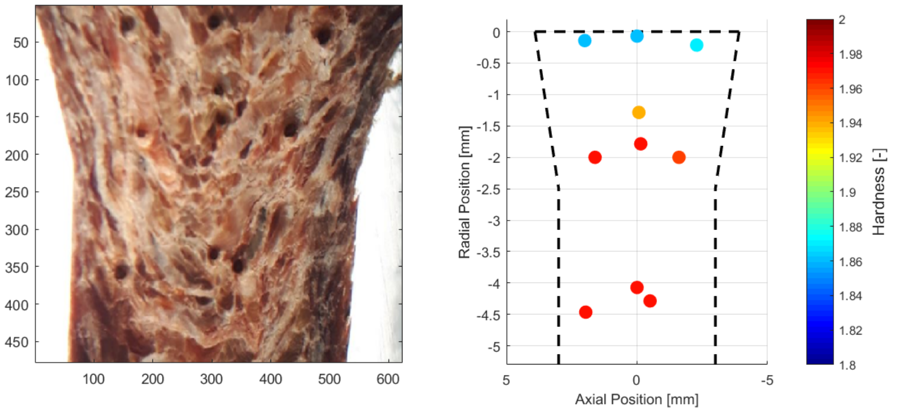

(a) Magnified picture (die no. 3). (b) Plotted hardness (die no. 3).

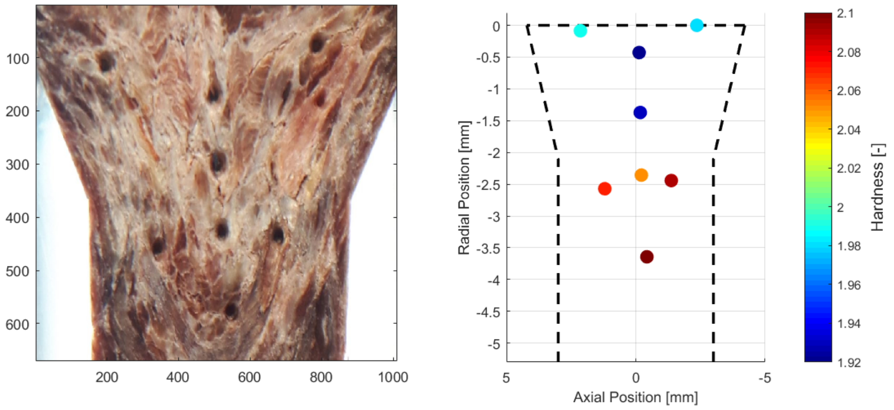

(c) Magnified picture (die no. 6). (d) Plotted hardness (die no. 6).

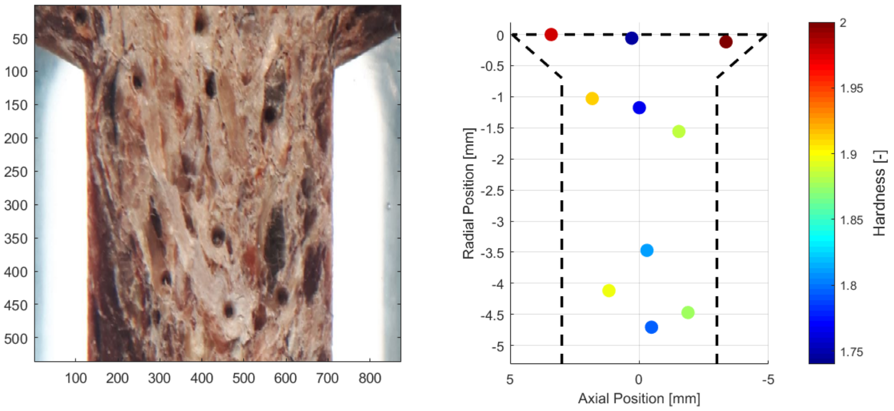

(e) Magnified picture (die no. 11). (f) Plotted hardness (die no. 11).

Figure 2.13: Photos of the magnified pellet and the mapped measuring locations and hardness.

The hardness of the three pellets in figure 2.13 can not be accounted for being statistical right, but though tendencies of the hardness for the three pellets will be drawn.

The hardness of the pellet produced in die no. 3, plotted in figure 2.13b, shows that the hardness is almost constant across the pellet, while it increases downward the axial direction in the inlet section.

The hardness of the pellet produced in die no. 6, plotted in figure 2.13d, shows that there is a tendency of the pelleting material to be harder near to the wall compared to the center. Generally for the pellet, the hardness is increasing in the axial direction.

The hardness of the pellet produced in die no. 11, plotted in figure 2.13f, shows that the hardness increases downward the pellet in the center axis. From the measurements of the three pellets, the pellet from die no. 11 has the largest radial differences in the hardness, where it is harder near the wall of the die.

CHAPTER 3

Numerical Modeling

The pelleting process and the physical processes that occur during pelleting of a material have previously been described on basis of many experimental tests, and there is a clear understanding on how different parameters affects the pelleting process. Even though there still are a lot of unknown variables, that has to be clarified to fully be able to describe the pelleting process. In the following chapter numerical models will be set up. The models are based on existing experimental test results and fundamental knowledge of the physical scenarios occurring in the pelleting process. The purpose of the models is to be able to simulate the pelleting load for various die designs, which can lead to improvements of the existing process. With the models it will be possible to simulate the processes occurring in the pellet channel, which from current knowledge has not been done so far. Starting with a simple model, the complexity will be increased as more physical processes will be implemented in the model structure.

3.1 Assumptions

In order to obtain a simulation of the pelleting process, a number of assumptions and limitations have been taken.

- The material properties for Poisson's ratio, ν, and Young modulus, E, are assumed to be constant during the entire process in the pellet channel.
- Wood is a orthotropic material, which means that the material properties are different in the axial, radial, and circumferential direction. The orientation, ϕ, of the wood fibers in the pellet channel will therefore affect the pelleting process. Since the packing and flow pattern of the fibers in the die are unknown, the orientation of the fibers are assumed to be constant through the entire pellet channel.

- The friction coefficient, μ, at the interface between the pelleting material and the wall of the pellet channel, is assumed to be constant for the entire pellet channel.
- Viscoplastic effects like material relaxation are neglected, and the radial stresses in the pellet channel will be based on the pelleting material obeying elastic behavior.
- The simulations will only encounter the active part of the pellet channel, which include the inlet (section 1) and the cylindrical part (section 2).
- The process is assumed to be in steady state.

3.2 1D Model

The first model that is set up, represents a single pellet channel, where the processes only occurs in one dimension (1D). The model is set up to simulate the pelleting process in the axial direction pelleting channel.

Two physical processes are encountered in the 1D model, in order to determine the energy requirement of the simulated dies. The energy requirement will be defined as a specific energy on mass basis, which defines the energy required to pelletise a certain amount of material in the chosen die, $w_s \left[\frac{J}{kg}\right]$. The two processes that will be encountered in the model are:

1. Friction between the pelleting material and the die wall.
2. Compression of the pelleting material.

3.2.1 Friction

The friction occurs at the interface between the pelleting material and the die wall. The pelleting material is forced trough the die, by the rolls acting a force in the axial direction of the die. A radial force in the pelleting material, acting normal to the die wall, appears as a consequence of the axial acting force. The radial force acting normal to the wall of the pellet channel implies a friction force acting opposite to the flow direction. The forces related to the friction in the pellet channel are shown in figure 3.1.

The friction between the wall of the pellet channel and the pelleting material is calculated by equation 3.1 where:

- F_μ is the friction force $[N]$
- F_{rad} is the radial force in the pelleting channel $[N]$

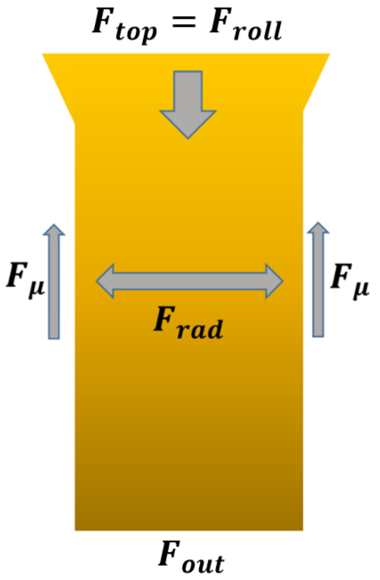

Figure 3.1: The forces acting in the pellet channel.

- μ is the friction coefficient $[-]$

$$F_\mu = F_{rad} \cdot \mu \tag{3.1}$$

The relation between the axial compression and the radial expansion is expressed by Poisson's ratio. A previous study by Holm et. al. has used Poisson's ratio, to define the friction in a cylindrical channel [22].

The effect of Poisson's ratio is illustrated in figure 3.2. Related to figure 3.2 is Poisson's ratio defined in equation 3.2 where:

- Axial strain: $\epsilon_{axi} = \frac{dx}{x}$ $[-]$
- Aadial strain: $\epsilon_{rad} = \frac{dr}{r_p}$ $[-]$
- ν_{RA} is Poisson's ratio for the strain in the radial (R) direction compared to the axial (A) direction $[-]$

$$\nu_{RA} = \frac{\epsilon_{rad}}{\epsilon_{axi}} = \frac{dr \cdot x}{dx \cdot r} \tag{3.2}$$

When pelleting material is compressed in the pellet channel, the radial expansion is restricted of the wall of the pellet channel. The radial expansion appear as a stress normal to the die wall, which causes a shear when the pelleting material is moved in the channel. The stress at the pellet channel walls, due to the effect of Poisson's ratio, is related to the strain of the pelleting material. Using Hookes law, which describes a proportional relation between stress and strain of material, the force normal to the pellet channel walls, F_{rad}, can be expressed by equation 3.3 where:

- E_ϕ is the young modulus of the pelleting material with the fiber orientation ϕ $[MPa]$

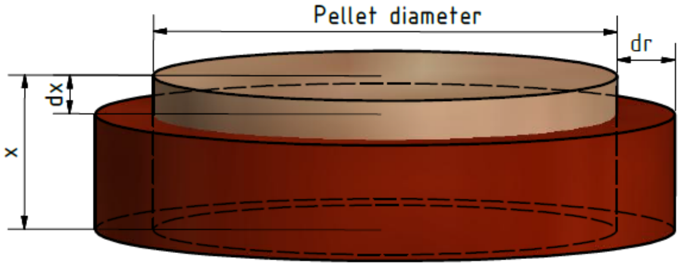

Figure 3.2: Compression of an element in the in the 1D model, causing a radial expansion.

- A_{rad} is the area of the interface between the wall of the pellet channel and the pelleting material, defined by $A_{rad} = r_p \cdot 2 \cdot \pi \cdot l$ where l is the length of the pellet channel $[m^2]$, and r_p is the radius of the pellet $[m]$

$$F_{rad} = E_\phi \cdot A_{rad} \cdot \frac{dr}{r_p} \tag{3.3}$$

The relation between the axial strain and the force applied in the axial direction, F_{top}, is expressed in equation 3.4 where:

- $E_{\phi\perp}$ is the young modulus of the pelleting material with a fiber orientation perpendicular to ϕ $[MPa]$
- A_{axi} is the cross-sectional area of the pellet channel, defined by $A_{axi} = r_p^2 \cdot \pi$ $[m^2]$

$$F_{top} = E_{\phi\perp} \cdot A_{axi} \cdot \frac{dx}{x} \tag{3.4}$$

Combining equation 3.3 and 3.4, an expression of force acting normal to the wall of the pellet channel (F_{rad}), can be obtained. The expression is shown in equation 3.5.

$$F_{rad} = \frac{E_\phi}{E_{\phi\perp}} \cdot \frac{2 \cdot l}{r} \cdot \nu_{RA} \cdot F_{top} \tag{3.5}$$

With the expression for the radial force, a force balance can be set up for the pellet channel. The force balance is based on figure 3.1, and shown in equation 3.6.

$$F_{top} - F_{out} - (F_{rad} \cdot \mu) = 0 \tag{3.6}$$

The purpose of the force balance is to determine the magnitude of F_{top}, that has to be applied, in order to push new pelleting material into the pellet channel. By rewriting equation 3.6, and substituting the expression for the friction force into the equation, an expression for F_{top} can be obtained. This expression is shown in equation 3.7:

$$F_{top} = \frac{F_{out}}{1 - \left(\frac{E_\phi}{E_{\phi\perp}} \cdot \frac{2 \cdot l}{r} \cdot \nu_{RA} \cdot \mu\right)} \tag{3.7}$$

The expression for F_{top} in equation 3.7, states that if the resisting force of an element is equal to zero, the applied force, F_{top} is also zero. This makes sense, because when no axial force is applied, no radial expansion will occur, and thereby all of the forces in the model will be equal to zero. In order to calculate the F_{top}-value, F_{out} at the outlet of the pellet channel has to be set to a value higher than zero.

The expression in equation 3.7 does not account any geometrical changes in the pellet channel shape. In order to account for the change of the shape in the inlet, the pellet channel will be discretized into a number of elements, which sizes corresponds to the position in the pellet channel.

Frictional Work

To determine the specific energy requirement for the frictional work in the pellet channel, the power that is dissipated due to friction is calculated using equation 3.8 where:

- $\dot{W}_\mu$ is the power dissipated caused by friction $[W]$
- v_p is the velocity of the pelleting material in the pellet channel $\left[\frac{m}{s}\right]$

$$\dot{W}_\mu = F_\mu \cdot v_p \tag{3.8}$$

By applying conservation of mass, the velocity of the pelleting material in the pellet channel is calculated by equation 3.9 where:

- $\dot{m}$ is the mass flow of pelleting material $\left[\frac{kg}{s}\right]$
- ρ_p is the density of the pelleting material $\left[\frac{kg}{m^3}\right]$

$$v_p = \frac{\dot{m}}{\rho_p \cdot A_{axi}} \tag{3.9}$$

The density of the pelleting material in the pellet channel is expressed by the empirical correlation between pressure and density, which was found from the experimental tests. The specific energy requirement for the frictional work is calculated by equation 3.10 where:

- $w_{s\mu}$ is the specific energy requirement for the frictional work $\left[\frac{J}{kg}\right]$

$$w_{s\mu} = \frac{\dot{W}_\mu}{\dot{m}} \tag{3.10}$$

Pressure

The density of the pelleting material is linked to its pressure. As described previously, the pressure of the pelleting material is defined as the average of the stresses acting normal to pelleting material. A normal stress is defined as the force acting normal to the volume, divided by the area on where the force acts. In 3D cartesian coordinates the pressure of a box is defined by equation 3.11, where:

- P is the pressure $[Pa]$
- σ_x, σ_y and σ_z are the normal stresses acting on the volume $[Pa]$

$$P = \frac{1}{3} \cdot (\sigma_x + \sigma_y + \sigma_z) \tag{3.11}$$

For a cylindrical volume, two normal stresses are acting, σ_{axi} and σ_{rad}. In order to obtain a definition for the pressure of a cylindrical shape, equation 3.12 is used.

$$P = \frac{1}{3} \cdot (\sigma_{axi} + 2 \cdot \sigma_{rad}) \tag{3.12}$$

3.2.2 Compression

The second of the two energy requiring processes that are encountered in the model, is the compression of the pelleting material. As previously described and shown in figure 1.16 does multiple processes occur during compression of a biomass material. The plastic deformation of the wood fibers are caused by a compressional work. The compression causes a rise in density. Due to the high complexity of the compression process, the calculation of the compressional work will be based on the empirical correlation found between pressure and density in the experimental test.

Compressional Work

Using the empirical function for pressure as a function of the specific volume, the amount of specific work in $\left[\frac{J}{kg}\right]$ used for compression can be calculated. Figure 3.3 illustrates the amount of specific compressional work used for compression, which is represented by the marked area below the function curve. The vertical dotted line, $V_{s\ min}$, in figure 3.3, specifies the lower limit for the specific volume obtained by compression.

Calculation of the specific compressional work can be done by using equation 3.13 where:

- w_{sc} is the specific compressional work $\left[\frac{J}{kg}\right]$
- $V_{s.1}$ and $V_{s.2}$ are the change in the specific volume due to compression $\left[\frac{m^3}{kg}\right]$
- P is the pressure $[Pa]$

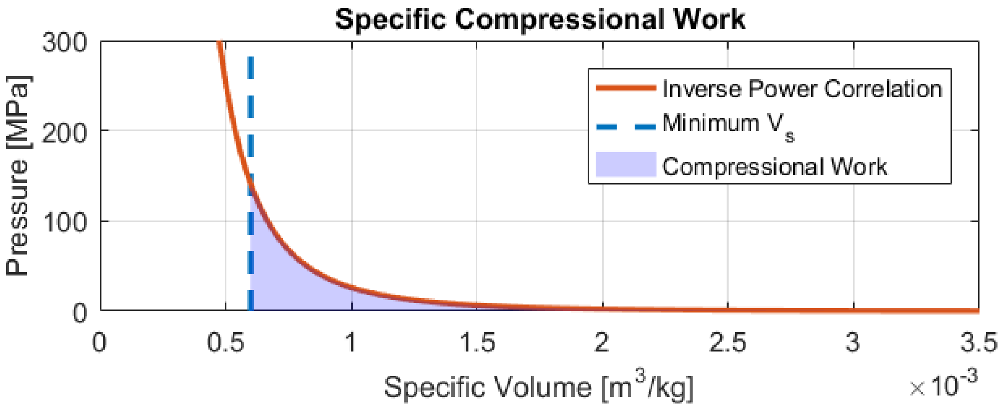

Figure 3.3: Compressional work exerted on the pelleting material as a function of the pressure.

$$w_{sc} = \int_{V_{s.1}}^{V_{s.2}} P \, dV_s \tag{3.13}$$

To determine the amount of compressional power used in the pelleting channel, the specific compressional work is multiplied by the mass flow of pelleting material. The compressional power is defined in equation 3.14, where:

- $\dot{W}_c$ is the power used for compression in the pellet channel $\left[\frac{J}{s}\right]$

$$\dot{W}_c = w_{sc} \cdot \dot{m} \tag{3.14}$$

3.2.3 Discretization of the 1D Model

In order to simulate the compression and the forces acting in a pelleting channel, the channel is discretized into N number of elements, where a force balance is set up for each element. Applying the expressions for compressional- and frictional work, the energy comsumption in each element in the pellet channel can be determined.

Each element represents a disk of the pellet channel. Figure 3.4 illustrates the discretization of the pellet channel. Figure 3.4a shows the original pellet channel design compared to the discretized design, and figure 3.4b shows the dimensions of the pellet channel. As figure 3.4a illustrates, the dicretization of the pellet channel causes a simplification of the shape. The simplification will cause inaccuracies of the modeled die design compared to the original design. By increasing the number of elements in the model, and thereby the resolution, these inaccuracies will be reduced. The 1D model is set up, such that the dimensions of the pellet channel can be varied and evaluated easily.

The axial size of the elements in the model is constant, and it is determined by equation 3.15 where:

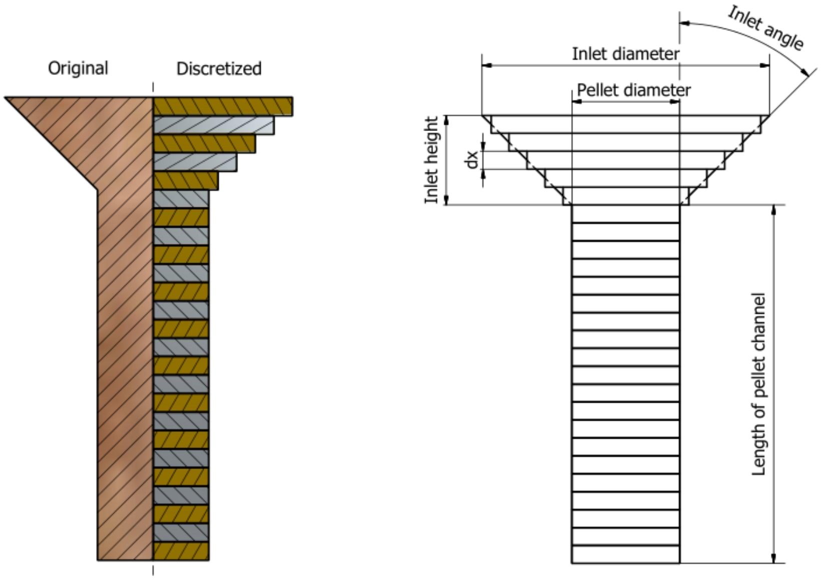

(a) Original and discretized pellet shape.

(b) Dimensions of the pellet channel.

Figure 3.4: Discretization of the pellet channel in the 1D model.

- N is the number of elements in the model $[-]$
- dx is the axial size of each element $[m]$
- l is the axial length of the pelleting channel $[m]$

$$dx = \frac{l}{N} \tag{3.15}$$

The model is divided into two sections; inlet (section 1) and pellet channel (section 2). In the conical inlet the radial size of the elements are dependent of the position in the inlet, while it is constant in the cylindrical pellet channel. The number of elements in the inlet are dependent of the model resolution and the chamfer depth, z. The number of elements in the inlet and the pellet channel are described in equation 3.16 where:

- N_{inlet} is the number of elements in the inlet $[-]$
- $N_{channel}$ is the number of elements in the pellet channel $[-]$

$$N_{inlet} = \frac{z}{dx} \tag{3.16a}$$

$$N_{channel} = N - N_{inlet} \tag{3.16b}$$

To ensure that the number of elements in the two sections are integers, the values of N_{inlet} and $N_{channel}$ are rounded.

The radial size of the elements in the cylindrical press channel (section 2) corresponds to the diameter of the pellet channel, while the radial size of the elements in the inlet (section 1) is calculated by equation 3.17 where:

- $r(n)$ is the radius of the cylindrical element n $[m]$
- n is the element number $[-]$
- α is the inlet angle of the pellet channel $[^o]$
- r_p is the radius of the press channel $[m]$

$$r(n = 1 : N_{inlet}) = r_p + tan(\alpha) \cdot \left((N_{inlet} - (n-1)) \cdot dx - \frac{1}{2} \cdot dx \right) \tag{3.17}$$

The axial surface area of the elements is the flat area between the elements. This area varies for the elements in the inlet, dependent of the axial position, while it is constant for the elements in the press channel. The axial surface areas are determined by equation 3.18 where:

- $A_{axi}(n)$ is the axial surface area of the element n $[m^2]$

$$A_{axi}(n) = \pi \cdot r(n)^2 \tag{3.18}$$

The radial surface area of the elements, is the curved contact area between the wall of the pelleting channel and the element. The radial surface areas is determined by equation 3.19 where:

- $A_{rad}(n)$ is the radial surface area of the element n $[m^2]$

$$A_{rad}(n) = \pi \cdot r(n) \cdot 2 \cdot dx \tag{3.19}$$

3.2.4 Solving the 1D Model

In order to obtain a simulation of the pellet channel, a free body diagram is set up for each element in the 1D model. A force balance for an element is illustrated in figure 3.5. It shows an axis symmetric element and the forces acting on it, where:

- F_{top} is the force applied from element $n-1$ $[N]$
- F_{rad} is the radial force that acts normal to the die wall $[N]$
- F_{res} is the resisting force, that corresponds to the force required to push the elements below $[N]$
- F_{μ} is the friction force between the wall of the pellet channel and the pelleting material $[N]$

Based on the free body diagram in figure 3.5, F_{res} and F_{μ} works in the same direction, and acts as the resistance in the pellet channel. These are oriented in the opposite direction of F_{top}.

- For element $n = 1$, F_{top} is equal the load of the pellet channel
- For element $n = N$, F_{res} is equal to zero

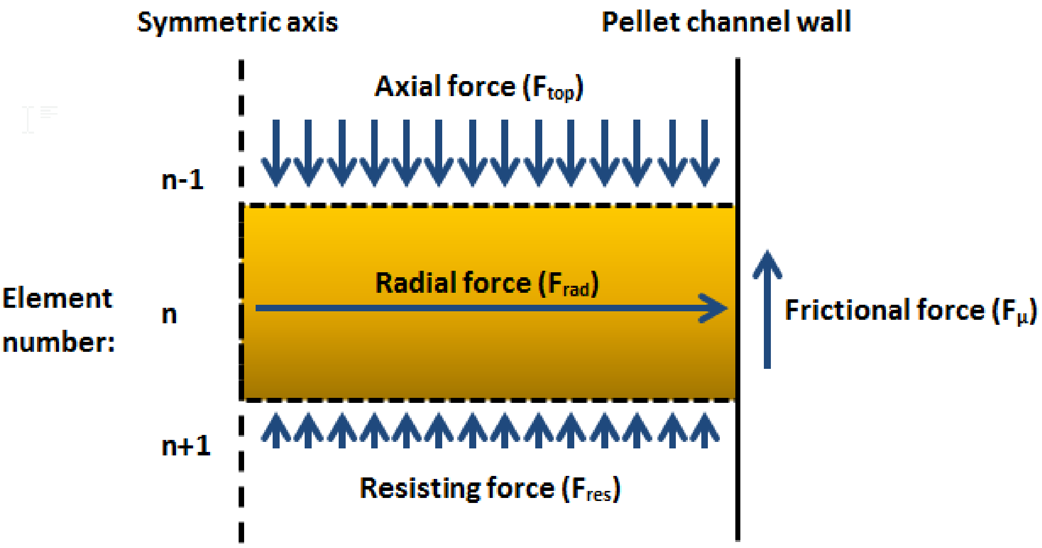

Figure 3.5: Force balance for an element in the 1D model.

With F_{res} set as a known boundary condition at the outlet element $(n = N)$, the magnitude of F_{top} for this element can be calculated with the expression found in equation 3.7, where $l = dx$. To calculate F_{top} for the next element $(n = N - 1)$, F_{res} is set equal to the value of F_{top}, from the element below. This relation is shown in equation 3.20.

$$F_{res}(n-1) = F_{top}(n) \tag{3.20}$$

Algorithm for Energy Consumption

After solving the force balances of the elements, the energy requirement for the pelleting process through the channel can be solved. The algorithm for this calculation is illustrated as a flow chart in figure 3.6.

Pressure in the Elements

The pressure of the elements in the 1D model is calculated from the definition stated in equation 3.12, where:

- σ_{axi} is the average of the normal stresses acting in the axial direction of the element, divided by the axial cross sectional area of the element, which is shown in equation 3.21

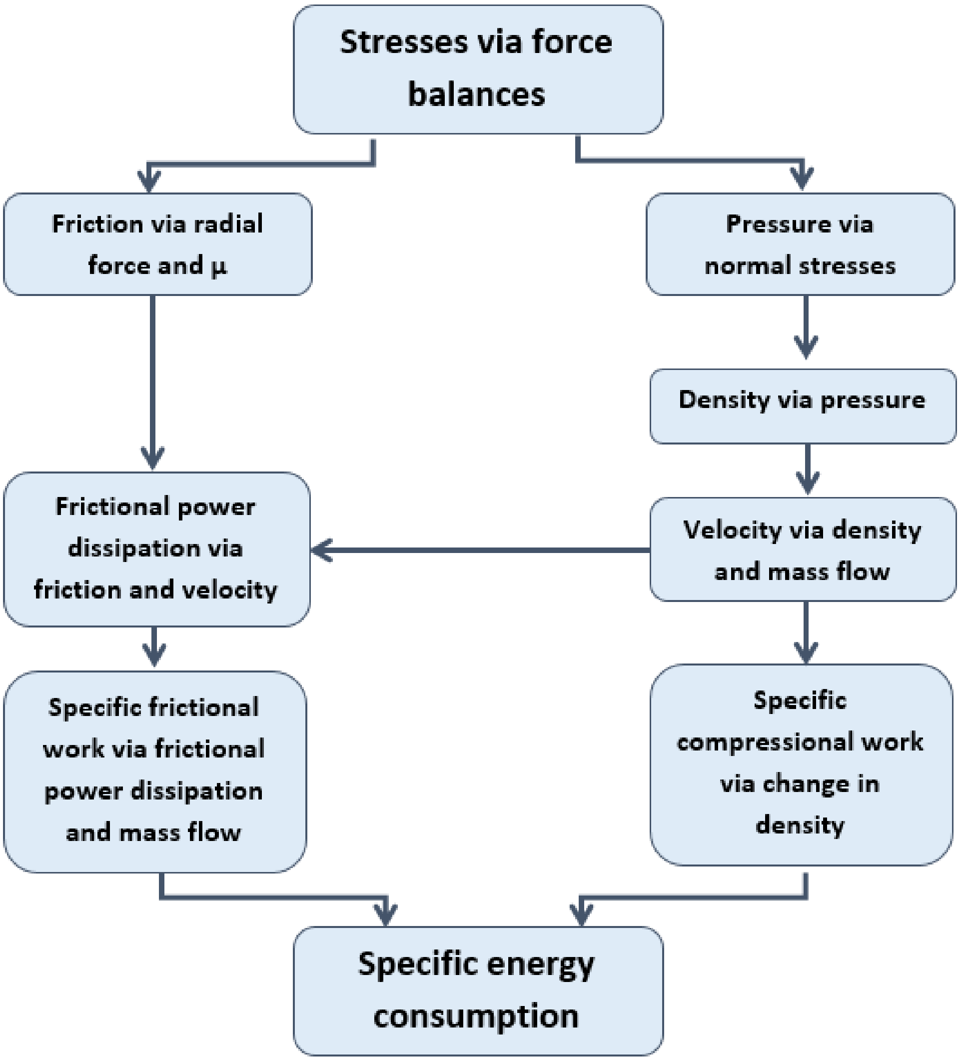

Figure 3.6: The algorithm set up for the calculation of the specific energy requirement for the processes in the pellet channel.

- σ_{rad} is the normal stress acting in the radial direction of the element, divided by the radial surface area of the element, which is shown in equation 3.22

$$\sigma_{axi} = \frac{\frac{F_{top}+F_{res}}{2}}{A_{axi}} \tag{3.21}$$

$$\sigma_{rad} = \frac{F_{rad}}{A_{rad}} \tag{3.22}$$

3.2.5 Grid Independence

As described previously, the simulation of the 1D model is based on a number of even-spaced elements in the axial direction of the pellet channel. The number of elements in the model affects the final simulation result. A low number of elements causes a poor resolution of the original pellet channel design, and the simulation results will be dependent of the number of elements. To obtain independence in the simulation with respect to the number of elements, an independence study of the model resolution is conducted. The 1D model is run with 100 elements, and thereafter the number is increased by another 100 elements until a independence in the simulation result is reached. To determine the independence of the model, a residual is calculated between each model resolution. The residual is defined as the change in percentage between two resolutions, and is shown in equation 3.23 where:

- $\phi(n)$ is the simulation value ϕ at resolution n $[-]$
- *Scaled Residual* is the change in simulation result between two model resolutions

$$Scaled\,Residual = \frac{\phi(n) - \phi(n-1)}{\phi(n-1)} \cdot 100 \tag{3.23}$$

The value that is evaluated for the model resolutions, is set as the required roll force ($(F_{top}(n = 1))$).

Properties for pine is used for the model resolution study, which is found in the Wood Handbook[23]:

- $\frac{E_\phi}{E_{\phi\perp}} = 20.7$ (fibers oriented perpendicular to the axial direction of the pellet channel and normal to the wall of the pellet channel)
- $\nu_{RA} = 0.021$
- $\mu = 0.4$
- $\dot{m} = 0.374\frac{g}{s} \approx 5.4\frac{ton}{h}$ for a ring die with 4000 pellet channels

The following dimensions are used for the pellet channel in the model resolution study:

- Active press length: $l = 50\,mm$
- Diameter: $d_p = 6\,mm$
- Inlet angle: $\alpha = 30^o$
- Chamfer depth: $z = 2\,mm$

The properties and dimensions used for the resolution study, have been selected in order to generate a simulation with realistic inputs.

Figure 3.7 shows the result of the model resolution study. Figure 3.7a shows the required roll force for the simulated model resolutions. It shows that the roll force is stable at approximate 4000 elements. Figure 3.7b shows the corresponding change in roll force when the element count is increased. At 4000 elements, the change in roll force is less than 0.01%, which is assumed to be good enough. In a matter of missing computational power, the element count can be lowered, and still be able to obtain good simulation results.

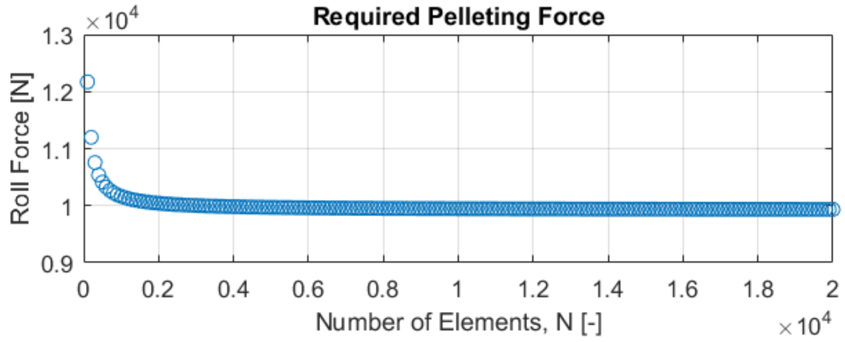

(a) Required roll force for different model resolutions.

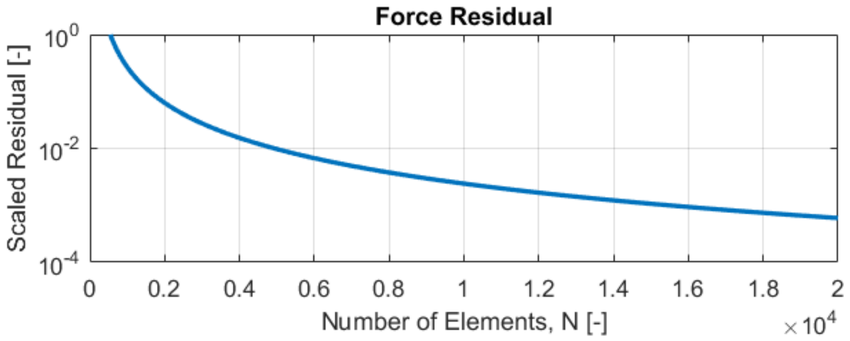

(b) The scaled residual at increasing element counts.

Figure 3.7: Independence study of the model resolution.

3.3 1D Model Simulations

In order to show how the 1D model is performing, simulation results of the three dies used in the hardness experiment will be presented, likewise how the specific energy requirement changes with inlet angel and chamfer depth for multiple die designs.

Model Input

In order to validate the 1D model, the model has to be run with properties similar to the pelleting material used for the experimental tests. The exact properties for the testing material has not been determined experimentally, therefore values from similar wood types are found in the literature [23]:

- $\frac{E_\phi}{E_{\phi\perp}} = 20.7$ (fibers oriented perpendicular to the axial direction of the pellet channel and normal to the wall of the pellet channel)

- $\nu_{RA} = 0.025$

- $\mu = 0.4$

- $\dot{m} = 0.374\frac{g}{s} \approx 5.4\frac{ton}{h}$ for a ring die with 4000 pellet channels

The friction coefficient, μ, is set for 0.4, because this value corresponds to a dry pelleting material on a smooth surface. Since the $MC \approx 8\%$ of the pelleting material used for experiments, it is assumed as being dry. Higher values of MC results in higher friction coefficients (μ = 0.4-0.8 [23]). The fact that the exact material properties are unknown, can cause some deviation in the simulation result compared to the experimental results. The total length of the pellet channel is set to 50 mm, and the pellet diameter is 6 mm, which corresponds to the dimensions of the dies used in the single pellet experimental [1].

3.3.1 Single Die Simulation

The energy consumption in the pellet channel has been divided into two subsections; friction and compression. To show where the energy is consumed in the pellet channel, a simulation of die no. 11 ($\alpha = 70^o$, $z = 0.7mm$) is conducted.

Figure 3.8 shows how the required force and the pressure and density varies in the pellet channel. The force curve in figure 3.8a is the F_{top}-values plotted for each element in the model. The orange curve illustrates the shape of the die wall.

In figure 3.8b the pressure and density of the elements are plotted. It is seen that the very flat inlet causes the pressure to increase in the inlet, which is mainly caused by the decreasing cross sectional area of the elements. Likewise the pressure, the density also increases in the inlet, until it reaches its final value right at the transition between the inlet and the cylindrical channel.

Figure 3.9 shows where in the pellet channel the energy is consumed. Figure 3.9a shows the frictional and compressional energy, and figure 3.9b shows the total accumulated energy in the pellet channel. It is seen that there is a offset of the accumulated energy at the start of pellet channel in figure 3.9b. This offset is caused by the amount of energy used for compressing the pelleting material to the density of the first element. In a pellet mill, this will be equal to the amount of energy used for compression before the pelleting material enters the pellet channel. Figure 3.9b shows that almost $\frac{5}{6}$ of the total energy is consumed in the first 20% of the pellet channel.

Contour plots of the pressure for the three die designs, which were used for the pellets in the hardness experiment, are shown in figure 3.10. Common for the

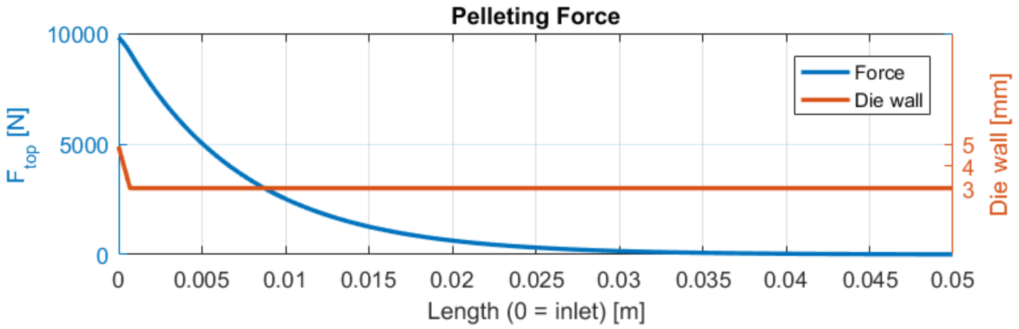

(a) F_{top}-force of the elements, and the shape of the die wall.

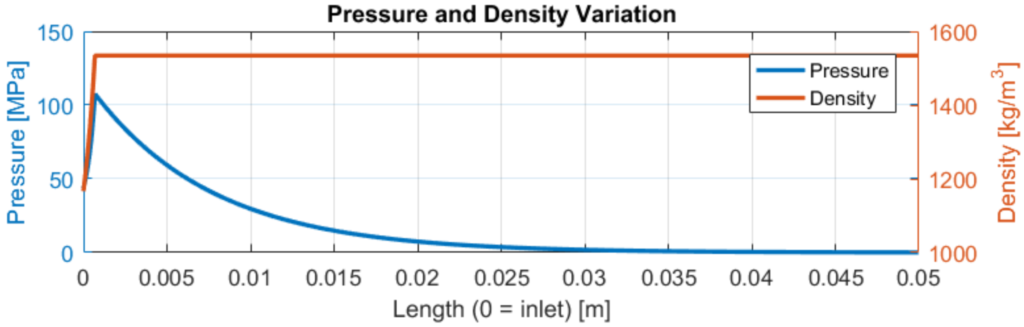

(b) Values for pressure and density in the pellet channel.

Figure 3.8: Simulation of die no. 11.

simulation of the three dies, is that the pressure peak is located at the interface between the inlet section and the cylindrical channel. The fact that the pressure peak is found at the interface between the inlet section and the cylindrical channel, can also explain why the wear in the pellet channel is observed in the inlet of the die.

Generally for the three dies are that:

- The maximum pressure in the dies decreases when the inlet depth increases
- The pressure gradients in the inlet increases, when the inlet angle increases

The highest pressure is seen in figure 3.10c for die no. 11.

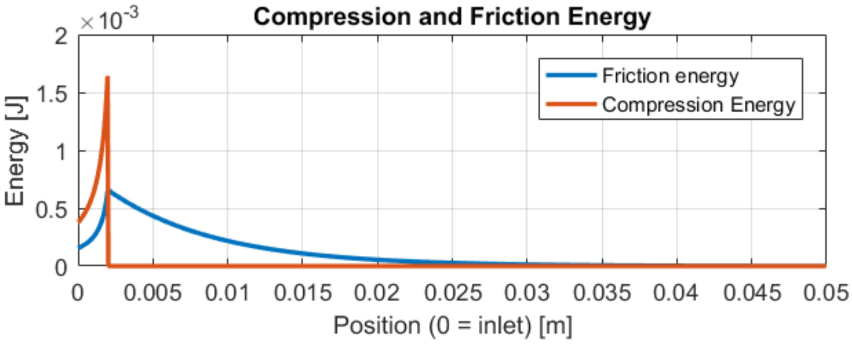

(a) Frictional- and compressional energy consumption in the pellet channel.

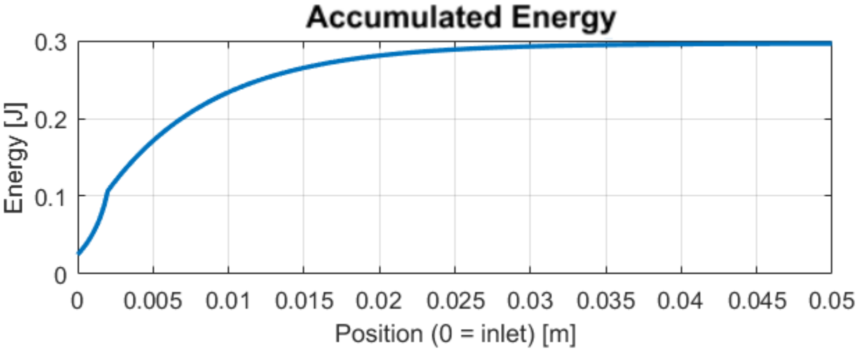

(b) Accumulated total energy consumption in the pellet channel.

Figure 3.9: Energy consumed in the pelleting channel.

3.3.2 Global Simulation Result

To test how the specific energy requirement changes with inlet angle and chamfer depth, the 1D model is run with a combination of the following values of inlet angle and chamfer depth:

- $\alpha[^o] = \begin{bmatrix} 0 & 10 & 20 & 30 & 40 & 50 & 60 & 70 & 80 & 90 \end{bmatrix}$
- $z[mm] = \begin{bmatrix} 0.0 & 0.5 & 1.0 & 1.5 & 2.0 & 2.5 & 3.0 & 3.5 & 4.0 & 4.5 \\ 5.0 \end{bmatrix}$

The 110 die designs are plotted, and a surface is generated with linear interpolation between the data points. The specific energy requirement for friction, compression and the sum of these are shown in figure 3.11 where:

- Figure 3.11a shows the specific energy used for friction
- Figure 3.11b shows the specific energy used for compression
- Figure 3.11c shows the total specific energy used in the dies

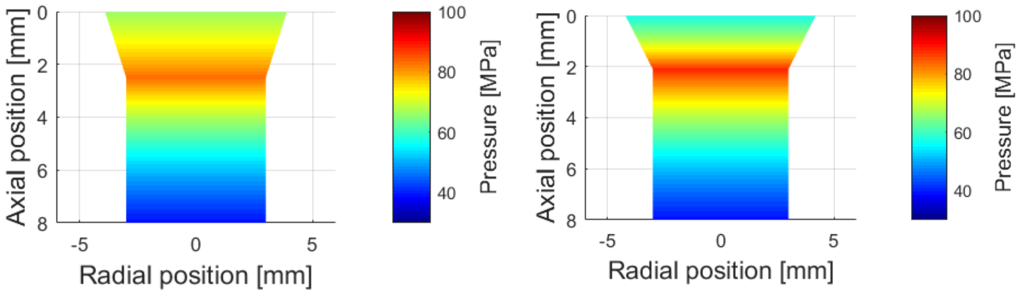

(a) Die no. 3.

(b) Die no. 6.

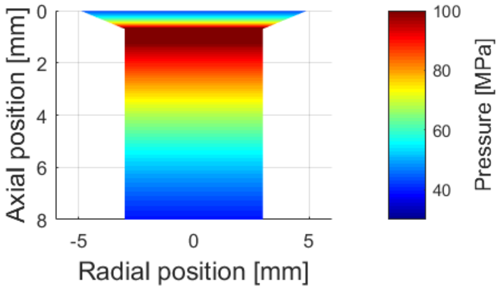

(c) Die no. 11.

Figure 3.10: Pressure in the upper part of the pellet channel for the three die designs.

Figure 3.11 shows that the major amount of energy in the pellet channel is dissipated by frictional work, and that the energy used for compression is $\approx \frac{1}{7} \sim \frac{1}{8}$ of the friction energy. The contours of the frictional- and compression work in figure 3.11a and 3.11b are similar. This is caused by the compressional work being directly linked to the pressure, which again is directly linked to the forces in the pellet channel, and thereby the frictional force. It is seen in figure 3.11c that the highest energy requirement is found in the combinations of $\alpha = 0^o$ and $z = 0\,mm$, which all results in the same energy requirement. This makes sense, since all of these combinations corresponds to a cylindrical channel, without an inlet section. Therefore the energy requirement of these combinations also have to be similar.

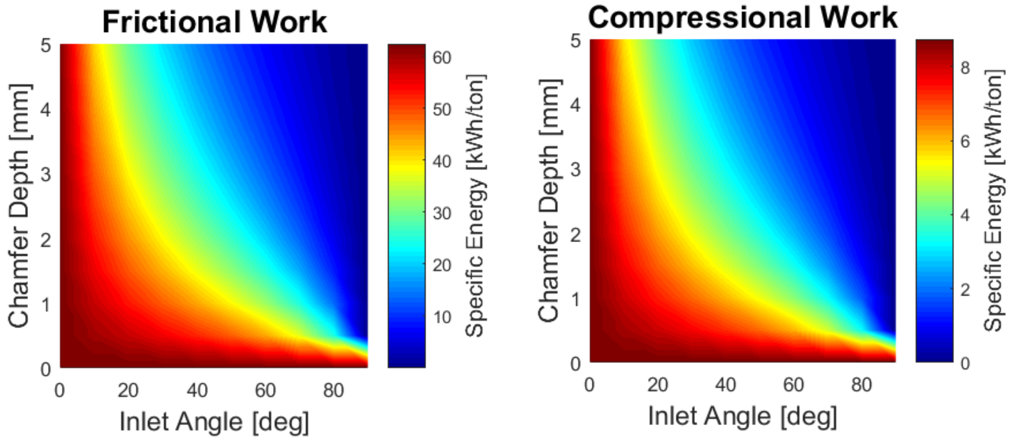

(a) Specific frictional work. (b) Specific compressional work.

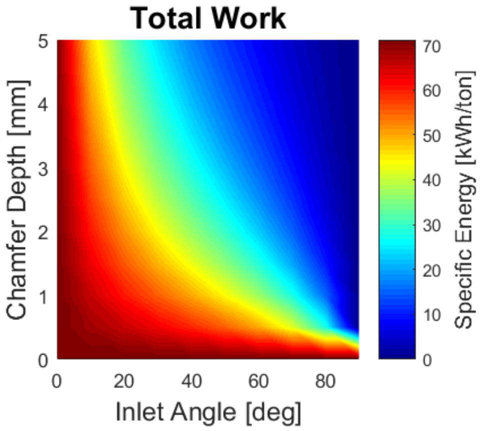

(c) Total specific work.

Figure 3.11: Comparison of energy requirement for dies with different inlet angels and chamfer depths.

3.4 Validation of the 1D Model

The 1D model will be validated on basis of the required load for the dies. The simulation results will be compared to the experimental results from the tests conducted in the 9th semester [1]. A plot which shows the pelleting load as a function of the chamfer depth and the inlet angle will be generated for the 1D model and compared to the experimental result.

Validation of the 1D Pelleting Load

In figure 3.12 are the measured pelleting loads from the experiment and the simulated loads from the 1D model shown. The black dots represents the dies. The surface is generated by a linear interpolation between the data of dies.

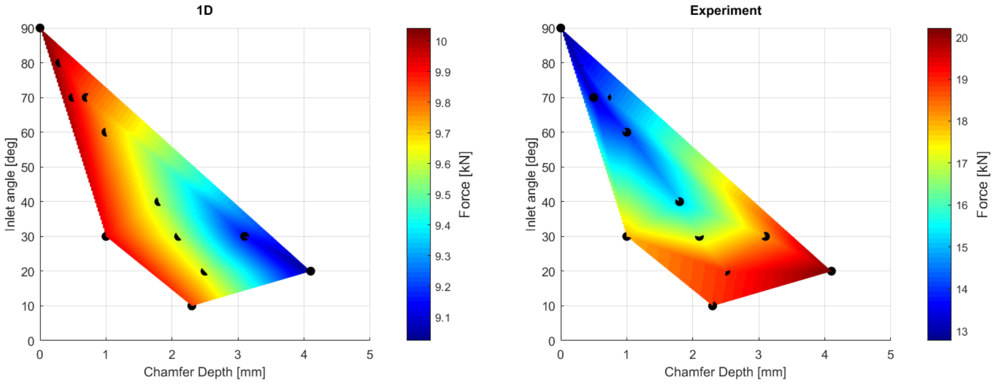

(a) 1D simulation.

(b) Experiment.

Figure 3.12: Pelleting loads.

Figure 3.12 shows that there is an offset between the experimental and simulated result. Based on the die without any inlet ($z = 0$), the offset is approximate $2\ kN$. Assuming that the inlet causes some radial effects, which affects the pelleting load, the die without any inlet should be the only one, that can be described by the 1D model. The offset between the model simulation and the experiment can be caused by the fact, that the 1D model only accounts for the pellet channel, and not includes any effects above the inlet, which is included in the experiments. Additionally the uncertainties of the experiments should be taken to account.

The simulation results in figure 3.12a, shows that the pelleting load reduces when the chamfer depth is increased, and the inlet angle is decreased. The opposite tendencies are observed for the experimental results in figure 3.12b, which shows that the specific energy increases when the chamfer depth is increased, and the inlet angle is decreased.

The conclusion of the validation is the 1D model can give a good estimation of the pelleting load for a pellet channel without any inlet. To account for radial changes in the pellet channel, a 2D axis symmetric model will be set up.

3.5 2D Model

To account for process variations in the radial direction of the pellet channel, a 2D axis-symmetric model is set up.

Figure 3.13 shows the forces that acts on the 2D model, where τ is the shear stress. Instead of setting an outlet force acting in the negative y-direction, at the outlet of the pellet channel, a pressure, P_{out}, is set. The set up of the model assumes that the shear stress in the radial direction of the pellet channel, varies linearly between the wall and the center of the pellet channel. Equation 3.24 defines the shear stress in the pellet channel as a function of the radial position, r, where:

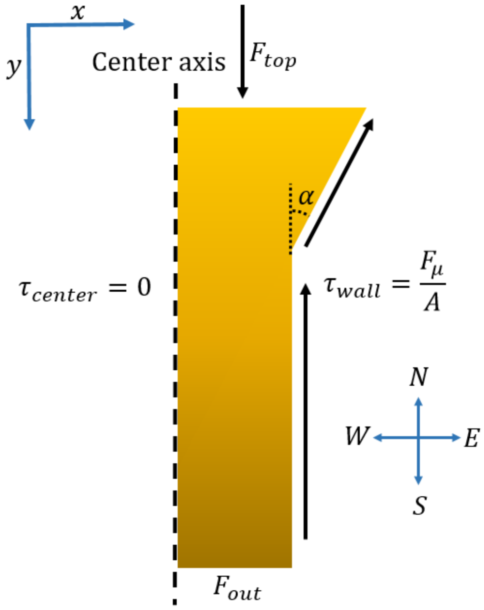

Figure 3.13: Outer forces acting in the 2D model.

- A is the area of the interface between the pelleting material and the wall of the die, where the friction force, F_μ, acts $[m^2]$

$$\tau = \frac{\tau_{wall}}{r_p} \cdot r = \frac{F_\mu}{A \cdot r_p} \cdot r \tag{3.24}$$

The friction force, F_μ, is defined in the same way as for the 1D model (equation 3.1). In the 2D model, the forces are set with a x- and a y-component. The orientation of x and y is defined in figure 3.13. The boundaries in the model will be denoted as north, south, east and west. The orientation of these are also shown in figure 3.13.

3.6 Discretization of the 2D Model

The 2D axis symmetric model will be discretized into two types of elements, which are shown in figure 3.14.

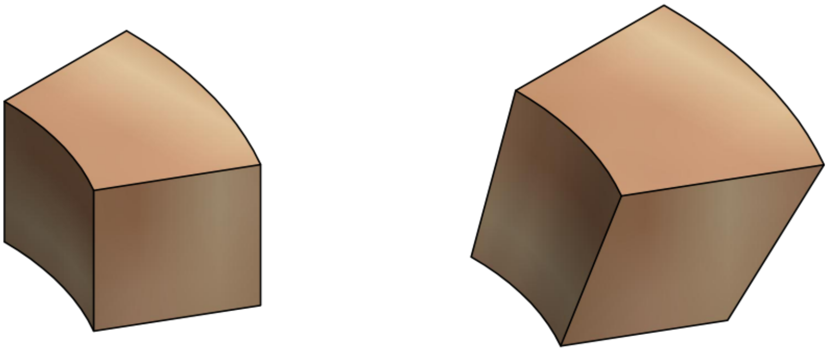

(a) Regular. (b) Skew.

Figure 3.14: The two types of elements used in the 2D model.

The regular element in figure 3.14a are used in the cylindrical part of the pellet channel, while the skew element in figure 3.14b are used in the conical inlet. The size of the elements depends of the size of the pellet channel, and the resolution of the model. The model discretization is defined by the dimensions of the pellet channel and the selected numbers of axial (N) and radial (M) elements.

Figure 3.15 illustrates discretizations of a 6 mm pellet channel with $\alpha = 30^o$ and $z = 5mm$, where figure 3.15a, 3.15b, 3.15c and 3.15d are different resolutions of the discretization.

Besides the length and pellet diameter, the discretization of the 2D model is defined by an inlet angle and a chamfer depth. The axial height of the elements (dx) is constant, and defined similar to the height used in the 1D model (see equation 3.15). The width of the elements in the radial direction (dy), is constant in the cylindrical part of the channel, and varies in the inlet. In the cylindrical channel, the width is defined by equation 3.25, where:

- r_p is the radius of the pellet channel $[m]$
- M is the number of elements in the radial direction of the die $[-]$

$$dy = \frac{r_p}{M} \tag{3.25}$$

To set up the discretization, two parameters are calculated, which are the number of axial elements in the inlet (N_{inlet}) and number of axial elements in the channel ($N_{channel}$). Both of these have to be integers, which can lead to deviations between the input design of the pellet channel and the discretized design. They are defined

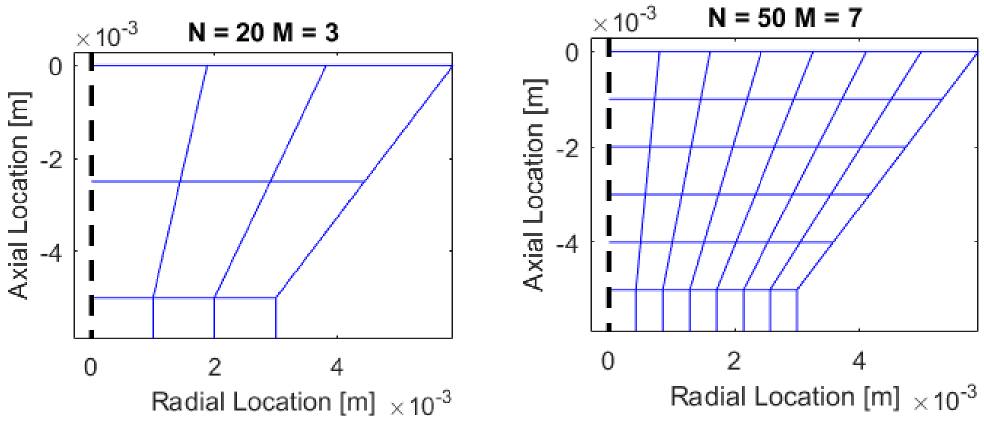

(a) $N = 20$, $M = 5$ (b) $N = 50$, $M = 7$

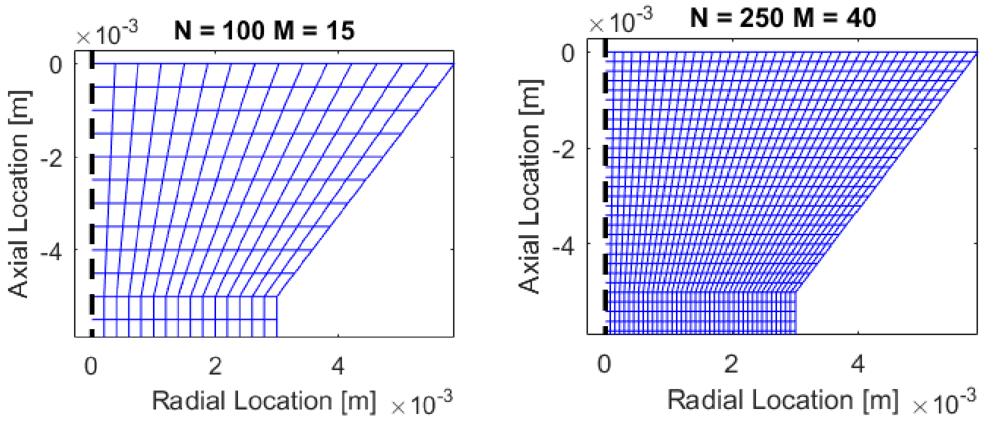

(c) $N = 100$, $M = 15$ (d) $N = 250$, $M = 40$

Figure 3.15: Graphic representation of four grid resolutions.

similar to the ones used in the 1D model (equation 3.16). Figure 3.16 shows how the resolution of the discretization affects the simulated die dimensions, compared to the actual die dimensions. Figure 3.16a shows that low resolutions in the axial direction can cause major differences in the actual die design and the discretized design used in the simulation. Figure 3.16a shows a higher resolution where the actual die design are similar to the discretized design.

3.6.1 Area and Volume

The surface areas of the elements in the model is defined by two shapes, the curved area which is parallel to the wall of the pellet channel, and the ring shaped area which is parallel to the in- and outlet of the channel. The dimensions used for the calculations are shown in figure 3.17.

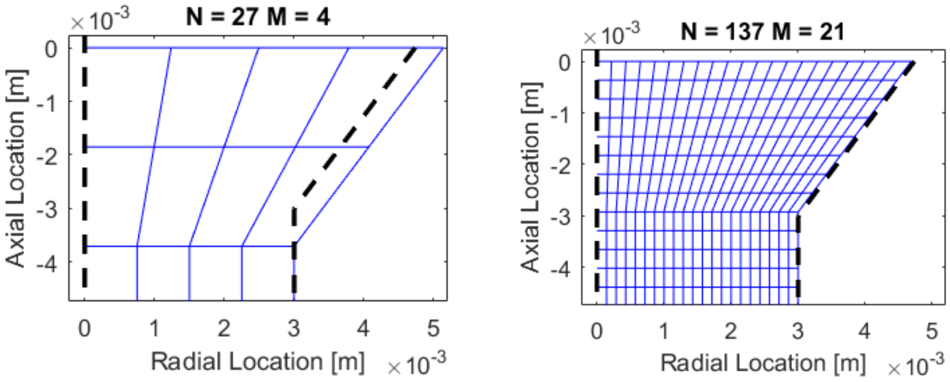

(a) Low model resolution.

(b) High model resolution.

Figure 3.16: Illustration of the actual die design (dotted black line) and the discretized design used in the simulation (blue lines).

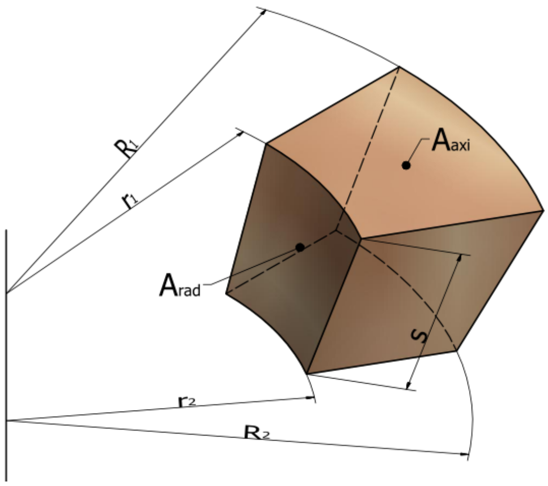

Figure 3.17: Dimensions used for the area calculations.

The areas facing parallel to the in- and outlet (north and south areas) are defined by equation 3.26, where:

- A_{axi} is the area $[m^2]$
- R_1 is the outer radius of the element $[m]$
- r_1 is the inner radius of the element $[m]$

$$A_{axi} = \pi \cdot ({R_1}^2 - {r_1}^2) \tag{3.26}$$

The areas facing normal to the wall of the pellet channel (east and west areas) are defined in equation 3.27, where:

- A_{rad} is the area $[m^2]$
- s is the length of the skew side on the element $[m]$
- r_1 and r_2 are the upper and lower radius $[m]$

$$A_{rad} = \pi \cdot s \cdot (r_1 + r_2) \tag{3.27}$$

For the regular elements in the cylindrical channel, r_1 and r_2 is equal, and s is equal to dx.

The volume of the elements are defined in equation 3.28, where:

- V is the volume of the element $[m^3]$

$$V = \frac{1}{3} \cdot dx \cdot \pi \cdot \big(({R_1}^2 + {R_2}^2 + R_1 \cdot R_2) - ({r_1}^2 + {r_2}^2 + r_1 \cdot r_2)\big) \tag{3.28}$$

3.6.2 Force Balances of the Elements without Poisson's Ratio

In this section, the force balances of the elements in the 2D model will be set up without the effect of Poisson's ratio. The elements will be denoted with two subscripts; (n, m), where n is the row number (y-direction) and m is the column number (x-direction). Element $(1, 1)$ is the inlet row at the symmetric axis. The force balances are set up in the same way for both the regular and the skew elements in the model.

Wall Element ($m = M$)

Figure 3.18 illustrates a force balance for the skew boundary element ($n = N_{inlet}$, $m = M$). The forces that acts on the boundaries of the element are marked by arrows that are not dotted. The forces inside the element, marked by the dotted arrows, have to equalize to the outer forces, such that the sum of forces, acting on the element equals zero.

The two shear forces, $\vec{F}_{\tau(M)}$ and $\vec{F}_{\tau(M-1)}$, are both dependent of the force applied from the top of the element, $\vec{F}_N$. The first step in order to solve the force balance, is to determine the force that is applied to the die wall, by $\vec{F}_N$. $\vec{F}_N$ has two components (x and y), which are illustrated in figure 3.19a. Each of the two components contribute to a force, $\vec{F}_{N,wall}$, that acts normal to the die wall.

Using the angle of the die wall, α_M, the force $\vec{F}_{N,wall}$ can be calculated from the sub-components of the $\vec{F}_N$ force, which are illustrated in figure 3.19b. The sum of the two sub-components, that acts normal to the die wall, equals $\vec{F}_{N,wall}$, which is stated in equation 3.29

$$\vec{F}_{N,wall} = \left(\underbrace{F_{N,x} \cdot cos(\alpha_M)}_{\text{Contribution from } \vec{F}_N,\, x} + \underbrace{F_{N,y} \cdot sin(\alpha_M)}_{\text{Contribution from } \vec{F}_N,\, y} \right) \cdot \begin{pmatrix} cos(\alpha_M) \\ sin(\alpha_M) \end{pmatrix} \tag{3.29}$$

With the expression for $\vec{F}_{N,wall}$, the frictional force is determined. The frictional force acts perpendicular to $\vec{F}_{wall}$, and is stated in equation 3.30.

$$\vec{F}_\mu = -\hat{\vec{F}}_{N,wall} \cdot \mu \tag{3.30}$$

Converting the friction force to a shear stress, and using the shear stress formulation stated in equation 3.24, the shear stress at the east boundary for the element in figure 3.18 can be calculated. This is shown in equation 3.31, where:

- A_W is the west face area of the element $[m^2]$
- R_1 and r_1 are the inner and outer radius of the element $[m^2]$

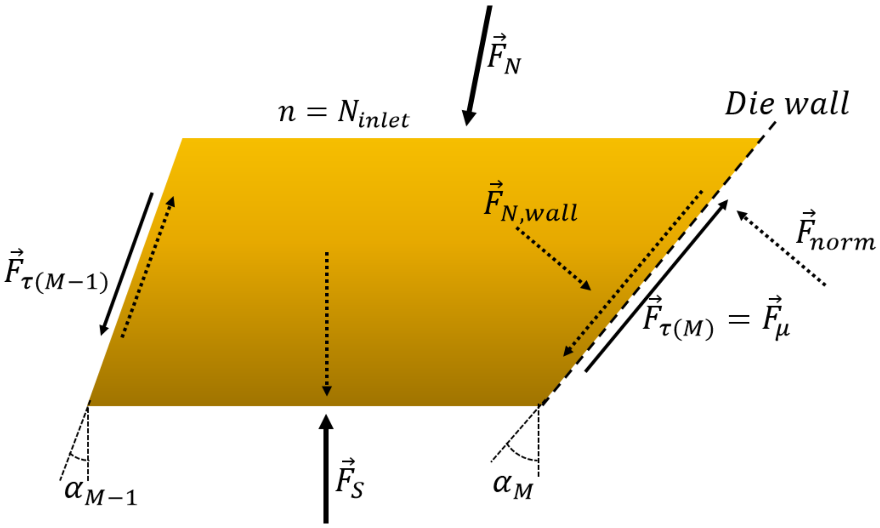

Figure 3.18: Force balance for the element ($n = N_{inlet}$, $m = M$).

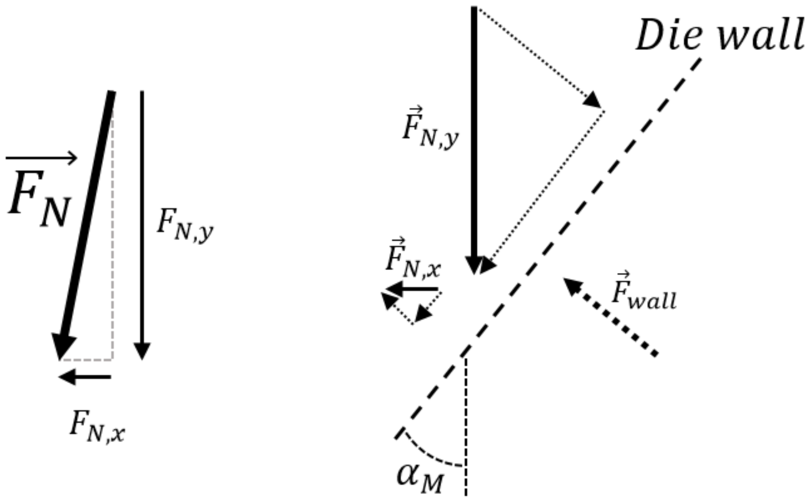

(a) x and y-component of $\vec{F}_N$.

(b) Sub-components of the x and y-component.

Figure 3.19: Components of $\vec{F}_N$.

$$\tau(M-1) = \underbrace{\frac{|\vec{F}_\mu|}{A_W}}_{\tau(M)} \cdot \frac{r_1}{R_1} \tag{3.31}$$

The ratio of the radius at the top and the bottom of the element are equal, and therefore the values of the top ratio, r_1 and R_1, have been chosen, to be used in the calculation of $\tau(M-1)$.

The shear stress at the east side of the element, $\tau(M-1)$, is converted into a shear force acting parallel to the east boundary of the element (see figure 3.18). It is calculated via equation 3.32, where:

- A_E is the east face area of the element $[m^2]$

$$\vec{F}_{\tau(M-1)} = \tau(M-1) \cdot A_E \cdot \begin{pmatrix} sin(\alpha_{M-1}) \\ cos(\alpha_{M-1}) \end{pmatrix} \tag{3.32}$$

It has to be noticed, that the x and y-components of $\vec{F}_{\tau(M-1)}$ and $\vec{F}_\mu$ must have different operational signs.

With the expressions for the forces acting on the element in figure 3.18, a force balance is set up, and the force that has to be applied to the north face of the element, $\vec{F}_N$, can be calculated. The force balance is shown in equation 3.33.

$$\vec{F}_S + \vec{F}_\mu + \vec{F}_{\tau(M-1)} + \vec{F}_N = 0 \tag{3.33}$$

Interior Element $(1 < m < M)$

The interior elements are the ones, which are not located in the columns next to the die wall or next to the symmetric axis in the center of the pellet. The force balance for these elements is identical compared to the elements near the wall, except that the shear force which acts on the west side of the elements, is not equal to the friction force appearing at the wall. Instead the shear force is calculated similar to the shear force, that acted on the east side of the element in figure 3.18. The x and y-component of the shear force on the west side of the elements, have the same operational signs as the friction force. The force balance for the interior elements is stated in equation 3.34, where:

- $\vec{F}_{\tau(m)}$ is the shear force acting on the west side of the elements $[N]$

$$\vec{F}_S + \vec{F}_{\tau(m)} + \vec{F}_{\tau(m-1)} + \vec{F}_N = 0 \tag{3.34}$$

Center Element $(m = 1)$

For the elements at the symmetric boundary axis, there are no shear force acting on the east side of the elements. This is due to the expression stated in equation 3.24. The force balance for the center elements is stated in equation 3.35.

$$\vec{F}_S + \vec{F}_{\tau(m)} + \vec{F}_N = 0 \tag{3.35}$$

Outlet Boundary Force

To calculate the force balances in the 2D model, the outlet force of the pellet channel is set as a known boundary condition. For the 1D model, a force was applied at the outlet of the channel, acting in the negative y-direction. Since the south areas of the elements in the bottom row (n=N) of the 2D model varies dependent of the radial position, an outlet pressure, P_{out}, is set instead. Using the outlet pressure, an equivalent force is calculated for each of the elements in the bottom row. The outlet pressure acts normal to the south faces of the elements in the bottom row. Therefore the x-component of outlet forces in this row equals zero. The equivalent force for the elements is defined in equation 3.36, where:

- $\vec{F}_S$ is the equivalent force acting on the south face of the element $[N]$
- A_S is the south face area of the elements $[m^2]$

$$\vec{F}_S = \begin{pmatrix} 0 \\ -P_{out} \end{pmatrix} \cdot A_S \tag{3.36}$$

3.6.3 Independence of Model Discretization

Similar to the grid independence study for the 1D model in section 3.2.5, a study of the model resolution is conducted for the 2D model. The study will be conducted for die no. 3, where the stress applied to the north face of the upper row elements, will be compared for five different discretization resolutions. The stress is defined in equation 3.37, where:

- σ_N is the normal stress that is applied to the north face of the element $[MPa]$
- $\vec{F}_{N,x}$ is the force that is applied normal to the north face of the elements $[N]$
- A_N is the north face area of the elements $[m^2]$

$$\sigma_N = \frac{\vec{F}_{N,x}}{A_N} \cdot 10^{-6} \tag{3.37}$$

The discretizations used for the independence study are shown in figure 3.20. The simulation result for the five discretization resolutions are shown in figure 3.21, where the values of σ_N is plotted for the elements in the top row, across the pellet channel. The values have been mirrored around the center axis of the pellet.

Figure 3.21 shows that the value of σ_N converges, as the resolution of the discretization increases. Though, it is seen that the magnitude of the stress, does not change much for the five resolutions. Figure 3.21 shows that the resolution of 16x16 and 32x32 elements, generates almost identical results.

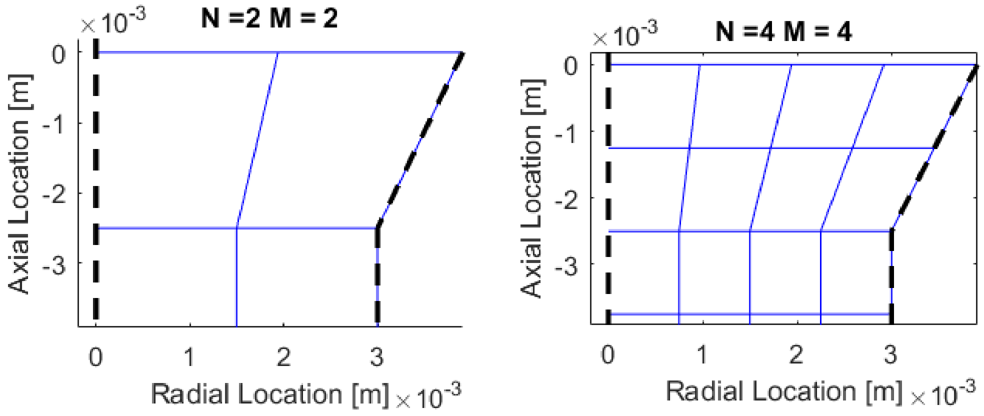

(a) $N = 2$, $M = 2$ (b) $N = 4$, $M = 4$

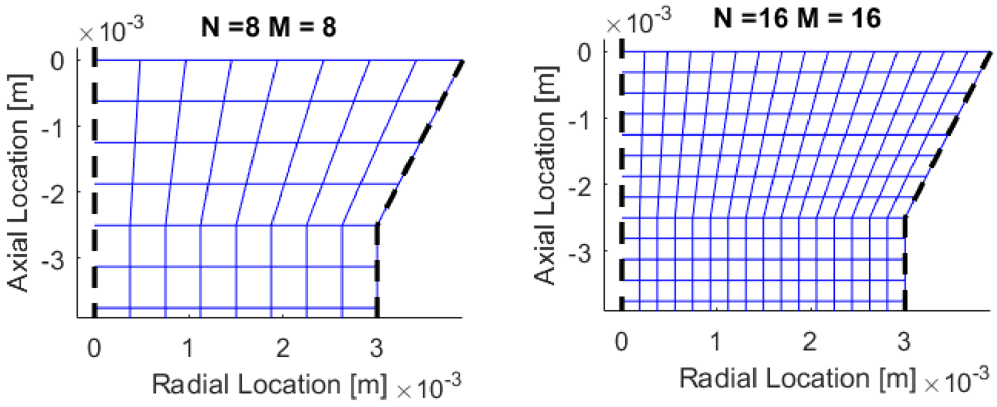

(c) $N = 8$, $M = 8$ (d) $N = 16$, $M = 16$

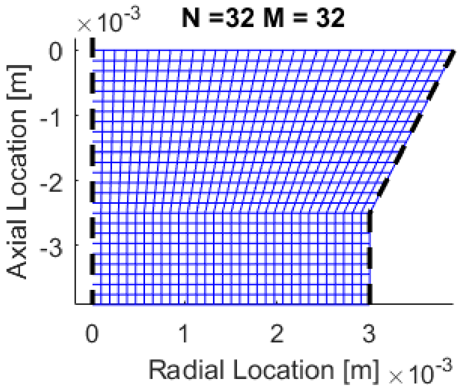

(e) $N = 32$, $M = 32$

Figure 3.20: Discretizations used for the independence study.

3.7 2D Model Simulations

To test how the 2D model performs with the current force balances, simulations of the three single dies, which were simulated in the 1D model, will be presented. A global result, where various of inlet designs are simulated, will also be presented.

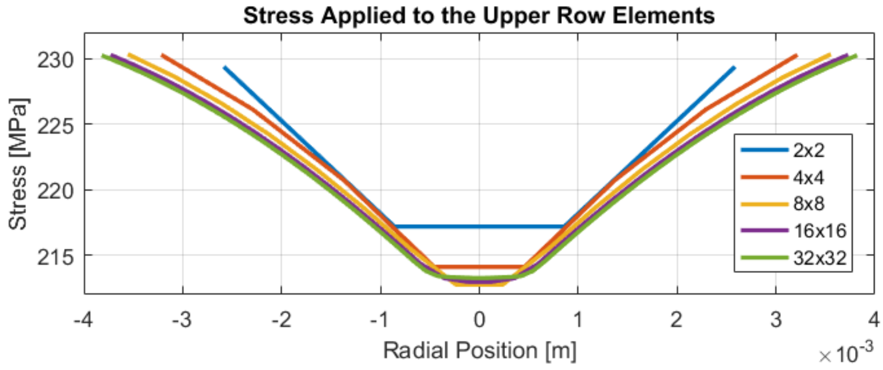

Figure 3.21: Values of σ_N for the five discretizations.

3.7.1 Single Die Simulation

To test how the simulation performs with the current force balances, a simulation of die no. 3, 6 and 11 is conducted. For the three simulations, the axial stresses will be evaluated. The axial stress is defined as the average stress applied to the north and south face of the elements, and is shown in equation 3.38, where:

- σ_{axi} is the average axial stress applied to the elements $[MPa]$

$$\sigma_{axi} = \frac{1}{2} \cdot \left(\frac{|F_{N,y}|}{A_N} + \frac{|F_{S,y}|}{A_S} \right) \tag{3.38}$$

Since the current force balances not introduces any radial stresses in the elements, the axial forces in a cylindrical channel, will be constant. The forces will only change in case that the wall of the pellet channel is not being parallel to the axial forces, which will cause friction to occur. Therefore, only the upper 5 mm of the pellet channel is simulated for the three dies. In order to visualize the simulation values of the skew elements, the element values are interpolated in to a regular grid, and shown as a contour plot. The discretization used in the three simulations, is set to 32x32 elements. The outlet pressure of the simulations is set to 354 MPa, which corresponds to a force of 10 kN acting on the radial area of the pellet.

Figure 3.22 shows the simulation result of the three dies. It is seen that the contours of the axial stresses varies for the three dies. Evaluating the stresses in the inlet of the three channels, shows that the stress is highest for die no. 3, while it is lower in die no. 6. For die no. 11, the axial stress in the inlet is much lower compared to the other two dies.

3.7.2 Global Simulation Result

To test how the 2D model performs for multiple dies, the model is run with the same combination of dies, as for the global result in the 1D model (section 3.3.2).

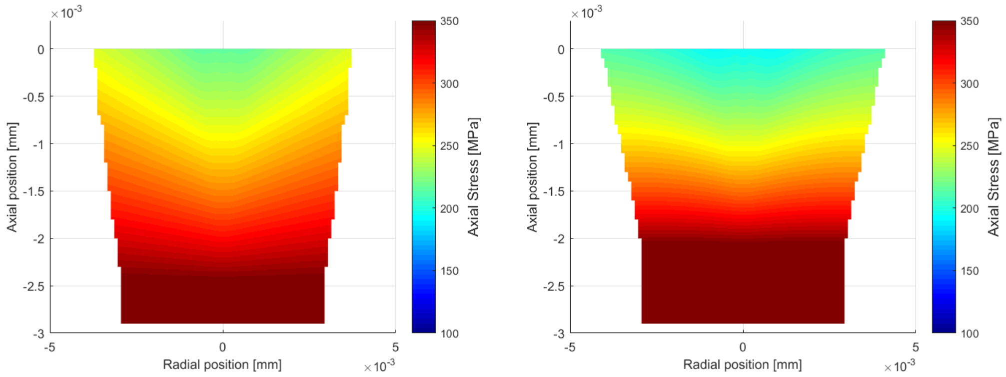

(a) Die no. 3. (b) Die no. 6.

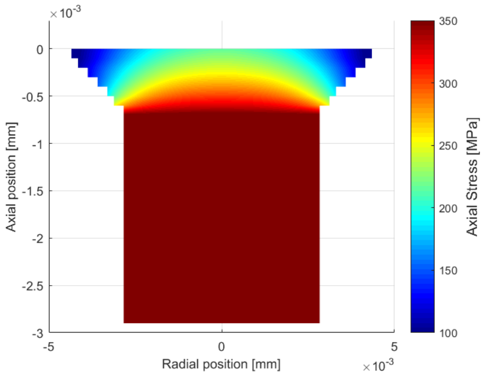

(c) Die no. 11.

Figure 3.22: 2D simulations of the three dies, showing the axial stress in the pellet channel.

The outlet pressure condition has been set to 177 MPa (corresponding to 5 kN). The magnitude of the outlet pressure is not relevant, since it is the relationship that is evaluated between the different die designs. The global result is shown in figure 3.23.

Figure 3.23 shows that the pelleting load is constant when using dies with $\alpha = 0^o$, $\alpha = 90^o$, and $z = 0$. The reason for the pelleting load being equal in all of these dies, is that they all are cylindrical channels without an inlet. Additionally it is seen in figure 3.23, that the highest pelleting load is observed for inlet angels of $\alpha = 50^o$, and that the pelleting load increases, when the chamfer depth is increased.

3.8 Validation of the 2D model

Similar to the 1D model, the 2D model will be compared and validated with the experimental results from the 9th semester. The required pelleting load for the 2D model is defined as the sum of the forces, $\vec{F}_N$, acting on the north face of the elements in the top row. In order to compare the pelleting load in the 2D model with the experimental results, the pelleting load is normalized for the experiments and the

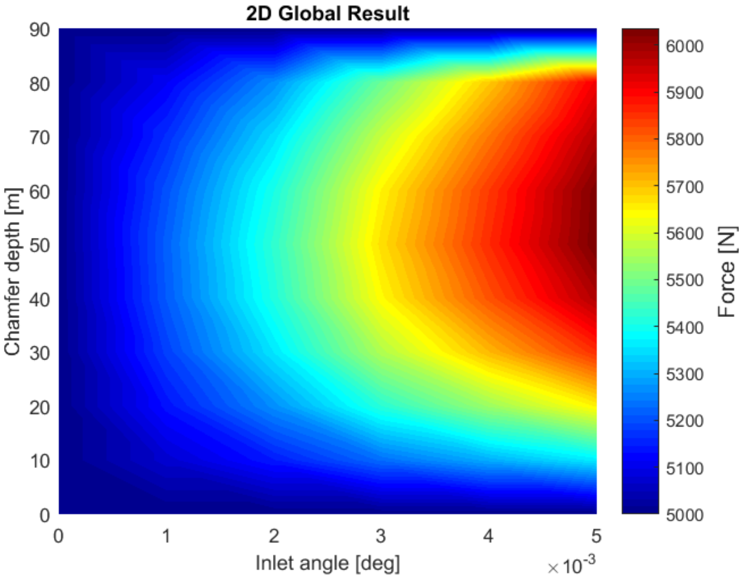

Figure 3.23: The global result of the pelleting load, simulated with the 2D model.

simulation results. They are normalized by dividing the pelleting load for each die, with the pelleting load for die with the lowest load. The reason for normalizing the results, is that the 2D model does not account for the effect of Poisson's ratio. Therefore a high outlet pressure will have to be set for the 2D model, in order to be directly comparable to the experimental results. Instead the results are normalized.

Figure 3.24 shows the normalized pelleting loads from the 2D model and the experiments. Compared to the 1D model, the 2D model simulates correct tendencies of the inlet designs, where the pelleting load is lowest for the die without any inlet. The scales in figure 3.24 shows that the deviation between the dies in the experiment, is larger than the simulated dies.

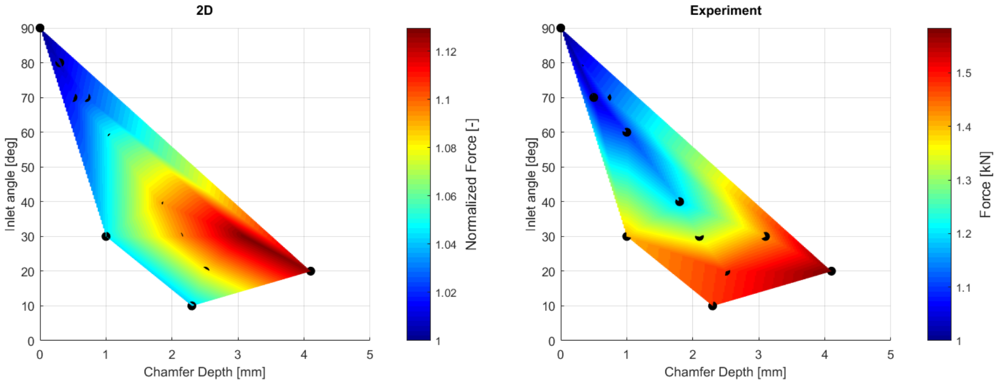

(a) 2D simulation. (b) Experiment.

Figure 3.24: Normalized pelleting loads.

The larger deviation of the pelleting loads in the experiment, compared to the 2D model, can be caused by the radial stresses from Poisson's ratio not are included in the 2D model. If the radial stresses are included in the force balances, the stress on the die wall will increase, and a higher friction force will appear. The radial stresses will also introduce a upward shear stress, that will work against the flow. Figure 3.25 illustrates the forces that will appear in the elements as a consequence of the radial forces from Poisson's ratio, where:

- $\vec{F}_{rad}$ is the radial force appearing as a function of the force applied from $\vec{F}_{N,x}$ $[N]$
- $\vec{F}_{up}$ is the shear force acting against the flow direction $[N]$
- $\vec{F}_{wall}$ is the extra force acting on the wall of the die $[N]$

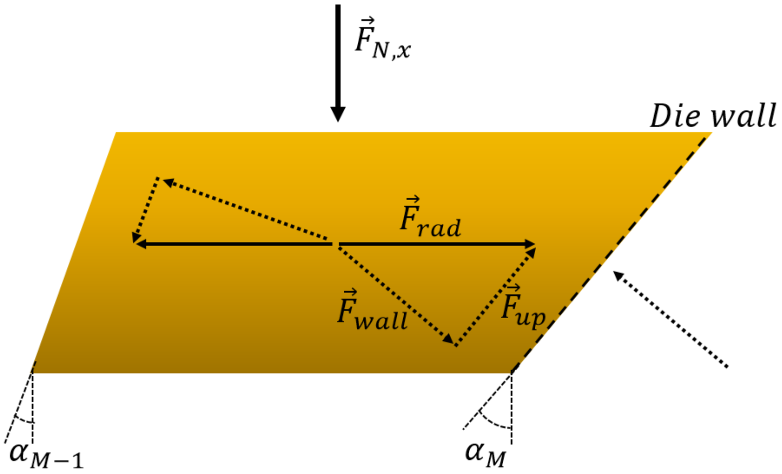

Figure 3.25: The forces that will appear as a consequence of Poisson's ratio.

Including Poisson's ratio in the 2D model will therefore increase the force acting on the wall, and increase the friction in the inlet, which will reduce the deviation between the experiments and the 2D simulation results.

3.9 Evaluation of the Numerical Models

The numerical models in this project are the first step in order to be able to simulate complex pelleting processes. The set up of the models entails some assumptions for the process. Further studies of the pelleting process can provide useful knowledge, which can be implemented in the models.

Friction Factor

One of the key parameters in the model is the friction factor, μ. To illustrate this, figure 3.26 shows three simulations from the 1D model, where μ is changed. The dotted lines represent values of μ that is ±0.5 of the value used in the simulations in this project.

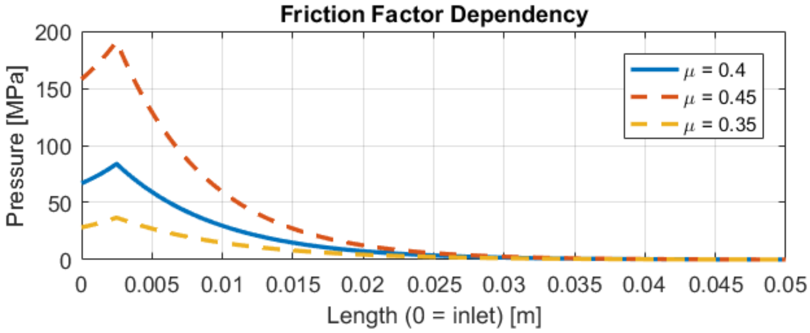

Figure 3.26: Parameter study of the friction factor.

The simulation results in figure 3.26 shows, that the friction factor is a key parameter, and it has a great impact on the output of the simulations. In order to select the right friction factor for the models, a thorough review of published articles has been done, with the conclusion that a very limited amount of data is available. Therefore further studies of determining μ is important for improving the performance of the models.

Material Behavior

An important part of the pelleting process is how the pelleting material behaves during the compression through the pellet channel. The models in this study assumes an elastic behavior of the pelleting material. From the compression tests a viscoplastic behavior [24] was observed, where the elastic stress from a compression, reduces by time, and the pelleting material ”relaxes”, to a certain plastic deformation. The time dependent behavior of the pelleting material is shown in figure 3.27, which shows data from one of the compression tests. The pelleting material was compressed for the first 30 seconds, where after the piston position is held constant for the remaining 17 seconds.

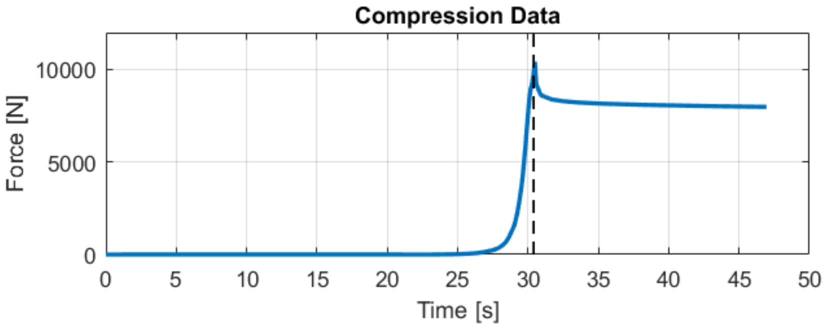

Figure 3.27: Viscoplastic behavior observed at compression test.

There are material models, which can describe viscoplastic behavior, but these are complex, and demands further studies of the pelleting material, though this has been out of the scope for this project. Implementing a material model for the viscoplastic behavior, properly can improve the model performance. In this project, modeling with elastic material behavior has shown to produce good simulations, which can describe the pelleting process.

Flow Profile

In order to simulate the flow of the pelleting material in the die, the rheology of the pelleting material has to be determined. In fluid dynamics, a commonly used rheology model is the Newtonian fluid, which for an example is used for water. It is far from all fluids that obey the criteria for a Newtonian fluid, and these are categorized as non-Newtonian fluids. Non-Newtoninan fluids is divided into several sub-categories, examples are; shear-thinning, shear-thickening and Bingham plastics [25].

Bingham plastics are fluids that appear with solid properties under certain conditions. These materials have a yield stress, τ_{yield}, which defines the magnitude of shear stress, that the material can withstand before it starts to flow. At shear stresses below the yield stress, the material is a rigid solid. Relating this scenario to pelleting of wood, τ_{yield} correspond to the point where the shear stresses exceeds the adhesion of the wood particles, and the particles start to flow. Though it can be imagined, that τ_{yield} is dependent of multiple of properties. It will require further studies to determine a rheology model, that can describe the pelleting material, since the currently available rheology models properly are not able to fully describe the the pelleting process.

In addition to the non-Newtonian behavior it can be imagined, that solidification models shall be implemented, in order to model the ”solidification” of the pelleting material. Solidification models are commonly used when simulating moulding processes. Examples of solidification models are the Apparent Heat Capacity Method and the Enthalpy Method [26]. In the Enthalpy Method, the enthalpy of the material is varied in the state between two phases, in order to model the latent heat. In terms of the pelleting material, it can be imagined that by simulating a viscosity of the pelleting material, a solidification model can be set up, where the solidification conditions are determined as a function of the pressure and temperature. Below these conditions, the pelleting material will behave as a fluid (low viscosity), at the solidification conditions the viscosity will increase, until it reaches conditions that are above the solidification conditions, where the material will be a solid (extremely high viscosity).

The flow of the pelleting material has not been in focus for this project. For future studies, visual inspections of the pellets, like the ones conducted during the hardness tests in this project, can provide useful knowledge of the rheology for the pelleting material.

CHAPTER 4

Conclusion

During this project, the following has been obtained.

- A thorough review of the pelleting process has been conducted, describing the knowledge that is available and presented published results from previous studies.
- Experiments has been conducted. The results has been implemented in the numerical models, and used as validation of these.
- Two numerical models has been set up in order to determine how the die design affects the pelleting process.

The first model is a 1D model, which evaluates the pellet channel in the axial direction. In order to determine the load that is required to extrude new pelleting material into the pellet channel, an expression for the friction appearing on the wall of the die was set up, based on Poisson's ratio for the pelleting material. Validation of the 1D model showed that it performs good in terms of simulating the required pelleting load for pellet channels without any inlet section. Though it is not able to simulate the pelleting load when conical inlets are added to the pellet channel. Figure 4.1 shows the comparison of the 1D model and the experimental data.

Evaluating the pressure in the pellet channel, showed that the pressure peaks at the interface between the inlet section and the cylindrical channel. This corresponds well to the fact that the wear of the pellet channel is observed at this location.

Expressions for the energy consumption in the pellet channel were included in the 1D model. The energy was divided into a friction and a compression contribution. To determine the energy consumption for compressing the material, an empirical expression for the density as a function of the pressure, was set up. The expression is based on experimental compression tests, which has been conducted. Evaluating the energy consumption in the pellet channel, it was observed that the material only is compressed in the inlet section of the pellet channel, and that the amount of energy used for compression is $\approx \frac{1}{7} \sim \frac{1}{8}$ of the frictional energy.

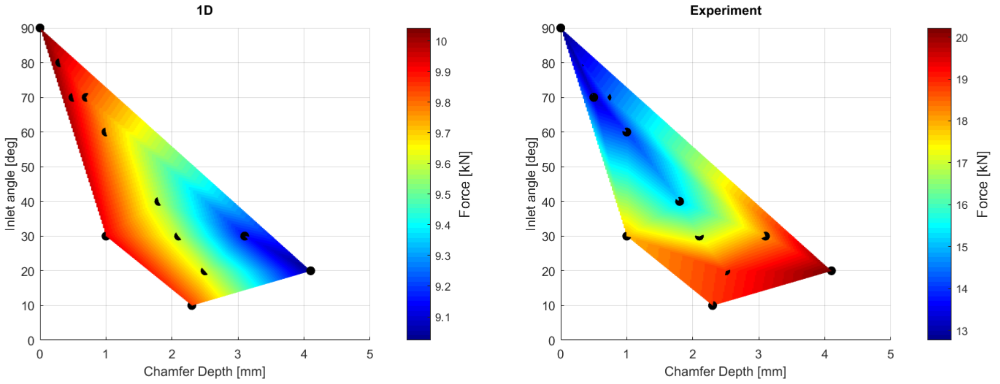

(a) 1D simulation.

(b) Experiment.

Figure 4.1: Pelleting loads.

Based on the fact that the 1D model is not able to simulate correct pelleting loads for dies with an inlet, a 2D axis symmetric model was set up. Validation of the 2D model, showed that the tendencies of the simulated pelleting loads corresponds well to the experimental data, used for the validation. The 2D model thereby confirms the conclusions from a previous study in 9^{th} semester, that a pellet channel without an inlet, has the smallest pelleting load, and thereby the smallest energy requirement. Figure 4.2 shows the comparison of the 2D model and the experimental data.

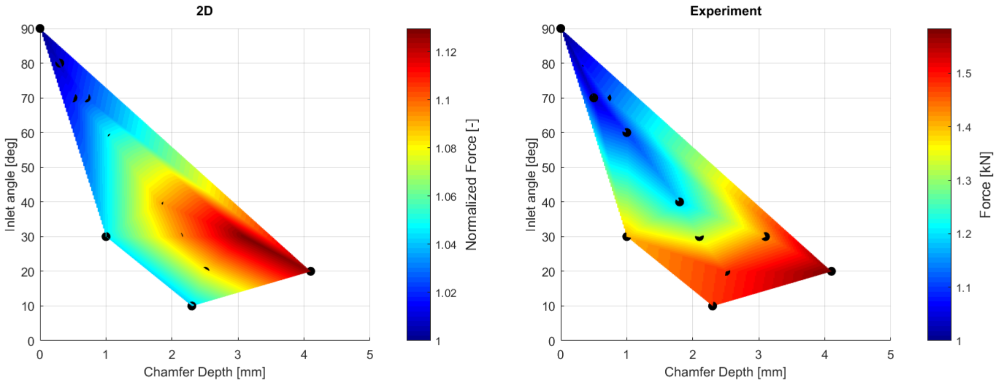

(a) 2D simulation.

(b) Experiment.

Figure 4.2: Normalized pelleting loads.

To evaluate the local density inside a pellet, pellets have been produced in single dies. The pellets were embedded in epoxy and sanded down, such that a cross sectional view of the pellets appeared in the epoxy. Measurements of the pellet hardness was conducted, and showed tendencies of the hardness changing dependent of the inlet design of the die. To link the hardness of the pelleting material to its density, samples of pelleting material was compressed to different densities. Hardness measurements of the density samples showed that the hardness of the pelleting material is linked to the density, and that raising the density increases the hardness of the pelleting material.

In order to simulate the density in the pellet channel with the 2D model, further work has to be done. Though this was not the primary goal of the project.

The numerical models has been set up in the program Matlab. The structure of the models allows the properties of the pelleting material to easily be changed, likewise the dimensions of the die.

Bibliography

[1] Simon K. Nielsen. Study of a pelleting process and its dependency of inlet design and temperature. Student report from AAU.

[2] Peter Thomsen. *Dong Energy's Implementering af Dansk Brancheaftale*. Dong Energy, oct 2015.

[3] Jack Huang. Wood pellet global market report 2014. $http://greenmaltese.com/wp-content/uploads/sites/20/2012/01/NIST-Conduction_2.jpg$, jan 2015.

[4] Niels Peter Kjeldsen Nielsen. *Importance of raw material properties in wood pellet production: effects of differences in wood properties for the energy requirements of pelletizing and the pellet quality*. PhD thesis, Forest & Landscape, University of Copenhagen, 2009.

[5] Wolfgang Stelte. *Fuel Pellets from Biomass*. PhD thesis, Danish National Laboratory for Sustainable Energy , Technical University of Denmark, dec 2011.

[6] Andritz Feed and Biofuel. Pelleting solutions making biomass to homogene fuel. pptx.

[7] Wolfgang Stelte, Jens K. Holm, Anand R. Sanadi, Søren Barsberg, Jesper Ahrenfeldt, and Ulrik B. Henriksen. Fuel pellets from biomass: The importance of the pelletizing pressure and its dependency on the processing conditions. *Fuel*, 90(11):3285 – 3290, 2011.

[8] Torben Poulsen Claus Felby Niels Peter Kjeldsen, Douglas J. Gardner. Importance of temperature, moisture content, and species for the conversion process of wood residues into fuel pellets. *Wood and Fiber Science*, 41(4):414–425, 2009.

[9] Wangaard FF Kellogg RM. Variation in cell-wall density of wood. *Wood Fiber Science*, 1:180–204, 1969.

[10] Callum A. S. Hill, Graham A. Ormondroyd, and Graham A. Ormondroyd. Dimensional changes in corsican pine (pinus nigra arnold) modified with acetic anhydride measured using a helium pycnometer. 58:544–547, 2004.

[11] L.G. Shaw, M.D.; Tabil. Compression, relaxation, and adhesion properties of selected biomass grinds. *International Commission of Agricultural Engineering*, 9:E–Journal, aug 2007.

[12] Anand R. Sanadi Søren Barsberg Jesper Ahrenfeldt Ulrik B. Henriksen Wolfgang Stelte, Jens K. Holm. A study of bonding and failure mechanisms in fuel pellets from different biomass resources. *Biomass and Bioenergy*, 35(2):910 – 918, 2011.

[13] Jens Bo Holm Nielsen. Optimized biogas production by utilization the primary agricultural products: Manure and lignocellulosic crop and crop by-products. Aalborg University, Inst. of Energy Technology, 2015.

[14] Susanne Merk, Alfred Blume, and Markus Riederer. Phase behaviour and crystallinity of plant cuticular waxes studied by fourier transform infrared spectroscopy. *Planta*, 204:44–53, 1997.

[15] Jacob J. Bikerman and Jacob J. Bikerman. Causes of poor adhesion: Weak boundary layers. *Industrial and Engineering Chemistry*, 59:40–44, 1967.

[16] Tangram Technology. Low temperature plastics. $http : //www.tangram.co.uk/TI - Polymer - Low_{t}emperature_{p}lastics.html.$

[17] P. J. Denny. Compaction equations: a comparison of the heckel and kawakita equations. 127:162–172, 2002.

[18] T. Comoglu. An overview of compaction equations. *Journal of Faculty of Pharmacy*, 36:123–133, 2007.

[19] Matam inc. Pellet durability index test procedure.

[20] Niels Peter K. Nielsen, Jens Kai Holm, and Claus Felby. Effect of fiber orientation on compression and frictional properties of sawdust particles in fuel pellet production. *Energy & Fuels*, 23(6):3211–3216, 2009.

[21] S. Z. Qamar. Shape complexity, metal flow, and dead metal zone in cold extrusion. *Materials and Manufacturing Processes*, 25(12):1454–1461, 2010.

[22] Johan E. Hustad Lasse H. Sørensen Jens K. Holm, Ulrik B. Henriksen. Toward an understanding of controlling parameters in softwood and hardwood pellets production. *Energy & Fuels*, 20(6):2686–2694, 2006.

[23] U.S. Department of Agriculture Forest Service. *Wood Handbook - Wood as an Engineering Material.* Forest Products Laboratory, 1999.

[24] Abhijit P.; Kumar P. B. Sunil Krishnan, J. Murali; Deshpande. *Rheology of Complex Fluids*. Springer New York, 2010.

[25] Theodore H.; Huebsch Wade W.; Rothmayer Alric P. Munson, Bruce R.; Okiishi. *Fluid Mechanics*. John Wiley & Sons, seventh edition, 2013.

[26] Henry Hu and Stavros A Argyropoulos. Mathematical modelling of solidification and melting: a review. *Modelling and Simulation in Materials Science and Engineering*, 4(4):371, 1996.

[27] matweb.com. Overview of materials for t 300 series stainless steel. *http : //www.matweb.com/search/datasheet.aspx?matguid = 7a87941825a3463eaba7979c4333721fckck* = 1.

[28] Johan E. Hustad Jens K. Holm, Ulrik B. Henriksen and Lasse H. Sørensen. Toward an understanding of controlling parameters in softwood and hardwood pellets production. 20:2686–2694, 2005.

[29] M. Thomas, M. Thomas, and T. Van Vliet. Physical quality of pelleted animal feed 3. contribution of feedstuff components. 70:59–78, 1998.

[30] Douglas J. Gardner, Leslie H. Stokke, Douglas D. ; Groom, Leslie H. Groom, and Douglas D. Stokke, editors. *Adhesion Mechanisms of Durable Wood Adhesive Bonds*, pages 254–265. 2006.

List of Figures

List of Tables

4.1 Appendix 1

4.1.1 Test Procedure [1]

The eucalyptus tree was ordered for a previous full scale test. The eucalyptus was received as chips, and has been grinded in a hammer mill with a screen size of $4\,mm$. For the tests in this project, a bag of $20\,kg$ grinded material was provided. Two samples of each $20\,g$ was collected to determine the MC of the material. The samples was heated to 105^oC in a drying chamber for 24 hours, to evaporate the moisture from the material. The difference in weight as received (as) or wet basis (w.b) and on dry basis (d) expresses the moisture content in the material, which is expressed on wet basis in equation 4.1 where:

- $M_{(w.b)}$ is the mass of the sample as received $[kg]$.
- $M_{(d)}$ is the mass of the sample on dry basis $[kg]$.

$$MC\%(w.b) = 1 - \frac{M_{(d)}}{M_{(w.b)}} \tag{4.1}$$

The results of the drying process are listed in table 4.1.

Sample no.	$M_{(w.b)}$ $[g]$	$M_{(d)}$ $[g]$	$MC\%(w.b)$ $[-]$
1	20.00	18.24	8.80%
2	20.00	18.20	9.00%
Average	20.00	18.22	8.90%

Table 4.1: Results of the MC measurements

4.1.2 Stress Calculations [1]

The force from the test station is applied to the top of the press piston, which has an diameter of $7.5\,mm$. The highest stress is applied on the top of the press piston, since this is where the diameter ($7.5\,mm$) and thereby the contact area is smallest. The bottom diameter of the press piston equals the press channel diameter of $9.5\,mm$, and thereby the stress/pressure is lower at this point, compared to the top of the piston. The compression force can be converted to pressure by using equation 4.2 where:

- P is the pressure acting on the area A $[Pa]$.
- A is the area which the pressure P acts on $[m^2]$.
- F is the force provided from the compression station $[N]$.

$$P = \frac{F}{A} \tag{4.2a}$$

$$P_{pellet} = \frac{21 \cdot 10^3 N}{\pi \cdot \frac{1}{4} \cdot (9.5 \cdot 10^{-3} mm)^2} = 296.3 MPa \tag{4.2b}$$

$$P_{top.piston} = \frac{21 \cdot 10^3 N}{\pi \cdot \frac{1}{4} \cdot (7.5 \cdot 10^{-3} mm)^2} = 475.3 MPa \tag{4.2c}$$

The compression limit corresponds to a pressure of $\approx 300 MPa$ in the bottom of the press piston, which is valid for a full scale pelleting process. The pressure acting on the top of the press piston is $\approx 475 MPa$ at the limit, which does not cause any deformations of the press piston.

4.2 Appendix 2 - *Matlab* Codes

4.2.1 1D Model - Single Die Simulation

```
%% Area functions of the pellet channel
%clc
%clear
%% Geometrical dimensions of the pellet channel.
    %These must be set for each simulation
L = 50E-3;      %Length of the pelleting channel [m]
D = 6E-3;       %Diameter of the pelleting channel [m]
C_a = 0.7E-3;   %Chamferig height of inlet [m]
alpha = 70;     %Inlet angle [deg]

%% Settings for the simulation
m_dot = 0.000374; %Mass flow pr. pellet channel [kg/s]
mu = 0.4;         %Friction coefficient [-]
G = 20.7;         %Ratio between E_l and E_r
nu = 0.025;       %Poissons ratio
N = 4000;         %Number of elements in the axial direction

dx = L/N;                   %Step size in axial direction [m]
alpha = degtorad(alpha);    %Inlet angle in radians
r_p = D/2;                  %Radius of the pellet [m]

N_inlet = round(C_a/dx); %Number of elements (axial) in the inlet [-]
N_channel = round((L-C_a)/dx); %Number of elements (axial)
                               %in the channel [-]

%Diameter of the discs in the inlet [m]
C_rad = zeros(N_inlet,1);
for j = 1:N_inlet;
C_rad(j) = tan(alpha)*((N_inlet-(j-1))*dx-0.5*dx);
end

% Axial surface area of the discs in the entire pelleting channel [m]
A_disk = zeros(N,1);
for j = 1:N;
 if j <= N_inlet;
     A_disk(j,1) = pi*(r_p+C_rad(j))^2; %Surface areas of the elements
                                        %in the inlet [m^2]
 else
     A_disk(j,1) = pi*(r_p)^2; %Surface areas of the elements
                               %in the pellet channel [m^2]
 end
end
```

```
% Radial surface area of the discs in the entire pelleting channel [m]
A_rad = zeros(N,1);
for j = 1:N;
 if j <= N_inlet;
     A_rad(j,1) = pi*(r_p+C_rad(j))*2*dx; %Surface areas of the
                                          %elements in the inlet [m^2]
 else
     A_rad(j,1) = pi*r_p*2*dx; %Surface areas of the elements
                               %in the pellet channel [m^2]
 end
end

% Force coefficient for each element
F_e = zeros(N,1);
for j = 1:N;
    if j<=N_inlet;
    F_e(j) = mu*G*nu*2*dx/(r_p+C_rad(j));
    else
    F_e(j) = mu*G*nu*2*dx/r_p;
    end
end

% Volume of the disks
V = zeros(N,1);
for j = 1:N;
    V(j) = A_disk(j)*dx;
end

%% Force Calculations
F_out = 0.1; %Force at the outlet of the channel [N]
F_in=zeros(N,1);

for j = 1:N;
F_in(end+1-j) = F_out/(1-F_e(end+1-j));
F_out = F_in(end+1-j);
end

F_wall = zeros(N,1);
F_wall = (F_e/mu).*F_in;


%% Density in the nodes as a function of the pressure
pressure = zeros(N,1);
pressure = 1/3*((F_in./A_disk)+2*F_wall)*10^(-6);

rho = zeros(N,1);
for j = 1:N;
rho(j) = rho_p(pressure(j));
```

```
if j == 1
    rho(j) = rho(j);
else
      if rho(j) < rho(j-1);
         rho(j) = rho(j-1);
      else
         rho(j) = rho(j);
      end
end
end
V_spec = zeros(1,N);
for j = 1:N
    V_spec(j) = 1/rho(j);
end
%% Compression energy
a = 318.989; %Empirical coeficients from compression test
b = 0.324;
c = 82.694;

rhos =@(x) 10^6*((1/a)*x.^(-1)-(c/a)).^(1/b); %Pressure/density function

  Q_comp = zeros(N,1);
  for j = 1:N;
      if j == 1;
          Q_comp(j) = integral(rhos,V_spec(1),0.0072)*V(1)*rho(1);
      else
          Q_comp(j) = integral(rhos,V_spec(j),V_spec(j-1))*V(j)*rho(j);
      end
  end

Q_comp_cum = zeros(N,1);
Q_comp_cum = cumsum(Q_comp); %Accumulated compression energy

%% Calculation of the element velocity
m_trans = zeros(N,1);
m_akk = zeros(N,1);
Vol_node = zeros(N,1);
vel_node = zeros(N,1);
for j = 1:N;
m_trans(j) = m_dot;
m_akk(j) = rho(j)*V(j);
Vol_node(j) = (m_trans(j)./rho(j));
vel_node(j) = Vol_node(j)./A_disk(j);
end

res_time = zeros(N,1);
for j = 1:N;
    res_time(j) = dx/vel_node(j); % Residence time in the elements
```

```
end

tot_res = cumsum(res_time);
tot_res = tot_res(end); %Residence time in the pelleting channel [s]



%% Friciton energy

Q_dot_fric = zeros(N,1);
for j = 1:N;
Q_dot_fric(j) = F_wall(j).*dx*mu; %Energy dissipated in the elements
end
Q_dot_fric_cum = cumsum(Q_dot_fric); %Accumulated
                                     %Energy dissipated in the elements
Q_tot_energy = Q_dot_fric_cum + Q_comp_cum; %Total energy consumption


%% Plots
Pos = zeros(N,1);
for j = 1:N;
    Pos(j) = j*dx-dx; %Element position in the channel
end
Pellet_dim = zeros(N,1);
for j = 1:N;
    if j <= N_inlet
        Pellet_dim(j) = C_rad(j)+r_p; %Radial size of the elements
    else
        Pellet_dim(j) = r_p;
    end
end

Pellet_dim = Pellet_dim*1E3;

figure(1)
subplot(2,1,1)
[ax,p1,p2]=plotyy(Pos,F_in,Pos,Pellet_dim); %Plots the force in the channel
set(p1,'LineWidth',2);
set(p2,'LineWidth',2);
title('Pelleting Force')
xlabel(ax(1),'Length (0 = inlet) [m]')
ylabel(ax(1),'F_{top} [N]')
ylabel(ax(2),'Die wall [mm]')
legend([p1,p2],'Force','Die wall')
ylim(ax(2),[0 10])
grid on

subplot(2,1,2)
```

```
[ax,p1,p2]=plotyy(Pos,pressure,Pos,rho); %Plots the pressure and density
set(p1,'LineWidth',2);
set(p2,'LineWidth',2);
title('Pressure and Density Variation')
xlabel(ax(1),'Length (0 = inlet) [m]')
ylabel(ax(1),'Pressure [MPa]')
ylabel(ax(2),'Density [kg/m^3]')
legend([p1,p2],'Pressure','Density')
grid on

figure(2)
plot(Pos,vel_node)                          %Plots the velocity of the
                                              %pelleting material
xlabel('Length (0 = inlet) [m]','FontSize',14)
ylabel('Velocity [m/s]','FontSize',14)

grid on
%% Grid Independence plot
C = F_max; %Force values of the different discrtizations
 N_n = (1:1:t);
 N_n = N_n*100;
 %N_n = N_n*100;
 figure(3)
 subplot(2,1,1)
 plot(N_n,C,'o')
title('Required Pelleting Force')
xlabel('Number of elements, N [-]')
ylabel('Roll force [N]')
grid on

 err = zeros(t,1);
 for j = 2:t;
 err(j) = abs(100*(C(j)-C(j-1))./C(j-1));
 end
 subplot(2,1,2)                     % Plot for the scaled residual
 semilogy(N_n(2:t),err(2:t),'LineWidth',2)
 title('Force Residual')
xlabel('Number of elements, N [-]')
ylabel('Residual (%)')
 grid on

 %% Contour plots of the energy consumption in the die
figure(4)
subplot(2,2,1)
surf(angle',chamfer.*1000,Q_tot_fric'./3600)
view(0,90)
shading interp;
lighting gouraud
```

```
colormap(jet)
colorbar;
%caxis([1200 1550])
%xlim([10 gg*10-9])
%ylim([0.0001 kk*0.0005-0.0004])
xlabel('Inlet Angle [deg]','FontSize',14)
ylabel('Chamfer Depth [mm]','FontSize',14)
%clabel('kWh/ton')
title('Friction Work [kWh/ton]','FontSize',18)

subplot(2,2,2)
surf(angle',chamfer.*1000,Q_tot_comp'./3600)
view(0,90)
shading interp;
lighting gouraud
colormap(jet)
colorbar
%caxis([1200 1550])
%xlim([10 gg*10-9])
%ylim([0.0001 kk*0.0005-0.0004])
xlabel('Inlet Angle [deg]','FontSize',14)
ylabel('Chamfer Depth [mm]','FontSize',14)
title('Compressional Work [kWh/ton]','FontSize',18)

Q_tot = (Q_tot_comp+Q_tot_fric)./3600;

subplot(2,2,3)
surf(angle',chamfer.*10^3,Q_tot')
view(0,90)
shading interp;
lighting gouraud
colormap(jet)
colorbar
%caxis([1200 1550])
%xlim([10 gg*10-9])
%ylim([0.0001 kk*0.0005-0.0004])
xlabel('Inlet Angle [deg]','FontSize',14)
ylabel('Chamfer Depth [mm]','FontSize',14)
title('Total Energy Consumption [kWh/ton]','FontSize',18)
%% Plot of energy consumption in the channel
figure(5)
Q_comp(1)=Q_comp(2);
subplot(2,1,1)
plot(Pos,Q_fric,'LineWidth',2)
hold on
plot(Pos,Q_comp,'LineWidth',2)
xlabel('Position (0 = inlet) [m]')
ylabel('Energy [J]')
```

```
legend('Friction energy','Compression Energy','Location','NorthEast')
title('Compression and Friction Energy')
grid on

subplot(2,1,2)

plot(Pos,Q_tot_energy,'LineWidth',2)
xlabel('Position (0 = inlet) [m]')
ylabel('Energy [J]')
title('Accumulated Energy')
legend('Cumulated Energy','Location','SouthEast')
grid on
```

1D Model - Contour plot

```
%% Display 1D model results on a die shaped contour plot, Density
E_axi = N_inlet;
N_rad = round((r_p+C_rad(1))/dx);
E_rad = zeros(N_rad,1);

for j = 1:N;
    if j <= N_inlet
    E_rad(j) = round((r_p+C_rad(j))/dx);
    else
    E_rad(j) = round(r_p/dx);
    end
end

Dis = zeros(N,N_rad);
for m = 1:N;
    for n = 1:N_rad;
        if n <= E_rad(m);
        Dis(m,n) = rho(m);
        else
        Dis(m,n) = NaN;
        end
    end
end

Sid = zeros(N,N_rad);
for m = 1:N;
    for n = 1:N_rad;
        Sid(m,n) = Dis(m,end+1-n);
    end
end

Dis = [Sid Dis];
```

```
P_axi = zeros(N,1);
for j = 1:N;
    P_axi(j) = j*dx*1000;
end
P_rad = zeros(2*N_rad,1);
for j = 1:2*N_rad;
    P_rad(j) = (j-N_rad-1)*dx*1000;
end
P_rad = P_rad';
figure(3)

C = Dis;
surf(P_rad,P_axi,Dis,C)
view(0,-90)
shading interp;
lighting gouraud
colormap(jet)

xlim([P_rad(1) P_rad(end)])
ylim([0 7])
xlabel('Radial position [mm]','FontSize',14)
ylabel('Axial position [mm]','FontSize',14)
title('Density Variations in the Pelleting Channel','FontSize',18)

%% Pressure contours
Dis = zeros(N,N_rad);
for m = 1:N;
    for n = 1:N_rad;
        if n <= E_rad(m);
        Dis(m,n) = pressure(m);
        else
        Dis(m,n) = NaN;
        end
    end
end

Sid = zeros(N,N_rad);
for m = 1:N;
    for n = 1:N_rad;
        Sid(m,n) = Dis(m,end+1-n);
    end
end

Dis = [Sid Dis];
figure(8)
subplot(2,2,2)
```

```
C = Dis;
surf(P_rad,P_axi,Dis)
view(0,-90)
shading interp;
lighting gouraud
colormap(jet)
caxis([30 100])
c=colorbar
ylabel(c,'Pressure [MPa]','FontSize',12)
xlim([P_rad(1) P_rad(end)])
ylim([P_axi(end)])
xlabel('Radial position [mm]','FontSize',14)
ylabel('Axial position [mm]','FontSize',14)
title('Pressure in the Pelleting Channel')
hold on
```

4.2.2 2D Model - Grid Generation

```
%% Two dimensional axissymmetric model
 clc
 clear

%% Geometrical dimensions of the pellet channel.
%These must be set for each simulation
angle = 20 %[10 20 20 30 30 30 40 70 60 70 80];
chamfer = 0.0025 %[2.3 2.5 4.1 1 2.1 3.1 1.8 0.5 1 0.7 0.3];

%for i = 1:size(angle,2)
   % for j = 1:size(chamfer,2)
L = 8E−3;                    %Length of the pelleting channel [m]
D = 6E−3;                    %Diameter of the pelleting channel [m]
C_a = chamfer(1);            %Chamfer depth [m]
alpha = angle(1);            %Inlet angle [deg]
alpha = degtorad(alpha);     %Inlet angle in radians
r_p = D/2;                   %Radius of the pellet [m]

%% Settings for the simulation
N_x =150; %Number of elements in the axial direction [−]
N_r = 40; %Number of elements in the radial direction [−]

dx = L/N_x; %Element size in axial direction [m]
dy_c = r_p/N_r; %Element size in radial direction in the channel [m]


N_x_i = round(C_a/dx); %Number of axial elements  in the inlet [−]
N_x_c = N_x−N_x_i; %Number of axial elements in the channel [−]

%% Channel grid

%North & South areas of the elements
A_n_c = zeros(N_x_c,N_r);
A_s_c = zeros(N_x_c,N_r);
for i = 1:N_x_c
for j = 1:N_r
    A_n_c(i,j) = area_ring(j*dy_c,(j−1)*dy_c);
end
end
A_s_c = A_n_c;

%East & West areas of the elements
A_e_c = zeros(N_x_c,N_r);
A_w_c = zeros(N_x_c,N_r);
for i = 1:N_x_c
```

```
for j = 1:N_r
    A_e_c(i,j) = area_oc((j-1)*dy_c,dx);
end
end
for i = 1:N_x_c
for j = 1:N_r
    A_w_c(i,j) = area_oc(j*dy_c,dx);
end
end

%Volume of the elements
V_c = zeros(1,N_r);
for j = 1:N_r
    V_c(j) = A_n_c(j)*dx;
end

%% Inlet grid
sub_alpha = zeros(1,N_r+1);
for j = 1:N_r+1
    sub_alpha(j) = (j-1)*(alpha/N_r);
end

%North areas of the elements
A_n_i = zeros(N_x_i,N_r);
for j = 1:N_r
    for i = 1:N_x_i
    A_n_i(i,j) = area_ring(j*dy_c+tan(sub_alpha(j+1))*(dx*(N_x_i-i+1)),...
        (j-1)*dy_c+tan(sub_alpha(j))*(dx*(N_x_i-i+1)));
    end
end


%South areas of the elements
A_s_i = zeros(N_x_i,N_r);
for j = 1:N_r
    for i = 1:N_x_i
    A_s_i(i,j) = area_ring(j*dy_c+tan(sub_alpha(j+1))*(dx*(N_x_i-i)),...
        (j-1)*dy_c+tan(sub_alpha(j))*(dx*(N_x_i-i)));
    end
end

%East areas of the elements
A_e_i = zeros(N_x_i,N_r);
for j = 1:N_r
    for i = 1:N_x_i
        if j == 1
            A_e_i(i,j) = 0; %Area in the axissymmetri
        else
```

```
            A_e_i(i,j) = area_oi((j-1)*dy_c+tan(sub_alpha(j))*...
                (dx*(N_x_i-i)),(j-1)*dy_c+tan(sub_alpha(j))*...
                (dx*(N_x_i+1-i)),dx/cos(sub_alpha(j)));
        end
    end
end

%West areas of the elements
A_w_i = zeros(N_x_i,N_r);
for j = 1:N_r
    for i = 1:N_x_i
         A_w_i(i,j) = area_oi(j*dy_c+tan(sub_alpha(j+1))*(dx*(N_x_i-i)),...
                     j*dy_c+tan(sub_alpha(j+1))*(dx*(N_x_i+1-i)),...
                     dx/cos(sub_alpha(j+1)));
    end
end

%Volume of the elements in the inlet
V_i = zeros(N_x_i,N_r);

for j = 1:N_r
    for i = 1:N_x_i
        if j == 1
           V_i(i,j) = V_i_element(dx,...
                        j*dy_c+tan(sub_alpha(j+1))*(dx*(N_x_i-i)),...
                        j*dy_c+tan(sub_alpha(j+1))*(dx*(N_x_i+1-i)));
        else
    V_i(i,j) = V_i_element(dx,...
                j*dy_c+tan(sub_alpha(j+1))*(dx*(N_x_i-i)),...
                j*dy_c+tan(sub_alpha(j+1))*(dx*(N_x_i+1-i)))-V_i(i,(j-1));
        end
    end
end

%% Total grid definition
A_n = [A_n_i; A_n_c];
A_s = [A_s_i; A_s_c];
A_e = [A_e_i; A_e_c];
A_w = [A_w_i; A_w_c];

alphas = zeros(N_x,N_r);
for j = 1:N_x
    for i = 1:N_r
    if j <= N_x_i
    alphas(j,i) = sub_alpha(i+1);
    else
    alphas(j,i) = 0;
    end
```

```
    end
end
%% Visualization of grid
figure(1)
%subplot(2,2,4)
hold on
for j = 1:N_r
    x1 = -(N_x_i*dx);
    y1 = j*dy_c;
    x2 = -L;
    y2 = y1;

    plot([y1,y2],[x1,x2],'b');
    hold on
end

for i = 1:N_x_c+1
    x1 = -(N_x_i*dx)-(i-1)*dx;
    y1 = 0;
    x2 = x1;
    y2 = (N_r*dy_c);

    plot([y1,y2],[x1,x2],'b');
    hold on
end

for j = 1:N_r
    x1 = 0;
    y1 = j*dy_c+tan(sub_alpha((j+1)))*(N_x_i*dx);
    x2 = -N_x_i*dx;
    y2 = j*dy_c;

    plot([y1,y2],[x1,x2],'b');
    hold on
end

for i = 1:N_x_i+1
    x1 = -(i-1)*dx;
    y1 = 0;
    x2 = x1;
    y2 = (N_r*dy_c)+tan(alpha)*((N_x_i*dx)-((i-1)*dx));

    plot([y1,y2],[x1,x2],'b');
    hold on

end

x1 = 0;
```

```
x2 = x1;
y1 = L;
y2 = -L;
plot([x1,x2],[y1,y2],'k--','LineWidth',2);

title('N =2 M = 2')
xlabel('Radial Location [m]')
ylabel('Axial Location [m]')
xlim([-0.05*(r_p+tan(alpha)*C_a) (r_p+tan(alpha)*(N_x_i*dx))])
ylim([-(r_p+tan(alpha)*C_a) 0.05*(r_p+tan(alpha)*C_a)])
hold on
x1 = r_p+tan(alpha)*C_a;
x2 = r_p;
y1 = 0;
y2 = -C_a;
plot([x1,x2],[y1,y2],'k--','LineWidth',2);
hold on
x1 = r_p;
x2 = r_p;
y1 = -C_a;
y2 = -L;
plot([x1,x2],[y1,y2],'k--','LineWidth',2);

%% Element center location

sub_sub_alpha = zeros(1,N_r-1);
for j = 1:N_r
    sub_sub_alpha(j) = (sub_alpha(j)+sub_alpha(j+1))/2;
end

Pos_x = zeros(N_x,N_r);
Pos_y = zeros(N_x,N_r);
for i = 1:N_x

 for j = 1:N_r
     if i <= N_x_i
        Pos_x(i,j)= 0.5*dy_c+dy_c*(j-1) + tan(sub_sub_alpha(j))*...
            (C_a-0.5*dx-(i-1)*dx);
     else
        Pos_x(i,j)= 0.5*dy_c+dy_c*(j-1);
     end
        Pos_y(i,j)= -0.5*dx-(i-1)*dx;
 end
end
```

4.2.3 2D Model - Solve

```
m_dot = 0.000374; %Mass flow pr. pellet channel [kg/s]
mu = 0.4; % Friction coefficient [-]
G = 20.7; %Ratio between E_l and E_r
nu = 0.025; % Poissons ratio

F_S = zeros(N_x,N_r,2);    %Force acting on the south face of the elements
F_N = zeros(N_x,N_r,2);    %Force acting on the north face of the elements

 P_out = 1; % Outlet pressure condition [Pa]
for j = 1:N_r
     F_S(end,j,1) = 0; %x-komponent of out-force
     F_S(end,j,2) = -(A_s(end,j)*P_out); %y-komponent of out-force
end


%% Force Balance Solve
for t = 1:N_x;
for n = 1:N_r;
 j=N_r+1-n;
 i=N_x+1-t;
syms F_N_x F_N_y

F_res = [F_S(i,j,1); F_S(i,j,2)];

F_in = [F_N_x; F_N_y];

if j == N_r; % Elements located next to the die wall (m=M)

F_wall = -(F_in(1)*cos(alphas(i,end))+F_in(2)*sin(alphas(i,end)))*...
            [cos(alphas(i,end)); sin(alphas(i,end))];

F_mu_wall = (mu*[-F_wall(2); F_wall(1)]);
tau_wall = norm(F_mu_wall)/A_w(i,end);

tau_center = (tau_wall/Pos_x(i,end))*Pos_x(i,end-1);
F_mu_center = tau_center*A_e(i,end)*...
                [-sin(alphas(i,end-1)); cos(alphas(i,end-1))];

[F_inx, F_iny] = solve(F_res+F_mu_center+F_mu_wall+F_in==0,[F_N_x F_N_y]);

elseif j==1;  % Elements located next to the symmetrical axis (m=1)

F_wall = (F_N(i,end,1)*cos(alphas(i,j))+F_N(i,end,2)*sin(alphas(i,j)))*...
            [cos(alphas(i,j)); sin(alphas(i,j))];
```

```
F_mu_wall =  (mu*[-F_wall(2); F_wall(1)]);
tau_wall = norm(F_mu_wall)/A_w(i,end);


tau_center2 = (tau_wall/Pos_x(i,end))*Pos_x(i,j);
F_mu_center2 = tau_center2*A_w(i,j)*[sin(alphas(i,j)); -cos(alphas(i,j))];


[F_inx, F_iny] = solve(F_res+F_mu_center2+F_in==0,[F_N_x F_N_y]);



else % Interior elements (1 < m < M)
F_wall = -(F_N(i,end,1)*cos(alphas(i,j))+F_N(i,end,2)*sin(alphas(i,j)))*...
            [cos(alphas(i,j)); sin(alphas(i,j))];

F_mu_wall =  (mu*[-F_wall(2); F_wall(1)]);
tau_wall = norm(F_mu_wall)/A_w(i,end);

tau_center2 = (tau_wall/Pos_x(i,end))*Pos_x(i,j);
F_mu_center2 = tau_center2*A_w(i,j)*[sin(alphas(i,j)); -cos(alphas(i,j))];


tau_center1 = (tau_wall/Pos_x(i,end))*Pos_x(i,j-1);
F_mu_center1 = tau_center1*A_e(i,j)*...
            [-sin(alphas(i,j-1)); cos(alphas(i,j-1))];

[F_inx, F_iny] = solve(F_res+F_mu_center1+F_mu_center2+F_in==0,...
                                                         [F_N_x F_N_y]);
end

F_N(i,j,1) = F_inx;
F_N(i,j,2) = F_iny;
if i > 1
F_S(i-1,j,1) = -F_inx;
F_S(i-1,j,2) = -F_iny;
else
    ;
end
end
end

%% Stresses
 for i = 1:N_x
     for j = 1:N_r
sigma_N(i,j) = (F_N(i,j,2)/A_n(i,j)); %Normal stress applied on the north
sigma_S(i,j) = (-F_S(i,j,2))/A_s(i,j);%Normal stress applied on the south
```

```
F_top(i,j) = (sqrt(F_N(i,j,2)^2+F_N(i,j,1)^2)); %Magnitude of F_N
    end
 end
```

4.2.4 2D Model - Contour plot

```
%% Contour plot for the 2D model

N_rad = zeros(N_x,1);
for i = 1:N_x
    if i <= N_x_i
    N_rad(i) = round(10^4*(N_r*dy_c+((N_x_i+1-i)*dx)*tan(alphas(i,end))));
    else
    N_rad(i) = round(10^4*(N_r*dy_c));
    end
end
%value = F_top;
value = P_N;
spaceing = round(N_rad./N_r);
Pos_x_grid = zeros(N_x,N_rad(1));
for i = 1:N_x
    for j = 1:N_rad(i)
Pos_x_grid(i,j) = (j)*Pos_x(i,end)/N_rad(i);
% if Pos_x_grid(i,j) == 0
%     Pos_x_grid(i,j) = NaN;
% end
    end
end

data = zeros(N_x,N_rad(1));
for i = 1:N_x
for j = 1:N_rad(i)
    Value_x_grid = interp1(Pos_x(i,:),value(i,:),Pos_x_grid(i,:));
    data(i,j) = Value_x_grid(j);
end
end

data(data == 0) = NaN;

invdata = zeros(N_x,N_rad(1));
for i = 1:N_x;
    for j = 1:N_rad(1);
        invdata(i,j) = data(i,end+1-j);
    end
end
invPos_x_grid = -1*fliplr(Pos_x_grid(1,:));
Pos_x_grid = [invPos_x_grid Pos_x_grid(1,:)];
```

```
%% plot
data = [invdata data]./10^6;
figure(1)
hold on
surf(Pos_x_grid,Pos_y(:,1)+dx/2,data)
view(0,90)
grid off
xlim([-0.005 0])
ylim([-0.008 0.0003])
shading interp;
lighting gouraud
colormap(jet)
colorbar

xlabel('Radial position [mm]')
ylabel('Axial position [mm]')
c=colorbar
caxis([100 350])
ylabel(c,'Axial Stress [MPa]','FontSize',12)
```